INVESTIGATION OF TRACTION MOTOR CONTROL SYSTEMS FOR ELECTRIC VEHICLE APPLICATIONS

By

Matthew Liam De Klerk

217002170

Submitted in fulfilment of the academic requirements for the degree of Master of Science in Electrical Engineering

College of Agriculture, Engineering and Science, University of KwaZulu-Natal

July 2022

Academic Supervisor: Prof. A.K. Saha

As the candidate’s Supervisor I ✓agree/do not agree to the submission of this thesis.

15 July 2022

…… ……

Supervisor: Prof. AK Saha Date

DECLARATION 1 - PLAGIARISM

I, Matthew Liam De Klerk, declare that:

1. The research reported in this thesis, except where otherwise indicated, is my original research.

2. This thesis has not been submitted for any degree or examination at any other university.

3. This thesis does not contain other persons' data, pictures, graphs or other information, unless specifically acknowledged as being sourced from other persons.

4. This thesis does not contain other persons' writing, unless specifically acknowledged as being sourced from other researchers. Where other written sources have been quoted, then:
    a. Their words have been re-written but the general information attributed to them has been referenced
    b. Where their exact words have been used, then their writing has been placed in italics and inside quotation marks, and referenced.

5. This thesis does not contain text, graphics or tables copied and pasted from the Internet, unless specifically acknowledged, and the source being detailed in the thesis and in the References sections.

Signed:

Matthew Liam De Klerk

DECLARATION 2 - PUBLICATIONS

DETAILS OF CONTRIBUTION TO PUBLICATIONS that form part and/or include research presented in this thesis (include publications in preparation, submitted, *in press* and published and give details of the contributions of each author to the experimental work and writing of each publication)

a) List of published journal articles:

Publication 1:

M. L. De Klerk and A. K. Saha, "A Comprehensive Review of Advanced Traction Motor Control Techniques Suitable for Electric Vehicle Applications," IEEE Access, vol. 9, no. 1, pp. 125080-125108, Sep. 2021.

Publication 2:

M. L. De Klerk and A. K. Saha, "Performance analysis of DTC-SVM in a complete traction motor control mechanism for a battery electric vehicle," Heliyon, vol. 8, no. 4, pp. 1-16, Apr. 2022.

b) Research presentations

M.L. De Klerk and A.K. Saha, "Investigation of Traction Motor Control Systems For Electric Vehicle Applications", Postgraduate Research and Innovation Symposium (PRIS), Durban, South Africa, December 2021 (online).

Signed:

Matthew Liam De Klerk

Acknowledgements

All glory to God, as everything I have and am able to do comes from Him!

I would like to thank my supervisor, Prof. Akshay Kumar Saha, whose continuous support, encouragement, and academic guidance were invaluable in the preparation of this dissertation. I am extremely grateful for everything I have learnt from your extensive knowledge and dedication.

To my parents, Evelyn and Grant De Klerk, thank you for all of the love, support and guidance that you have given me over the course of my studies and long before my studies even began. Words cannot express how grateful I am for all that you have done for me.

To my sister, Jenna De Klerk, thank you for all of the love and support that you have shown me. All the best for your university studies which are approaching in the near future!

To my grandparents and other close family, I really appreciate all of your love and support; thank you.

Thank you to my close friends, who took an interest in my studies and were always willing to give advice and suggestions.

Finally, I would like to thank the University of KwaZulu-Natal, whose academic and financial support has been a significant help in the completion of my studies.

Abstract

Electric vehicles are a promising solution to the current pollution and greenhouse gas issues faced by the transport sector. As such, the traction motor control system of an electric vehicle is worthy of investigation. Direct torque and indirect field-oriented control are commonly applied control techniques, enabling advanced control of the induction and permanent magnet synchronous motors currently used in most electric vehicles being produced. Various improvements have been made to current traction motor control schemes to reduce ripple, improve parameter insensitivity, and increase powertrain efficiency. Consequently, the objective of the research conducted is to contribute to the field of electric vehicle powertrains through comprehensive investigations into the suitability and performance of direct torque and indirect field-oriented control in the traction motor control system of an electric vehicle. A four-stage simulation-based investigation was undertaken, with five motor control techniques initially assessed, which were conventional direct torque and field-oriented control, two space vector modulation-based direct torque control systems and fuzzy logic-based direct torque control. Results from the first stage of the simulation-based study highlighted expected issues with conventional direct torque control and showed that fuzzy logic-based direct torque control and space vector modulational-based direct torque control with closed-loop torque and flux control present promising solutions for use in the traction motor control system of an electric vehicle. Extensions of the simulation-based investigation in stages two and three included the integration and assessment of field-weakening control and sensorless speed estimation. Furthermore, stage four concluded the investigation with an essential analysis of a complete control mechanism in realistic urban and highway driving conditions. The fourth stage utilised sections of the New York City Cycle and Highway Fuel Economy Test cycle, with a simulated vehicle load. The complete study indicated that space vector modulation-based direct torque control with closed-loop torque and flux control performs suitably for electric vehicle applications, providing favourable speed, torque, current and stator flux results with a faster computation time than some comparable control options. The comprehensive investigation extends current literature and forms a basis for further investigation in the field of traction motor control systems for electric vehicle applications.

Contents

Table of Figures

List of Tables

List of Abbreviations

ANN	Artificial Neural Network
ANN-DTC	Artificial Neural Network-Based DTC
ASR	Acceleration Slip Regulation
BEV	Battery Electric Vehicle
CDTC	Conventional Direct Torque Control
CH_4	Methane
CO_2	Carbon Dioxide
DC	Direct Current
DDC	Delhi Driving Cycle
DFIM	Doubly Fed Induction Motor
DSP	Digital Signal Processor
DTC	Direct Torque Control
DTC-SVM	Space Vector Modulation-Based Direct Torque Control
DTC-SVM-FC	DTC-SVM with Closed-Loop Flux Control
DTC-SVM-FTC	DTC-SVM with Closed-Loop Torque and Flux Control
DTC-SVM-TC	DTC-SVM with Closed-Loop Torque Control
DTRFC	Direct Torque and Rotor Flux Control
EMF	Electromotive Force
EMI	Electromagnetic Interference
ESS	Error Status Selection
EV	Electric Vehicle
EVT	Electrical Variable Transmission
FCEV	Fuel Cell Electric Vehicle
FFT	Fast Fourier Transform
FLC	Fuzzy Logic Control
FOC	Field-Oriented Control
FPGA	Field Programmable Gate Array
Fuzzy DTC	Fuzzy Logic-Based DTC
FW	Field-Weakening
HEV	Hybrid Electric Vehicle
HOSMC	High Order Sliding-Mode Control
HWFET	Highway Fuel Economy Test
ICEV	Internal Combustion Engine Vehicle
IFOC	Indirect Field-Oriented Control
IM	Induction Motor

ITAE	Integral Time-Weighted Absolute Error
LPV	Linear Parameter Varying
MF	Membership Function
MPC-DTC	Model Predictive-Based DTC
MRAS	Model Reference Adaptive System
N_2O	Nitrous Oxide
NEDC	New Europe Drive Cycle
Ni-Cd	Nickel-Cadmium
NiMH	Nickel-Metal Hydride
Ni-Zn	Nickel-Zinc
NYCC	New York City Cycle
OL	Open-Loop
PI	Proportional Integral
PM	Permanent Magnet
PMSM	Permanent Magnet Synchronous Motor
RIOL	Robust Input-Output Feedback Linearization
RMSE	Root Mean Square Error
SM	Sliding-Mode
SMC-DTC	Sliding Mode Control-Based DTC
SOC	State of Charge
SOM	Smallest of Maximum
SVPWM	Space Vector Pulse Width Modulation
THD	Total Harmonic Distortion
TTW	Tank to Wheel
VVVF	Variable-Voltage Variable-Frequency
WTW	Well to Wheel
XSG	Xilinx System Generator

List of Symbols

T_{e_N}	Nominal torque
$\vec{V_s}$	Stator voltage vector
$\overrightarrow{V_s^*}$	Reference stator voltage vector
$\lvert\psi_r\rvert$	Rotor flux magnitude
ψ_{s_N}	Nominal stator flux
$\overrightarrow{\psi_s^*}$	Reference stator flux
h_{T_e}	Torque hysteresis controller band width
h_ψ	Stator flux hysteresis controller band width
C_D	Aerodynamic drag coefficient
I_s	Stator current
$K_{p\psi}$	Proportional gain of flux PI controller
L_m	Per-phase mutual inductance
L_r	Per-phase rotor inductance
L_s	Per-phase stator inductance
L_s'	Stator transient inductance
P_{max}	Maximum power of motor
R_r	Per-phase referred rotor resistance
R_s	Stator resistance
$T_{e,sat}$	Torque saturation limit
T_e	Electromagnetic torque
$T_{i\psi}$	Integral time constant of flux PI controller
T_{max}	Maximum torque
T_s	Switching period
V_{dc}	DC inverter supply voltage
V_{fund}	Fundamental phase amplitude
$V_{s,max}$	Maximum phase voltage
i_0	Gear ratio
i_{dr}	d Component of the rotor current (d-q reference frame)
i_{ds}	d Component of the stator current (d-q reference frame)
i_{qr}	q Component of the rotor current (d-q reference frame)
i_{qs}	q Component of the stator current (d-q reference frame)
$i_{\alpha r}$	α Component of the rotor current (α-β reference frame)
$i_{\alpha s}$	α Component of the stator current (α-β reference frame)

$i_{\beta r}$	β Component of the rotor current (α-β reference frame)
$i_{\beta s}$	β Component of the stator current (α-β reference frame)
m_i	Modulation index
t_m	0-100 km/h acceleration time
v_{as}	Phase A stator voltage
v_{bs}	Phase B stator voltage
v_c	Climbing/grading velocity
v_{cs}	Phase C stator voltage
v_{ds}	d Component of the stator voltage (d-q reference frame)
v_m	Final acceleration speed
v_{max}	Maximum velocity
v_{qs}	q Component of the stator voltage (d-q reference frame)
$v_{\alpha s}$	α Component of the stator voltage (α-β reference frame)
$v_{\beta s}$	β Component of the stator voltage (α-β reference frame)
α_{max}	Maximum grading angle
η_t	Driveline efficiency
θ_e	Stator flux position (α-β reference frame)
ρ_a	Air density
τ_r	Rotor time constant
ψ_{dr}	d Component of the rotor flux (d-q reference frame)
ψ_{ds}	d Component of the stator flux (d-q reference frame)
ψ_{qr}	q Component of the rotor flux (d-q reference frame)
ψ_{qs}	q Component of the stator flux (d-q reference frame)
$\psi_{s,rated}$	Rated stator flux
$\psi_{\alpha r}$	α Component of the rotor flux (α-β reference frame)
$\psi_{\alpha s}$	α Component of the stator flux (α-β reference frame)
$\psi_{\beta r}$	β Component of the rotor flux (α-β reference frame)
$\psi_{\beta s}$	β Component of the stator flux (α-β reference frame)
ω_{base}	Base speed
ω_e	Synchronous speed
ω_{mr}	Speed of the rotor flux relative to the stator (induction motor)
ω_r	Rotor speed
ω_{sl}	Slip speed
$\lvert\psi_s\rvert$	Estimated stator flux magnitude
$\lvert\psi_s^*\rvert$	Reference stator flux magnitude

$\Delta\vec{\psi}_s$	Stator flux change
ΔT_e	Electromagnetic torque error
$\Delta\psi_s$	Stator flux error
A	Front area of vehicle
HB_{Te}	Torque hysteresis band limit
HB_{ψ}	Stator flux hysteresis band limit
P	Number of motor poles
f	Tyre rolling resistance coefficient
g	Gravitational acceleration
k	Motor overload factor
m	Vehicle mass
n	Rated speed
p	Differential operator
δ	Rotational inertial factor
σ	Total leakage factor

1. Chapter 1 – Introduction

1.1. Introduction to the Research Work

Electric vehicles (EVs) are becoming increasingly important, as they provide a solution to many issues that are currently faced by the transport sector [1], [2], [3]. Transport and vehicular travel are essential for socio-economic growth, forming a major part of the operation of cities and businesses around the world. In its current state, the transport sector relies largely on internal combustion engine vehicles (ICEVs); however, this reliance is proving to be problematic as ICEVs contribute to greenhouse gases and urban air pollution as a result of tailpipe emissions [4], [5]. The environmental risk posed by the transport industry has been a topic of discussion for a number of years. Consequently, EVs are currently a major consideration and can aid in the reduction of greenhouse gas emissions and the preservation of non-renewable resources [2], [6], [7], [8]. Such increasing attention and consideration have resulted in significant increases in the sale of battery electric vehicles (BEVs), with increased annual growth rates as high as 54-87% during 2012-2014 [9].

Due to their importance, continual development of EVs is essential, and various mechanical design concepts can be employed in order to improve the performance of electric vehicles. However, optimisation of the electrification of the EV powertrain is also an essential aspect enabling further efficiency and range improvements. Motor drive technology forms a core part of the systems that are utilised in an electric vehicle powertrain, and as a result, such technology demands attention and continuous advancement. Electric vehicles have intensive performance requirements, demanding more from the electric machines (motors) utilised than common industrial applications [10]. Electric motor performance requirements for EV applications include high torque and power density, wide speed range, high efficiency and high torque capability [10], [11], [12]. As a result, highly efficient electric motors can be used in order to enhance driving range, with the use of correctly selected electrical propulsion allowing for instant and high torques, at low-speed operation, making EV technology suitable for urban driving [13], [14].

Through the development of electric vehicle technology, various electric machines have been investigated for use in electrified automotive propulsion [5], [11], [15]. Direct Current (DC) motors were initially utilised in most electric vehicle systems, providing ease of integration and control. However, DC machines are not the best suited to meet the high-performance requirements of EV systems [10], [16]. The development of power electronics has resulted in three-phase induction and permanent magnet (PM) machines being the most commonly used in electric and hybrid electric vehicles which are currently commercially available [3], [11], [12]. The traction

motor control mechanism is an essential subsystem in the EV powertrain, with control techniques dependent on the motor utilised. Frequent use of three-phase induction and permanent magnet synchronous motors (PMSMs) require complex vector and direct torque control techniques in order to meet the speed and torque requirements of automotive applications.

1.2. Motivation

The operation of many cities and business sectors around the world is largely dependent on transport and vehicular travel. Internal combustion engine vehicles, which currently form the largest portion of the vehicles on the road, cause tailpipe emissions, generating urban air pollution and greenhouse gases. Due to an increasing population size, urbanization, and socio-economic development, an increase in vehicle usage and the resulting emissions have been observed [17], [18]. In 2004 and 2007, the transport sector was responsible for 23-26% of the global carbon dioxide (CO_2) emissions and 74% of the on-road CO_2 emissions, respectively [17], [18]. In addition to CO_2, ICEVs emit various other pollutants, which include nitrous oxide (N_2O) and methane (CH_4) [17], [18]. Furthermore, the use of fossil fuels associated with ICEVs could see the depletion of non-renewable resources in the future [18], [19]. In an effort to prevent such long-term damage, the United Nations have provided objectives and deadlines to all countries concerning the reduction of carbon emissions [5], [6]. Measures must be taken in order to reduce the environmental effects of the transport industry on both the environment and the depletion of global natural resources [18]. One of the major solutions to the current environmental issues faced is the consideration and development of battery, or pure electric vehicles (BEVs) [6], [7], [8].

In addition to mitigating the emission of greenhouse gases and urban air pollution, efficiency analysis provides further motivation for investigation into the use of electric vehicles. The Tank to Wheel efficiency (which assesses the efficiency of the vehicle between the energy content in the fuel tank/battery system and the energy output from the wheels) of a BEV ranges between 50 – 80%, which is significantly higher than the Tank to Wheel efficiencies obtained from gasoline and diesel ICEVs, typically in the ranges of 14 – 33% and 28 – 42%, respectively [20], [21], [22], [23], [24]. Additionally, significant benefits are also obtained from EVs which are charged using solar or wind farm systems [20].

In light of the urgent and growing need for a solution to the issues associated with ICEVs, the mitigation of tailpipe emissions and highly efficient powertrain structure means that electric vehicles are a solution that cannot be overlooked. The traction motor control mechanism is essential to the performance of EV systems and must be correctly designed to ensure improved vehicle rideability and efficiency. As a result, control techniques which are applicable for use in the traction motor control system of an EV are worthy of attention and investigation.

1.3. Research Questions

The chapters that follow aim to answer the following research questions, which surround the control of the traction motor in battery electric vehicles.

- What techniques have been employed in traction motor control systems investigated in literature, and what are the most effective improvements made?
- How suitable are conventional vector and direct torque-based controllers for use in battery electric vehicle systems?
- What improvements can be made to effectively reduce ripples (current, torque and flux), maintain a constant switching frequency, and improve vehicle rideability? Furthermore, which improvements are the most suitable when compared and consequently, are worthy of further investigation with the integration of additional control aspects (field-weakening control and sensorless speed control)?
- How do field-weakening and sensorless speed control algorithms perform in EV traction motor control systems? Which control algorithms are most effective, and which are most suitable for implementation?
- How does the complete traction motor control model (which contains both field-weakening and sensorless speed control), assessed under realistic vehicle loading, perform in urban and highway driving conditions?

1.4. Aims and Objectives

The research carried out in this dissertation aims to provide a thorough investigation of traction motor control mechanisms which are suitable for application in BEV systems. The aims and objectives of the proposed research are as follows:

- Conventional control structures used in the traction motor control mechanism of an EV and current state-of-the-art improvements that have been made should be identified from a theoretical perspective through a comprehensive literature review.
- Provide a theoretical and simulation-based analysis and comparison of vector (field-oriented) control and direct torque control for use in EV applications, determining the suitability of the control methods.
- Incorporate basic (space vector modulation-based techniques) and more complex (artificial intelligence-based techniques) improvements into the conventional direct torque-based control strategies. The strategies are to be compared in order to determine which improvements are the most suitable, based on algorithm complexity, computation time (directly related to hardware requirements), speed and torque response, and ripple reduction (torque, current and flux).

- Implement field-weakening control to allow for operation of the traction motor above the rated speed specification. Stable motor operation, with necessary torque or current limiting, is to be ensured in the field-weakening region.
- Implementation of sensorless speed control as it presents numerous advantages in EV systems. Both open-loop and closed-loop machine model-based estimation techniques are to be investigated.
- All control mechanisms investigated are to be evaluated based on the speed and torque responses, as well as the torque, current and flux ripples. More specialised and involved systems are also to be evaluated based on any specific requirements of the system. In addition, the control methods should be tested for suitability in standard urban and highway driving conditions.

1.5. Significance and Contribution of the Research

The significant and increasing need for a solution to the tailpipe emissions generated from ICEVs means that the traction motor control system of battery electric vehicles warrants in-depth investigation. Various research works have carried out reviews of advanced motor control techniques for both general and EV applications. However, despite the extensive research conducted in the field of EVs, a review had not been presented that comprehensively discusses the novel traction motor control techniques that are applied to EV applications. Such a review, which extensively discusses both conventional and state-of-the-art control techniques, is provided in chapter 2 of this dissertation, with the findings published in a review journal article [25]. The main contributions of which are as follows:

1. An overview of important information on current EV systems, with focus on the EV powertrain and EV efficiency in comparison to ICEVs. A comprehensive overview of direct torque control (DTC) and field-oriented control (FOC) is also provided.
2. A review of DTC and FOC mechanisms which are applied to electric vehicle applications, with a discussion of novel improvements made to the mechanisms.
3. A summary of the scope of the research works reviewed, as well as a tabulated overview of the merits and demerits of each.

Both direct torque control and field-oriented control present promising results in various scenarios and studies in literature, which make both control structures worthy of attention and investigation. However, many of the already presented studies consider small-scale models, in which experimental testing forms the basis of the conclusions made. Even in cases in which simulation studies are presented, low power rating motors and systems are investigated. It is essential to understand the theoretical performance of control mechanisms in appropriately scaled systems. As a result, chapters 4, 5 and 6 of this dissertation contribute a study which investigates motor

sizing through parameter matching while also considering improvements and additions to the control mechanism, including ripple reduction, field-weakening control, and sensorless speed control. A small portion of the findings from chapters 4, 5 and 6 are published in a research journal article [26]. The main contributions of these chapters are as follows:

1. A comprehensive study and comparison of various traction motor control mechanisms using an appropriately sized traction motor drive system assessed at realistic torque loads. The control mechanisms assessed are conventional direct torque and field-oriented control, space vector modulation-based DTC using closed-loop torque control (DTC-SVM-TC), space vector modulation-based DTC using closed-loop torque and flux control (DTC-SVM-FTC), and fuzzy logic-based DTC.
2. A comparison of DTC-SVM-FTC and fuzzy logic-based DTC with the incorporation of field-weakening control, enabling the mechanisms to be assessed over the entire speed range required.
3. An investigation into the performance of DTC-SVM-FTC which contains both field-weakening control and sensorless speed estimation. A comparison of two sensorless speed estimation methods is made when integrated with the DTC-SVM-FTC mechanism. The sensorless speed estimation methods investigated are an open-loop rotor flux-based speed estimation method and a closed-loop rotor flux-based MRAS speed estimation method.

In addition to the investigation and simulation of traction motor control mechanisms with a suitably scaled traction motor drive system, it is also useful to assess the complete control system under realistic vehicle loading in both urban and highway driving conditions. This is the main contribution of chapter 7, which assesses the complete DTC-SVM-FTC mechanism with a simulated vehicle body (simulating realistic vehicle loading) in both urban and highway driving conditions. The urban driving performance of the system is assessed using sections of the New York City Cycle, whereas the highway driving performance is assessed using the Highway Fuel Economy Test cycle.

1.6. Limitations of the Research Work

The following limitations were noted when conducting the research described in this dissertation:

- Although the study carried out in this dissertation comprehensively investigates the traction motor control system of an electric vehicle, the performance of the traction motor control mechanism is not assessed in conjunction with a complete drivetrain system. While important portions of the drivetrain are included, the battery system and DC-DC bidirectional converter are omitted as they do not fall within the scope of the research

conducted. The work carried out in this dissertation can be utilised to enable further investigation in which the performance of a complete drivetrain is assessed.

- The research work carried out in this dissertation is simulation-based and has no practical or experimental aspect. While practical or experimental investigation of full-sized EV systems is a very difficult task, a smaller scale model could present useful insight in some areas of an extended study.

1.7. Structure of the Dissertation

The investigation of traction motor control mechanisms applicable to battery electric vehicle applications is essential, as the traction motor drive system is a key aspect in the performance of a BEV system. Prior to a simulation-based investigation of suitable control systems, it is essential to understand which control schemes are currently applied to EV systems and the development currently being carried out. As a result, chapter 2 provides a comprehensive review of literature surrounding traction motor control techniques suitable for EV applications. The review presents important information about EV drivetrains and EV efficiency, discusses conventional DTC and FOC schemes, and reviews current improvements made to DTC schemes. Furthermore, the chapter reviews current literature which investigates the application of DTC and FOC mechanisms to EV systems, with focus also given to the novel aspects of the schemes proposed. Notably, a tabulated summary of the scope of various research works and the merits and demerits of each is provided.

The methodology used for the research work undertaken is detailed in chapter 3, which includes detailed descriptions of the parameter matching process, and all aspects of the control systems employed. Following the methodology provided, chapter 4 provides an initial investigation and comparison of various traction motor control techniques to assess their suitability for use in EV systems. The control techniques are assessed using only a section of the speed range required as field-weakening control is not integrated into the mechanisms investigated in chapter 4. Conventional DTC and FOC, DTC-SVM-TC, DTC-SVM-FTC, and fuzzy logic-based DTC are investigated, with focus given to the speed, torque, current and stator flux results observed. However, the two control techniques which exhibit the best performance (DTC-SVM-FTC and fuzzy logic-based DTC) are extended in chapter 5, with the inclusion of field-weakening control. Consequently, chapter 5 is able to provide an assessment and comparison of both techniques across the entire speed range required, while the operation of the field-weakening control system is assessed based on stator flux variation and torque limiting. The DTC-SVM-FTC mechanism is further extended in chapter 6, with the inclusion of sensorless speed control. The performance of the DTC-SVM-FTC mechanism is assessed with the use of two different sensorless speed estimation techniques, namely an open-loop rotor flux-based estimation technique and a closed-

loop rotor flux-based MRAS estimation technique. The techniques are assessed based on their suitability for use in EV applications, with the steady-state speed error a notable metric in the comparison of the two systems. The simulation-based study carried out is concluded in chapter 7, which assesses the performance of the complete DTC-SVM-FTC mechanism (including field-weakening control and closed-loop rotor flux-based MRAS speed estimation) in both urban and highway driving conditions. Furthermore, the investigation carried out in chapter 7 makes use of a simulated vehicle body, providing realistic vehicle loads for the investigation. Finally, chapter 8 concludes the research work undertaken and provides suggestions for extension of the investigation.

2. Chapter 2 – Theoretical Background and Literature Review

2.1. Introduction

Valuable research into the traction motor control system of an electric vehicle requires an understanding of the current work that has been conducted in the field. As a result, this chapter aims to present a comprehensive review of both conventional and novel traction motor control techniques applicable to EV systems, which have been presented in literature. It is useful to note that various other reviews have also investigated advanced motor control techniques. However, a review had not been presented that comprehensively discusses the novel traction motor control techniques that are applied to EV applications.

The authors in [27] and [28] provide a review of direct torque-controlled induction motor drives. While the authors in [27] provide a comprehensive discussion surrounding the suitability of DTC in EV applications, the researchers in [28] discuss various applications of DTC. A further review of modern improvement techniques used in DTC schemes is provided in [29]; however, although various applications of DTC are mentioned, the focus is on the changes to the conventional DTC system. The authors in [12] review design approaches and control strategies that can be used for energy-efficient electric machines that are applicable in EV applications. As a result, the discussion around applicable control methods is focused on loss minimisation control. The power electronics and motor drive technology applicable to various types of EVs are reviewed in [1]; however, focus is not given to traction motor control methods. Furthermore, the researchers in [11] review the present status and future trends of propulsion technologies which are utilised in EV systems; however, as in [1], although the power electronics required for EV systems are discussed, focus is not given to the traction motor control mechanism. Lastly, the authors in [17] provide a comprehensive review of EV systems and also provide various other applicable information. While the authors discuss applicable traction motor control mechanisms, a very brief discussion is given, providing only a general overview.

Additionally, it is noted that there are also various other research areas which are being investigated in the field of both conventional vehicle and EV technology. The authors in [30] provide a review of chassis coordinated control for full X-by-wire vehicles. X-by-wire chassis vehicles are investigated as the system enables improved active safety through the enhancement of the kinematic characteristics of the human-vehicle closed-loop system. The authors split their review of chassis coordinated control methods into two sections based on subsystem involvement patterns. An acceleration slip regulation (ASR) method that is suitable for four-wheel-independently-actuated EVs is proposed by X. Ding *et al.* [31]. The proposed method uses a

hybrid control scheme, in which the advantages of slip-ratio-based and maximum-torque-based acceleration slip regulation methods are combined to allow for acceptable ASR over a wide speed range. Four-wheel drive vehicles are discussed in [32], with the authors investigating electronic stability control, which considers both motor driving and braking torque distribution. The focus of the method is for a four-in-wheel motor drive electric vehicle. The authors make use of hardware-in-loop testing in order to validate the proposed system. Research conducted in [33] provides a comparative study of methods which can be used to estimate the sideslip angle of ground vehicles. The authors make use of a hardware-in-loop system in order to provide a comparison between various estimators, which include kinematics-, dynamics-, and neural network-based estimators. An interesting review focused on information-aware connected and automated vehicles is carried out by the authors in [34]. Such vehicles have the potential to introduce improved operational efficiencies and roadway safety. The review focuses on three important and interrelated aspects of information-aware connected and automated vehicles, which are sensing and communication technologies, human factors, and information-aware controller design. The review comprehensively discusses each key aspect, under which various additional topics are included. S. De Pinto *et al.* [35] make a comparison of different traction controllers which can be utilised in EVs with on-board drivetrains. Some of the controllers include PID and H_∞ control structures, which are designed specifically for onboard electric drivetrains. The authors indicate that the best performance is obtained through the use of control systems which are designed with the consideration of actuation dynamics.

2.2. Electric Vehicle Powertrain

Figure 2-1 shows a block diagram of a standard electric vehicle system, illustrating the major components and interconnections between them. The various types of interconnections are illustrated by the key provided in the figure. The motor, vehicle controller, power electronic circuitry, power source and transmission are the fundamental components of the system [8], [17]. The driver provides input to the system through the accelerator or brake pedal of the vehicle. The pedal operation acts as the user input (Figure 2-1), from which an electronic controller is utilised to provide inputs to the vehicle controller. Examples of such inputs are acceleration, braking and vehicle speed signals [11]. The vehicle controller has digital/control signal connections with both the battery management system and power electronic circuitry. The power electronic circuitry contained in an electric vehicle generally consists of a bidirectional DC-DC converter and a three-phase inverter circuit. The bidirectional DC-DC converter receives switching signals from the vehicle controller in order to maintain the correct DC link voltage. Furthermore, the three-phase inverter also receives control signals for the inverter switching state, which are based on vector control, motor/inverter protection control and high voltage circuit management control [11]. In order to provide control signals for both the bidirectional DC-DC converter circuit, and the three-

phase inverter, the vehicle controller requires that the DC link voltage and the three-phase inverter output current are measured. As a result, the vehicle controller also receives feedback from the power electronic circuitry. Finally, the motor provides a mechanical/torque signal to the mechanical transmission, enabling the vehicle to be driven. In general, there are three subunits which make up a typical vehicle load, which are the propulsion motor, as well as stabilized and unstabilized payloads [19].

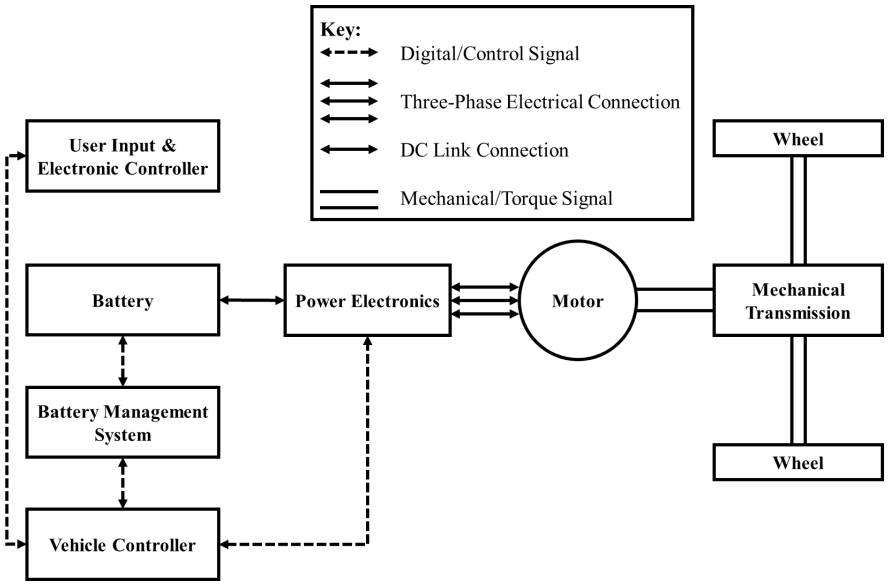

Figure 2-1: Generalised battery electric vehicle powertrain architecture [14], [17], [19], [36], [37]

A simplified BEV powertrain architecture is shown in Figure 2-2. The propulsion motor, which is often a PMSM or induction motor (IM), is the main vehicle load and is seen as a constant power load by the rest of the powertrain [19]. A controlled inverter (DC/AC converter) is utilised in order to connect the propulsion motor to the DC link [19], [9]. Stabilized payloads are not applicable to all general-purpose EV systems, with common examples of stabilized payloads being electronic weapons systems and surveillance cameras; however, vehicle lights are considered as unstabilized payloads and are essential to all electric vehicle systems [19].

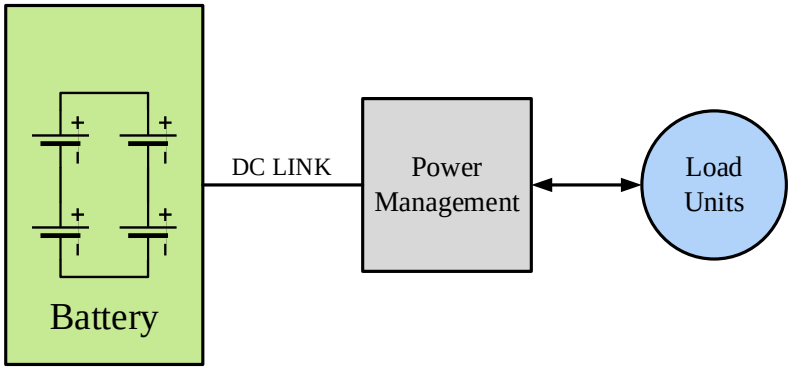

Figure 2-2: Simplified BEV powertrain architecture [19]

Table 2-1: Battery types – Advantages and disadvantages for use in EV applications [13], [14], [38]

Battery Type	Advantages	Disadvantages
Lead-Acid	Readily available in large production volumes. Lower in cost when compared to other battery types. Mature technology, has been widely used.	Low energy and power density. May require maintenance in certain applications. Has a limited life cycle when the batteries are utilised at a low state of charge.
NiMH (Nickel-Metal Hydride)	Double the energy density of lead-acid batteries. Recyclable and harmless to the environment. Safe operation at high voltages. Wide operating temperature range. Resistant to over-charging and over-discharging.	When discharged rapidly (high load currents), the lifetime is reduced to approximately 200-300 cycles. The batteries suffer from disadvantages relating to the memory effect, reducing usable power.
Lithium-Ion	Double the energy density when compared to (NiMH) batteries. High specific power and energy. Long battery life span, approximately 1000 cycles. Recyclable. Low memory effect. The batteries perform well at high temperatures.	High cost. Lengthy recharge time; however, still better than most other battery types.
Ni-Zn (Nickel-Zinc)	High power and energy density. Manufacturing utilises low-cost material. Wide operating temperature range. Capable of deep cycle operation. Environmentally friendly.	Not suitable for use in electric vehicles due to fast-growing dendrite.
Ni-Cd (Nickel-Cadmium)	Recyclable. Long lifespan. Can be discharged fully without causing damage to the battery.	Expensive for use in EVs. If Cadmium is not correctly disposed of, pollution can be caused.

In order to ensure the desired operation of an EV, the vehicle load requires that the voltage, power and energy can be instantaneously satisfied by the energy sources or storage units [19]. The battery system provides power to the EV drivetrain in a BEV and consists of multiple electrochemical cells that convert stored chemical energy into electrical energy [38]. The battery system capacity (Ah), energy (kWh), and usable state of charge (SOC) should all be considered in the design of an electric vehicle. The SOC measures the percentage of available capacity of the battery system in its current state [38]. As multiple electrochemical cells are required to form a complete battery system, there are various topologies in which the cells can be connected [39]. The topologies affect the energy, power, voltage range and maximum current of the system, and as a result, are essential in the BEV design [39]. The battery management system operates in communication with the battery system and vehicle controller, ensuring that the batteries are utilised only within the correct SOC range. This is essential, as continuous use of the batteries with a deep depth-of-discharge results in a reduced battery life cycle [38].

As the batteries are required to instantaneously satisfy the voltage, power and energy requirements for adequate operation of the EV, batteries are an integral part of the vehicle system. The authors in [13], [14], [38] consider the advantages and disadvantages of various types of batteries, which include lead-acid, lithium-ion, nickel-metal hydride, and nickel-zinc. The authors' findings are summarized in Table 2-1, showing a comparison of the advantages and disadvantages discussed. Due to the wide range of advantages that lithium-ion batteries offer, which include high energy density, good performance at high temperature, recyclability, low memory effect, high specific power, high specific energy, ability to utilize fast charging modes, and a long battery lifespan, they are the most commonly used in current EV powertrains [13], [14], [38].

Battery charging is a major challenge which EV technology faces, as charging duration and accessibility to public charging stations are issues which have not yet been completely resolved [38], [40]. Conductive charging is the conventional charging method for EV applications, and has two charging types, which are on-board and off-board charging. On-board charging is utilised for slower charging modes, and the EV has a built-in charger, allowing for this functionality [13], [38], [40]. The SAE and IEC define various charging levels for both AC and DC charging, which are summarized in Table 2-2.

There are various power electronic circuitries that are contained in an electric vehicle, which include DC/DC converters (utilised in battery charging and the DC/DC link between the battery system and motor control system), as well as the inverter circuitry in the motor control system [8], [17]. The power electronic circuitry should be designed to provide a fast and smooth response, controlled by both the driver control inputs and automatic tracking, which controls the recharging

and discharging of the batteries in the most efficient way [8]. Unidirectional or bidirectional DC/DC converters can be used in the battery charging system and the DC/DC link system between the batteries and the motor control system. However, the use of bidirectional converters allows for vehicle-to-grid power flow as well as regenerative braking in the vehicle. Regenerative braking allows the batteries to be charged during the operation of the vehicle, which takes place mainly during braking and downhill travel [8], [17].

Table 2-2: Charging power levels [13], [38], [40], [41]

Charging Level	**Charger Location**	**Typical Usage**	**Interface for Energy Supply**	**Power Level [kW] (Current [A])**
SAE Charging Standards				
Level 1 AC • **230 Vac (EU)** • **120 Vac (US)**	Single-Phase: On-board	Home/Office based charging	Any convenient outlet	• 1.9 (20) • 1.4 (12)
Level 2 AC • **400 Vac (EU)** • **240 Vac (US)**	Three-Phase/Single-Phase: On-board	Public/Private based charging	Electric vehicle supply equipment	• 19.2 (80) • 8 (32) • 4 (17)
Level 3 AC (Fast charging) • **208-600 Vac**	Three-Phase: Off-Board	Commercial charging points	Electric vehicle supply equipment	• 100 • 50
DC Power Level 1 • **200-450 Vdc**	Off-Board	Dedicated charging stations	Electric vehicle supply equipment	• 40 (80)
DC Power Level 1 • **200-450 Vdc**	Off-Board	Dedicated charging stations	Electric vehicle supply equipment	• 90 (200)
DC Power Level 1 • **200-600 Vdc**	Off-Board	Dedicated charging stations	Electric vehicle supply equipment	• 240 (400)
IEC Charging Standards				
AC Power Level 1	Single-Phase: On-board	Home/Office-based charging	Any convenient outlet	• 4-4.75 (16)
AC Power Level 2	Single-Phase/Three-Phase: On-board	Public/Private based charging	Electric vehicle supply equipment	• 8-15(32)
AC Power Level 3	Three-Phase: On-Board	Commercial charging points	Electric vehicle supply equipment	• 60-120 (250)
DC Rapid Charging	Off-Board	Dedicated charging stations	Electric vehicle supply equipment	• 1000-2000 (400)

The electric motor (driving the transmission mechanism and, subsequently, the vehicle) is driven by power electronic circuitry and various control mechanisms [17], [8]. Various motors can be utilised as the traction motor in an EV; however, three-phase induction and permanent magnet synchronous motors are the most commonly used [17]. In addition, various suitable drivetrain architectures can be implemented in BEVs. The implemented architecture affects the transmission system of the vehicle. The most commonly utilised transmission system is used in conjunction with a rear-wheel drive architecture, in which a fixed gearing system and differential are integrated into a single assembly. This transmission system configuration enables reduced transmission weight, as the gearing system and clutch have been omitted [17].

2.3. Electric Vehicle Efficiency

A complete analysis of efficiency, comparing internal combustion engine vehicles and EVs, is provided by the authors in [20]. An investigation of the vehicle Tank to Wheel (TTW) efficiency as well as the Well to Wheel (WTW) efficiency is carried out. The TTW efficiency provides an indication of the efficiency of the vehicle between the energy content in the battery system and the energy output from the wheels. The TTW efficiency is determined by the efficiency of the components in an EV system and can be estimated through literature [20]. With the consideration of various EV components, including the AC/DC converter (90-96% efficiency), the battery input (90-99% efficiency), the battery output (93-98% efficiency), the DC/AC converter (96-98% efficiency), the electric motor (81-95% efficiency), and the mechanical transmission (89-98% efficiency), it was determined that the TTW efficiency of an EV ranges between 50% and 80% [20], [21], [22], [23], [24]. This is in comparison to other types of vehicles which offer a much lower efficiency. Gasoline and diesel ICEVs exhibit a TTW efficiency in the range of 14-33% and 28-42%, respectively [20]. Therefore, it can be noted that EVs exhibit a much higher TTW efficiency than ICEVs; however, this is not necessarily the case when WTW efficiency is investigated. The WTW efficiency investigates the efficiency of all the processes necessary to power the vehicle and, as a result, is the efficiency from the extraction of natural resources for fuel to the final power output of the wheels of the vehicle [20]. The authors in [20] found that the WTW efficiency of an EV is dependent on the power generation source utilised for battery charging. EVs fed by natural gas power plants exhibit efficiencies in the range of 13-31%, whereas EVs fed from coal-fired or diesel power plants have WTW efficiencies in the range of 13-27% and 12-25%, respectively [20]. This is in comparison to gasoline or diesel ICEVs, which have WTW efficiencies in the range of 11-27% and 25-37%, respectively. This result suggests that the overall efficiency benefit obtained from EVs is not as significant. However, a notable finding is that EVs charged from solar or wind farm systems exhibit a WTW efficiency in the range of 39-67%. This is significantly higher than any other vehicle investigated and offers major efficiency benefits in complete vehicular systems [20].

The traction motor control circuit is essential to the successful operation of the vehicle, as the electric machine and drive system are core technologies in the electric vehicle powertrain system, ensuring the dynamic specifications of the vehicle can be met [17], [14]. As a result, the sections that follow in this review discuss the well-developed direct torque control and field-oriented control techniques, as well as novel implementations of these techniques in EV applications.

2.4. Direct Torque Control

2.4.1. Conventional Direct Torque Control

DTC offers comparable performance to FOC; however, intensive online coordinate transformations and calculations are not required [10], [27]. Additionally, the feedback current control performed in FOC is not required in DTC, and the motor torque is directly controlled, resulting in a fast torque response [10], [27]. As with FOC, DTC can be performed using sensorless speed control in advanced control models. DTC is applicable for high-speed operation and allows for frequent starting/stopping and acceleration [27]. DTC enables robust flux weakening control to be implemented and also enables dynamic operation of the motor [27]. However, DTC suffers from sluggish start-up response, with high current and toque ripple present in conventional direct torque control (CDTC) structures [10], [27], [42]. DTC also has a variable switching frequency, which is undesirable, and presents challenging control and high noise level at low speeds [27], [42].

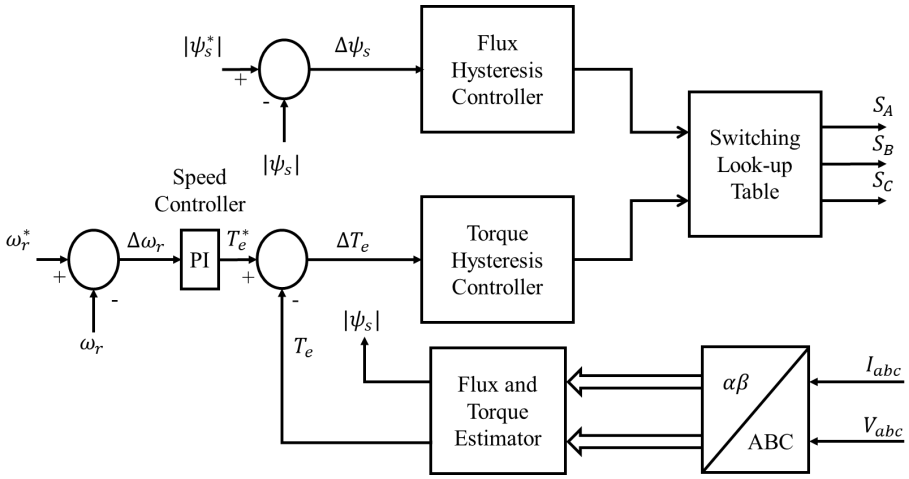

Figure 2-3: CDTC block diagram [10], [27], [42]

A block diagram depicting a conventional direct torque control system is shown in Figure 2-3, which utilises hysteresis control to control the motor torque and stator flux magnitude. CDTC consists of a largely online control method, in which the electromagnetic torque and stator flux of the motor are estimated using an estimator unit in the control model, as seen in Figure 2-3 [42]. In order for the necessary parameters to be estimated, the stator voltage and current must be measured and transformed to the stationary two-phase reference frame (α-β). Equation 2-1 shows

the equation for the transformation of the stator voltage into the stationary α-β reference frame [10], [27], [42], [43].

$$\begin{bmatrix} v_{\alpha s} \\ v_{\beta s} \end{bmatrix} = \frac{2}{3}\begin{bmatrix} 1 & -\frac{1}{2} & -\frac{1}{2} \\ 0 & \frac{\sqrt{3}}{2} & -\frac{\sqrt{3}}{2} \end{bmatrix}\begin{bmatrix} v_{as} \\ v_{bs} \\ v_{cs} \end{bmatrix} \tag{2-1}$$

Similarly, the stator current measured can also be transformed into the stationary α-β reference frame. Equations 2-2 – 2-5 show the equations utilised in the online estimation unit, allowing for the stator flux and electromagnetic torque to be estimated. Equations 2-2 and 2-3 allow for the stator flux in the α- and β- axis to be found, respectively [10], [27], [42].

$$\psi_{\alpha s} = \int (v_{\alpha s} - R_s i_{\alpha s}) dt \tag{2-2}$$

$$\psi_{\beta s} = \int (v_{\beta s} - R_s i_{\beta s}) dt \tag{2-3}$$

Equation 2-4 allows for the stator flux magnitude of the induction motor to be estimated [10], [27], [42].

$$|\psi_s| = \sqrt{\psi_{\alpha s}^2 + \psi_{\beta s}^2} \tag{2-4}$$

The electromagnetic torque developed by the induction motor can be estimated using Equation 2-5 [10], [27], [42].

$$T_e = \frac{3}{2}\frac{P}{2}(\psi_{\alpha s} i_{\beta s} - \psi_{\beta s} i_{\alpha s}) \tag{2-5}$$

Additionally, estimation of the position of the stator flux in the stationary reference frame is also required. The position is used to determine the instantaneous flux sector, which enables the inverter switching states to be correctly selected. The stator flux position in the stationary reference frame can be found using equation 2-6 [10], [27], [42].

$$\theta_e = tan^{-1}\left(\frac{\psi_{\beta s}}{\psi_{\alpha s}}\right) \tag{2-6}$$

Where in equations 2-1 – 2-6, v_{as}, v_{bs}, v_{cs} are the phase voltages applied to phase a, b and c of the stator, respectively, $v_{\alpha s}, v_{\beta s}$ are the stator voltages in the stationary α-β reference frame, $\psi_{\alpha s}$, $\psi_{\beta s}$ are the stator flux components in the stationary α-β reference frame, R_s is the stator resistance of the induction motor, $i_{\alpha s}, i_{\beta s}$ are the stator currents in the stationary α-β reference frame, $|\psi_s|$ is the estimated stator flux magnitude, T_e is the estimated electromagnetic torque developed by the induction motor, θ_e is the position of the stator flux in the stationary reference frame.

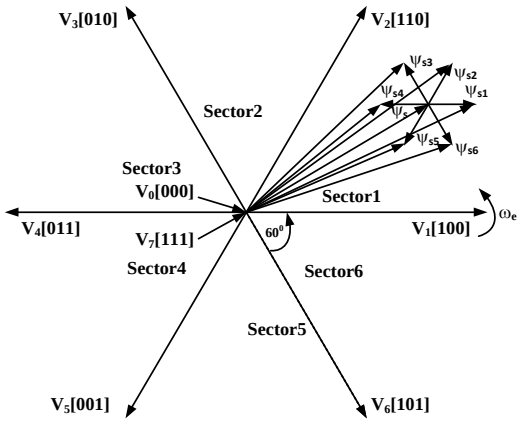

Figure 2-4: Voltage space vectors for inverter switching states and corresponding stator flux variations for Δt [10], [42]

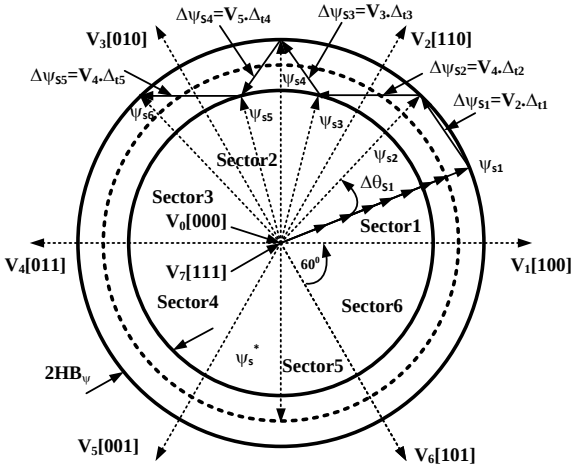

Figure 2-5: Trajectory of the Stator Flux Vector in CDTC [10], [42]

Equations 2-2 and 2-3 indicate that in order for the electromagnetic torque and stator flux to be estimated, the stator resistance (R_S) of the induction motor must be known. However, if the stator flux resistance is neglected for simplicity, equation 2-7 can be developed [10], [42].

$$\Delta\vec{\psi}_s = \vec{V}_s \Delta t \tag{2-7}$$

Equation 2-7 indicates that the stator flux of the induction motor can be changed through the application of a specific stator voltage ($\vec{V}_s$) for a period of time. Figure 2-4 shows the flux increments that correspond to each of the six space vector pulse width modulation (SVPWM) inverter vector voltages [10], [42].

In order to control the flux magnitude, hysteresis controllers are utilised. As a result, appropriate increments of the stator flux are chosen, ensuring that the flux remains within the specific hysteresis band. This is illustrated in Figure 2-5, which shows the trajectory of the stator flux within the hysteresis band [10], [42]. The stator flux and electromagnetic torque are controlled with the use of a two-level and a three-level hysteresis controller, respectively [10], [42]. The appropriate inverter switching states are determined with the use of the hysteresis controller

outputs, the stator flux position, and a look-up table. Table 2-3 shows the look-up table used in the CDTC model investigated in this review. The table corresponds to the theoretical switching table utilised in hysteresis-based DTC [10], [42].

Table 2-3: CDTC stator voltage vectors look-up table [10], [42]

HT_e	H_ψ	S1	S2	S3	S4	S5	S6
1	1	$\bar{V}_2$	$\bar{V}_3$	$\bar{V}_4$	$\bar{V}_5$	$\bar{V}_6$	$\bar{V}_1$
0	1	$\bar{V}_0$	$\bar{V}_7$	$\bar{V}_0$	$\bar{V}_7$	$\bar{V}_0$	$\bar{V}_7$
-1	1	$\bar{V}_6$	$\bar{V}_1$	$\bar{V}_2$	$\bar{V}_3$	$\bar{V}_4$	$\bar{V}_5$
1	-1	$\bar{V}_3$	$\bar{V}_4$	$\bar{V}_5$	$\bar{V}_6$	$\bar{V}_1$	$\bar{V}_2$
0	-1	$\bar{V}_7$	$\bar{V}_0$	$\bar{V}_7$	$\bar{V}_0$	$\bar{V}_7$	$\bar{V}_0$
-1	-1	$\bar{V}_5$	$\bar{V}_6$	$\bar{V}_1$	$\bar{V}_2$	$\bar{V}_3$	$\bar{V}_4$

Equations 2-8 and 2-9 show the outputs from the hysteresis controllers. The outputs are determined by the electromagnetic torque and stator flux error, represented as ΔT_e and $\Delta\psi_s$, respectively [10], [42]. The electromagnetic torque and stator flux hysteresis band limits are represented HB_{Te} and HB_ψ, respectively.

$$HT_e = \begin{cases} 1 & for\ \Delta T_e > HB_{Te} \\ 0 & for -HB_{Te} < \Delta T_e < HB_{Te} \\ -1 & for\ \Delta T_e < -HB_{Te} \end{cases} \tag{2-8}$$

$$H_\psi = \begin{cases} 1 & for\ \Delta\psi_s > HB_\psi \\ -1 & for\ \Delta\psi_s < -HB_\psi \end{cases} \tag{2-9}$$

As the torque is directly controlled in DTC, the desired speed can be achieved with the use of a proportional integral (PI) speed control loop. The PI controller in the speed control loop generates a torque reference that allows for the desired speed to be achieved. The hysteresis band limits are chosen to allow for control of the stator flux and electromagnetic torque values. The stator flux vector moves in a circular path created by the boundaries of the hysteresis band, as the maximum value of the stator flux is limited by the stator flux hysteresis controller [42]. The circular flux trajectory is depicted in Figure 2-5. The torque hysteresis band controls the torque ripple, with the torque ripple mostly independent of the stator flux hysteresis controller. Changes in the torque hysteresis band limits cause the torque ripple to respond proportionally. However, lower torque hysteresis band limits cause an increase in switching frequency and a proportional increase in inverter switching losses [42].

Lastly, the DC voltage required to supply the motor for adequate direct torque control must be calculated. The authors in [44] investigate the maximum modulation index of direct torque control while still allowing for a circular flux trajectory. However, reference [44] also provides an investigation into the modulation index of SVPWM. The DC link for an inverter with an SVPWM switching scheme can be found using equation 2-10 [44].

$$V_{dc} = \frac{V_{fund}}{m_i \times \frac{2}{\pi}} \tag{2-10}$$

Where; V_{dc} is the DC voltage required to supply the inverter, V_{fund} is the fundamental phase amplitude of the pulse-width-modulated switching sequence, and m_i is the modulation index of the inverter and switching scheme. It is possible to operate the inverter in the overmodulation range while still maintaining a circular flux trajectory in DTC.

There are certain disadvantages that are present when utilising the conventional direct torque control scheme. These disadvantages include high flux and electromagnetic torque ripples, current distortions and high current ripple. The disadvantages are well documented in literature, and are discussed by the authors in [10], [27], [45], [46], [47]. As a result, a large amount of research and investigation has gone into the improvement of CDTC.

In fact, the authors in [48] focus on optimisation of the torque tracking performance in DTC systems, utilising a proposed composite torque regulator. The authors aim to ensure that the system maintains the advantages present in conventional DTC while providing optimized torque tracking performance. The composite torque regulator proposed consists of a combination of two variable hysteresis bands, as well as two constant hysteresis bands. The constant hysteresis bands ensure that the fast dynamic response of CDTC is retained, whereas torque tracking precision under steady-state operating conditions is improved with the use of the variable hysteresis bands. A detailed discussion of the torque variation in CDTC is provided in order to indicate that the difference in increasing and decreasing rate of the torque significantly impacts the deviation of the average torque from the torque reference. Additionally, it is noted that deterioration of the torque tracking performance can occur as a result of the time delay of a sampling period. The authors indicate that such issues can be mitigated with the use of the proposed composite torque regulator. While the results obtained indicate that the torque tracking performance and torque ripple are improved through the use of the modified hysteresis controller, the modified hysteresis controller structure is significantly more complex. Additionally, there are various other control techniques in which the switching table and hysteresis controllers utilised in CDTC are replaced with other control mechanisms. However, none of these are compared with the proposed technique. As there are various other modifications that can be made to CDTC, section 2.4.2 of this chapter reviews various other improvements and novel techniques that have been proposed, which involve the replacement of the hysteresis controllers and switching table.

2.4.2. Improvements to Direct Torque Control

2.4.2.1. Integration of Space Vector Modulation into the CDTC System (DTC-SVM)

The DTC-SVM technique includes characteristics such as simple algorithm complexity and improved performance (reduced ripples, reduced current distortion, and constant switching frequency), with the main objective being mitigation of the issues observed in the conventional DTC system investigated. DTC-SVM systems consist of a similar hardware topology to that utilised in conventional DTC [28]. In general, DTC-SVM techniques involve the replacement of the hysteresis controllers and switching table present in conventional DTC structures. The switching table is replaced by a voltage modulator, utilised in order to calculate the correct switching states for the voltage source inverter [49]. The objective of the SVM technique is to enable optimal selection of the switching vectors, allowing for the reduction of torque/flux ripples and harmonic distortion in the current waveform by maintaining a constant switching frequency. As with CDTC, the DTC-SVM mechanism is dependent only on the stator parameters of the induction motor [49]. There are three DTC-SVM control structures that can be implemented, which are DTC-SVM with closed-loop flux control (DTC-SVM-FC), DTC-SVM with closed-loop torque control (DTC-SVM-TC), and DTC-SVM with closed-loop torque and flux control (DTC-SVM-FTC) [28], [50].

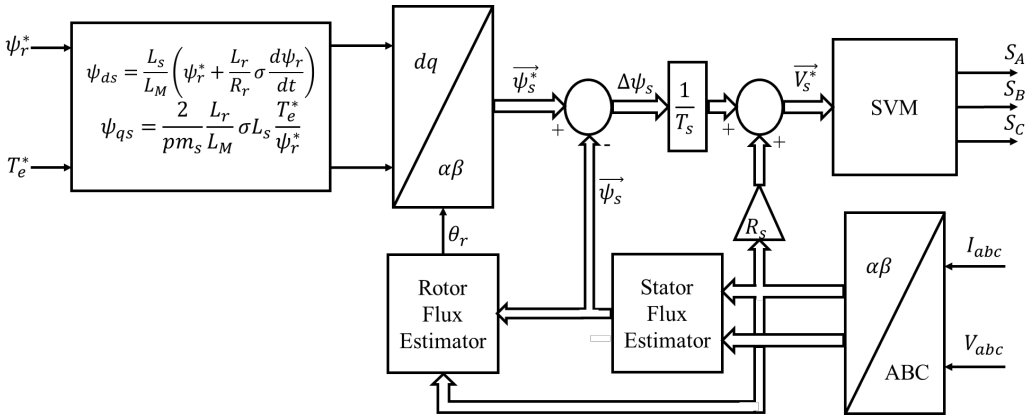

Figure 2-6: DTC-SVM with closed-loop flux control [28], [50], [46]

The authors in [28], [46], [50] present a review of DTC-SVM-FC. The structure of the control mechanism is shown in Figure 2-6, in which the rotor flux is assumed as a reference. With the electromagnetic torque reference and rotor flux reference known, the stator flux references in the rotating d-q reference frame can be found [28], [46], [50]. Ultimately, a comparison of the reference stator flux in the stationary α-β reference frame with the estimated stator flux values allows for the reference voltage vector to be determined utilising equation 2-11 [28], [46], [50].

$$\overrightarrow{V_s^*} = \frac{\Delta\psi_s}{T_s} + R_s I_s \tag{2-11}$$

The successful execution of DTC-SVM-FC requires various stator and rotor machine parameters and, as a result, is sensitive to parameter variation. However, despite this drawback, the control scheme enables increased torque overload capability [28], [46], [50].

Figure 2-7 shows the control structure of DTC-SVM-TC. Initially, DTC-SVM-TC was proposed for use in PMSM drives; however, the technique can also be easily applied to induction motor drives [50]. This variation of the DTC-SVM scheme allows for the improvement of the dynamic and steady-state performance of the torque response [46]. The torque error is utilised to determine torque angle increments ($\Delta\delta_\psi$) through PI controlled torque regulation. As a result, the torque can be controlled through changes in the angle between the stator and rotor fluxes [28], [46], [50]. The reference stator flux is found using equation 2-12, and the reference stator voltage vector is found using equation 2-11.

$$\overrightarrow{\psi_s^*} = |\psi_s^*| e^{j(\theta_e + \Delta\delta_\psi)} \tag{2-12}$$

The DTC-SVM structure with closed-loop torque control presents a useful strategy to improve the performance of the torque response obtained from the drive. In addition, only a single PI controller is required, ensuring a simple control loop design [50]. However, this also presents a disadvantage, as the flux is adjusted in an open-loop manner [50].

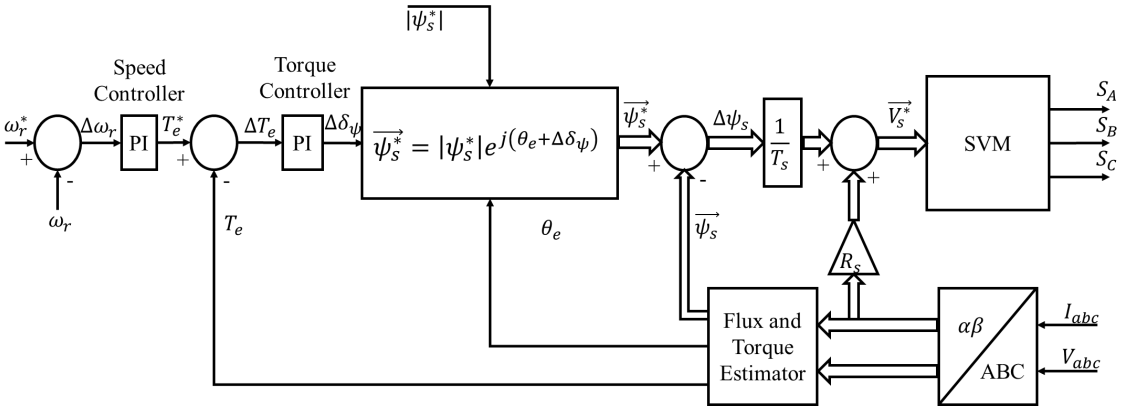

Figure 2-7: DTC-SVM with closed-loop torque control [28], [46], [50]

The authors in [49] present the use of DTC-SVM-TC, which also includes efficiency optimisation through a model-based loss minimisation strategy. Additionally, the authors attempt to provide robust speed regulation through the use of a second-order sliding-mode super twisting controller in the outer control loop. The loss minimisation model is based on optimal selection of the rotor and stator flux values; however, core losses are neglected for simplicity. The authors present DTC-SVM results with reduced torque and flux ripples and good current waveforms. Although this is expected of a DTC-SVM system, when compared to CDTC, the authors also show that the loss minimisation controller allows for significantly lower losses in no load or lightly loaded operating conditions. However, the authors do not present an explanation as to how the loss minimisation controller may be incorporated in cases when field-weakening (FW) control is required. Additionally, it would be interesting to observe the results obtained utilising the loss minimisation controller in a DTC-SVM system with closed-loop torque and flux control.

Furthermore, the authors in [51] present a study of DTC for induction motors which is based on minimum voltage vector error. The control mechanism proposed also utilises DTC-SVM-TC; however, the duty ratio of the fundamental voltage vector is optimized in order to minimise the error that occurs between the reference voltage vector and the voltage vector that is finally imposed. The duty ratio is optimized through an algebraic equation, making use of Pythagoras' Theorem, which allows for the improvement of the DTC system with a very simple optimisation technique. The proposed control mechanism with voltage vector duty ratio optimisation presents promising results and is compared to the work proposed by the authors in [52] and [53], as well as CDTC. The research scholars in [52] present a conventional DTC control mechanism which also includes optimisation of the voltage vectors through a torque minimisation strategy, while the authors in [53] present a discrete duty-cycle-control method for DTC, which incorporates a model predictive solution. While the work presented in [51] presents convincing results with a very simplified control technique, the authors do not provide a comparison between the proposed technique and DTC-SVM-TC that does not contain the optimisation strategy employed (such as making use of the symmetrical SVM technique). Such a comparison would be useful as it would allow the reader to gauge the improvement that fundamental voltage vector duty ratio optimisation provides to the system.

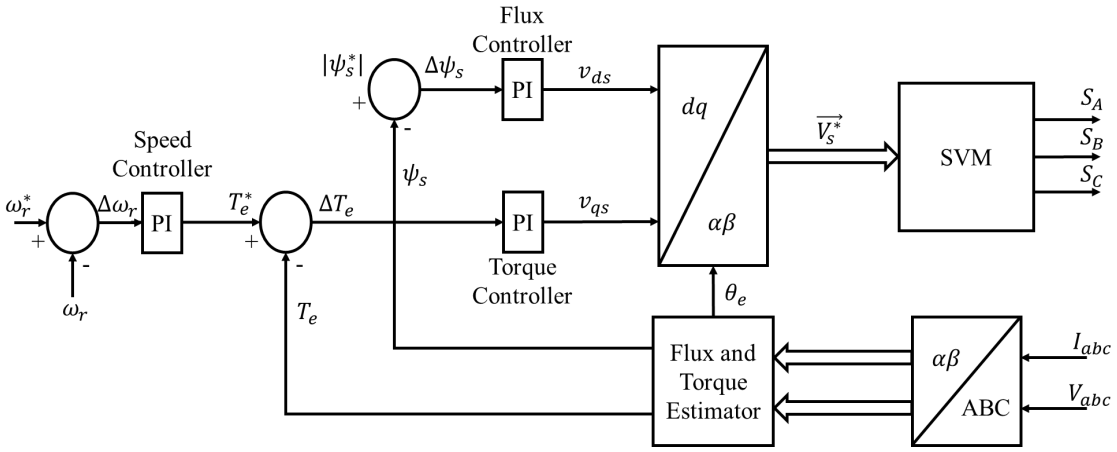

Figure 2-8: DTC-SVM with closed-loop torque and flux control in stator flux coordinates [28], [46], [50]

There are also other works that consider the use of DTC-SVM-TC. For instance, the authors in [54] ensure speed regulation with the use of a fuzzy logic controller in a system which utilises DTC-SVM-TC. The comparison provided between CDTC and DTC-SVM had already been well established in literature; however, the results obtained indicate that a more robust speed response is obtained when the fuzzy PI speed controller is implemented in comparison to a classical PI controller. Interestingly, the authors in [55] incorporate a new flux observer model into DTC-SVM-TC in order to control an electrically excited synchronous motor. A full-order, closed-loop stator flux observer is proposed by the authors, and the implemented system also uses a simplified

three-level SVPWM algorithm. The experimental setup used by the authors provides desirable results; however, a more extensive set of results may allow for further performance evaluation.

A DTC-SVM scheme which incorporates both closed-loop torque and flux control can be utilised in order to mitigate the issue present in DTC-SVM-TC which results from control of the flux in an open-loop manner. Figure 2-8 shows the structure of DTC-SVM-FTC in stator flux coordinates. The stator reference voltage components in the rotating d-q reference frame are generated from the flux and torque PI controllers. After which, the DC voltage commands are transformed into the stationary α-β reference frame. The reference values in the α-β reference frame can be used in order to control the SVM section of the mechanism [28], [46], [50].

DTC-SVM-FTC, which operates in polar coordinates, can also be utilised. However, the control scheme is more complex and relies on flux error values to generate the reference stator voltage vectors (equation 2-11), as was used in DTC-SVM-FC and DTC-SVM-TC [28], [46], [50]. Generating the reference stator voltage vectors in this manner presents a disadvantage in the related systems, as the differentiation algorithm utilised is sensitive to disturbances, with possible instability caused when errors occur in the feedback signal [50].

The research scholars in [56] propose the use of DTC-SVM-FTC in stator flux coordinates. The aim of the research presented by the authors is to enable a higher constant switching frequency without the need for a higher sampling frequency or deadbeat controller, while also significantly reducing the torque and speed ripple. The proposed aim of the research allowed for significant simplification of schemes that contain a deadbeat controller while minimizing the issues associated with conventional DTC. An increased switching frequency is achieved through the use of the symmetrical regular-sampled SVM technique, allowing for a constant switching frequency, which is equivalent to the sampling frequency. The results obtained show an increased switching frequency when compared with CDTC, with significantly reduced torque and flux ripples. The authors proposed a small change to the scheme, with significantly better results obtained. However, other improvements to CDTC, such as predictive control, artificial intelligence and multilevel inverters, are not compared.

There are also various other works surrounding DTC-SVM-FTC. The authors in [57] present two methods for PI controller design in DTC-SVM-FTC. The first method uses the symmetric optimum criterion and provides a simple method for the design of the controllers. However, controller design using the full induction motor model and the root locus method provides better results. While the paper presents useful methods for PI controller design, other types of controllers are not considered and compared. Furthermore, the authors in [58] provide a simulation-based

comparison of conventional DTC and DTC-SVM. The study shows that DTC-SVM provides improved electromagnetic torque and stator flux results due to a constant switching frequency; however, the speed response is not discussed, and as a result, the operating conditions under which the motor is operating are not fully defined. Finally, the authors in [59] and [60] also provide general research on DTC-SVM-FTC, with the authors in [59] investigating an FPGA implementation of the system.

2.4.2.2. Integration of Fuzzy Logic Control into the CDTC System (fuzzy DTC)

S. Gdaim *et al.* [61] investigate the design and experimental implementation of a fuzzy logic-based DTC mechanism for the control of an induction motor. Initially, the authors present a discussion of conventional direct torque control, citing the disadvantages associated with it. Such disadvantages are well documented in literature and form the basis for research into improvements of the conventional control methodology. Fuzzy logic control (FLC) was integrated with the conventional DTC mechanism, as it allows for control of the system without knowledge of the mathematical model of the plant while also aiding in the reduction of the torque and flux ripples observed in CDTC [61]. The proposed fuzzy logic controller replaces the torque and flux hysteresis controllers, as well as the switching look-up table that are present in the CDTC mechanism. However, the controller proposed receives the torque error, stator flux error and stator flux angle as inputs, with the necessary inverter switching state as an output.

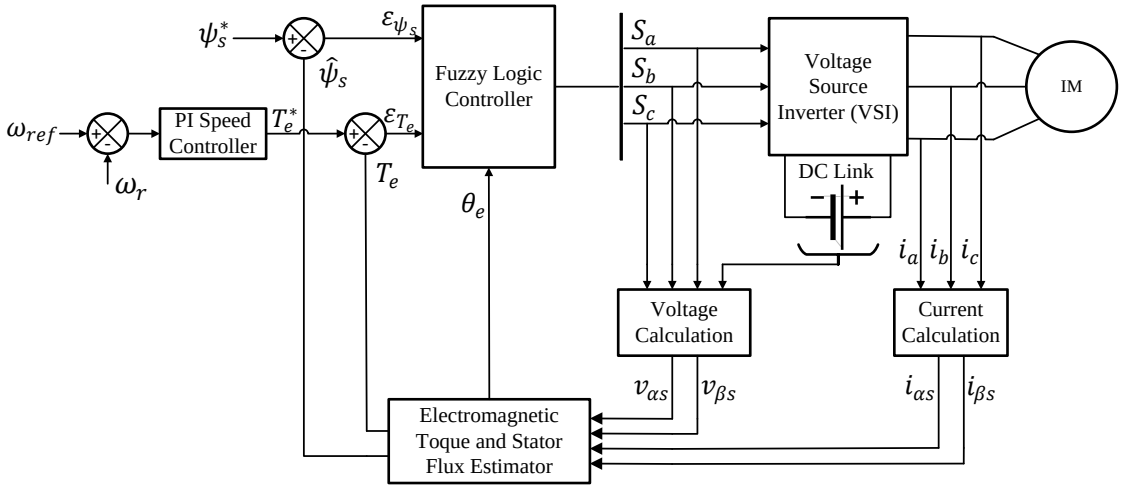

Figure 2-9: DTC with integrated fuzzy logic controller [61]

Figure 2-9 shows the proposed DTC system with an FLC (fuzzy DTC). Improvements made to the DTC system mainly focus on improved performance and mitigation of torque ripple through replacement of the torque and flux hysteresis controllers. As a result, the general structure of the DTC system remains the same, and many of the improvements which are discussed in the following sections of this chapter have a similar structure.

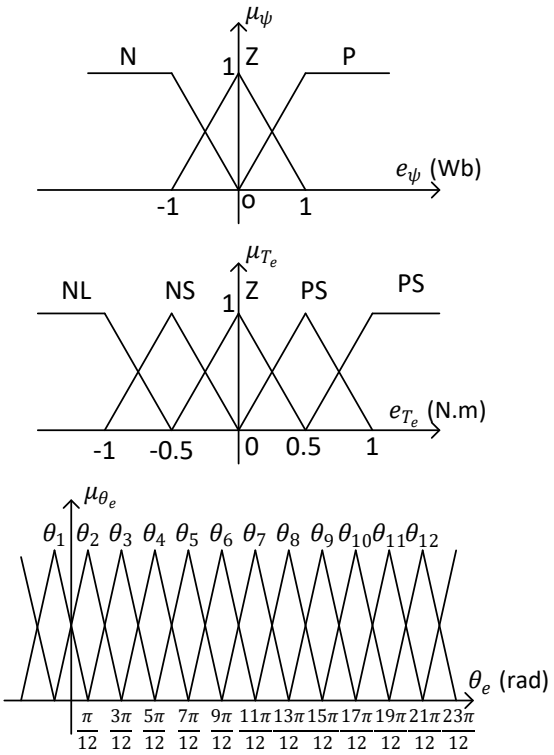

Figure 2-10: Fuzzy membership functions for conversion of input variables [61]

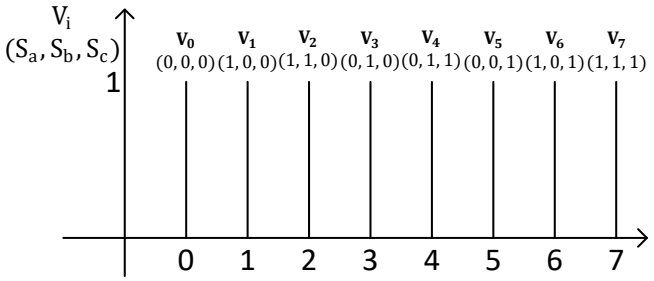

Figure 2-11: Fuzzy membership functions for conversion of the output [61]

In general, there are four principal units that form the basis of a fuzzy logic controller and are used by the authors in [61]. The units and their application to the DTC mechanism are as follows:

1. A fuzzifier – The fuzzifier converts the analogue inputs into fuzzy variables. Membership functions (MF) are used in order to produce the fuzzy variables [61]. The analogue inputs of the controller in the DTC system are the stator flux error, the torque error, and the stator flux angle. The membership functions utilised in the fuzzifier section of the controller designed by the authors in [61] are shown in Figure 2-10. It was desired to have medium stator flux variations, and as a result, three overlapping fuzzy sets were utilised, with the universe of discourse normalized to [-1, 1]. However, five overlapping fuzzy sets were utilised in the torque error MF, aiming to enable smaller torque variations [61]. Furthermore, the authors in [61] designed the fuzzy MFs with 12 fuzzy sets for the stator flux angle (usually consisting of only six sectors), allowing for more precision in the fuzzy variable selection. The stator flux angle has a universe of discourse of [0, 2π], and

the torque error has a normalized universe of discourse of [-1, 1]. Finally, the fuzzy controller output variable consists of seven singleton subsets and is shown in Figure 2-11.

2. A fuzzy rule base – The behaviour of the fuzzy system is described by the fuzzy rule base [61]. The fuzzy rules that are defined store knowledge on how the plant is to be controlled, and are designed to enable control which allows for the stator flux to be maintained at the reference value while providing a fast torque response [61]. The control rules can be described by the three input variables and the output variable, and as a result, the ith rule can be generalized by equation 2-13 [61]:

$$R_i: If\ e_\psi\ is\ A_i\ and\ e_T\ is\ B_i\ and\ \theta\ is\ C_i,\ then\ v\ is\ V_i \tag{2-13}$$

In which, A_i, B_i, and C_i represent the fuzzy set of variables e_ψ, e_T and θ, respectively. Additionally, V_i is the fuzzy singleton.

3. The fuzzy interference engine – Approximate reasoning is performed by the fuzzy interference engine through the association of the input variables with the fuzzy rules [61]. The authors in [61] propose the use of Mamdani's procedure based on min-max decision.
4. A defuzzifier – The defuzzifier aims to convert the fuzzy output of the fuzzy logic controller to an analogue value which can serve as an input to the system being controlled [61]. The authors in [61] propose the use of the Max method for defuzzification, meaning that the control output will correspond to the fuzzy output value which has the maximum possibility distribution. This defuzzification method is chosen due to the nature of the fuzzy membership functions of the output.

Figure 2-12 shows the complete fuzzy logic controller proposed by the authors in [61]. The figure depicts the four essential units in the design and control.

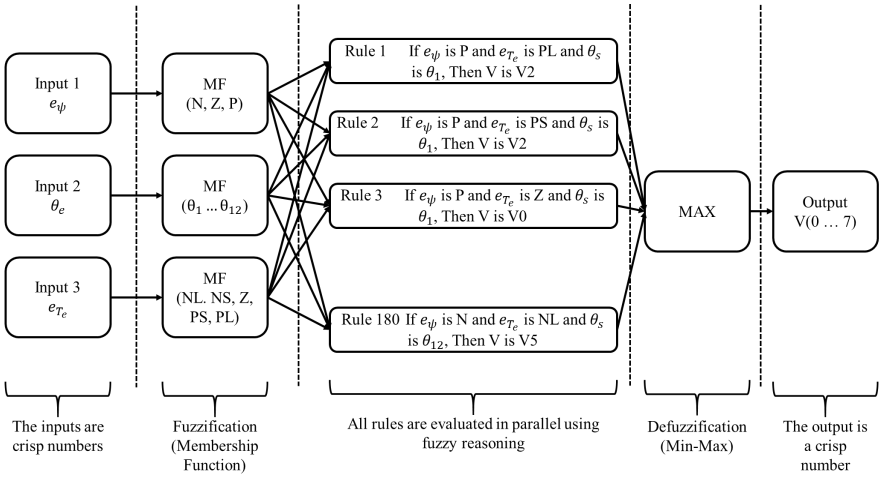

Figure 2-12: Complete fuzzy logic control system [61]

The authors in [61] provide simulations which consider a 1.5 kW motor. The simulations show that the DTC system with integrated fuzzy logic control responds better than a CDTC system. A

faster torque response is noticed, with significantly reduced torque and flux ripples. In addition, a hardware controller is designed incorporating parallel architecture, direct computation and modular architecture techniques. Interestingly, the VHDL hardware description language is utilised as a basis for the proposed design, with practical implementation of DTC with fuzzy logic again providing better dynamic results than CDTC [61]. The authors in [61] provide a good investigation, with the experimentally implemented system a noteworthy section of the article. However, the focus of the article is largely on the speed, torque and flux characteristics of the motor. Various other issues which are present in CDTC, such as high harmonic content in the input current waveforms and a variable switching frequency, are not analyzed. The improved dynamic behaviour of fuzzy DTC is concluded on the speed, torque, and flux characteristics alone.

Y. Bchir *et al.* [62] also present research on the application of fuzzy logic in a DTC scheme; however, the authors present the use of the Xilinx System Generator (XSG) toolbox in Simulink in order to carry out simulations of the proposed DTC mechanism and deployment of the control system to hardware field programmable gate arrays (FPGAs). The authors present a similar fuzzy logic control structure to that presented in [61]; however, the fuzzy membership functions used for the fuzzification of the stator flux error, the electromagnetic torque error, and the stator flux angle consist of fewer fuzzy sets. Although the use of fewer fuzzy sets simplifies the fuzzy rule base required, it also leads to less precision in the selection of the required voltage vector. Interestingly, the authors discuss the use of the XSG toolbox, which allows for algorithm development and verification in digital signal processors (DSPs) and FPGAs. Simulation of the desired system using the XSG toolbox indicated favourable stator current, stator flux and electromagnetic torque results were achieved when compared to CDTC. While the authors present a notable method of simulation and hardware implementation, they do not consider other improvements to the DTC system, such as more accurate flux and torque observers, as well as the implementation of sensorless speed control.

Fuzzy logic control can also be utilised to improve the direct torque control mechanism of a doubly fed induction motor (DFIM). Research in this area is presented by the authors in [63]. Again, the authors use fewer fuzzy sets for the fuzzy membership functions designed than was presented in [61]. However, despite the reduced precision present in the selection of the optimal voltage vectors, significant reduction in the current, flux and torque ripples can still be noticed when the proposed system is compared to CDTC. Additionally, a large reduction in the THD can also be noticed when the two mechanisms are compared. While the main contribution of the paper (reducing the issues associated with CDTC using fuzzy DTC for a DFIM in motoring mode) is achieved, the authors do not show a comparison of the proposed system with other DTC

improvements available. For instance, DTC-SVM can also provide significantly reduced ripples while maintaining the advantages of CDTC in a simpler control structure.

The authors in [64], [65] attempt to generate optimal voltage vectors for the three-phase inverter utilising a modified selection table based on a fuzzy logic controller. As seen in previous cases, the proposed method allows for the replacement of the standard switching table and hysteresis comparators present in CDTC systems, ultimately enabling improvement of the dynamic performance observed from CDTC. The use of the stator flux error, electromagnetic torque error and the stator flux position as inputs to a fuzzy-based switching table, as discussed in [61], is also discussed by the authors in [66], [67], [68]. Ideally, adequate control is desired with the use of a minimum number of fuzzy logic rules. This is achieved through the division of each input and output into a determined number of fuzzy sets.

In a similar manner to previous papers, the authors in [69] utilize a fuzzy logic controller for optimal selection of the voltage vector, which controls the inverter switching states. This is done through the replacement of the flux and torque hysteresis controllers. In addition to general performance improvement of the DTC control mechanism, the authors also aim to reduce the low-speed torque ripple present in the drive system. An interesting addition to the system is the fuzzy speed regulator, which is included to enable dynamic adjustment of the proportional and integral gains of the PI controller, based on the speed error and the rate of change of the speed. Low torque ripples, even in low-speed regions, and favourable dynamic and steady-state performance were obtained utilising the model presented.

A different approach is considered by M. Hafeez *et al.* [70], who adjust the torque hysteresis controller band limits utilising a fuzzy logic controller. Variations in the IM torque and stator current are utilised as inputs to the fuzzy logic controller in an attempt to select the optimal hysteresis controller band limits. The same approach is utilised in [71], in which both simulation-based and experimental results are presented. A comparison between the proposed fuzzy logic-based technique and conventional DTC indicated that the proposed method produced considerably lower torque ripples.

2.4.2.3. Sliding-Mode Control-Based DTC Systems

Sliding-mode (SM) control is a technique derived from variable structure control and is advantageous due to its fast and robust control nature [28], [29]. The robustness of the technique extends to variations in the machine parameters, perturbation due to the load, and omissions in the modelling of the machine [29]. SM control enables the control of nonlinear systems through the application of discontinuous control signals; however, undesired chattering caused by the

discontinuous section of the control mechanism can be observed in the quantity being controlled [28], [29]. A sliding-mode controller can be used to replace the hysteresis controllers and switching table present in conventional DTC, enabling improvements in the transient and steady-state behaviour of the system [28], [29]. Figure 2-13 shows a DTC scheme with the integration of sliding-mode control. Despite the replacement of the hysteresis controllers and conventional switching table, the general structure of the DTC system remains the same. There are various research works that consider the use of sliding-mode control to improve conventional DTC structures. The authors in [72] aim to improve the steady-state operation of CDTC with the application of a sliding-mode control approach to DTC. The new control approach is developed based on variable structure control and SVPWM and is specifically intended for application in sensorless IM drives. A robust stator flux observer, designed based on regional pole assignment theory, is incorporated into a sliding-mode-based DTC system implemented by the authors in [73]. The researchers in [74] present a sensorless sliding-mode DTC strategy intended for IM drives. The main contribution of the paper is the design of a single loop sliding-mode controller, based on an SM current control algorithm which employs two identical sliding surfaces.

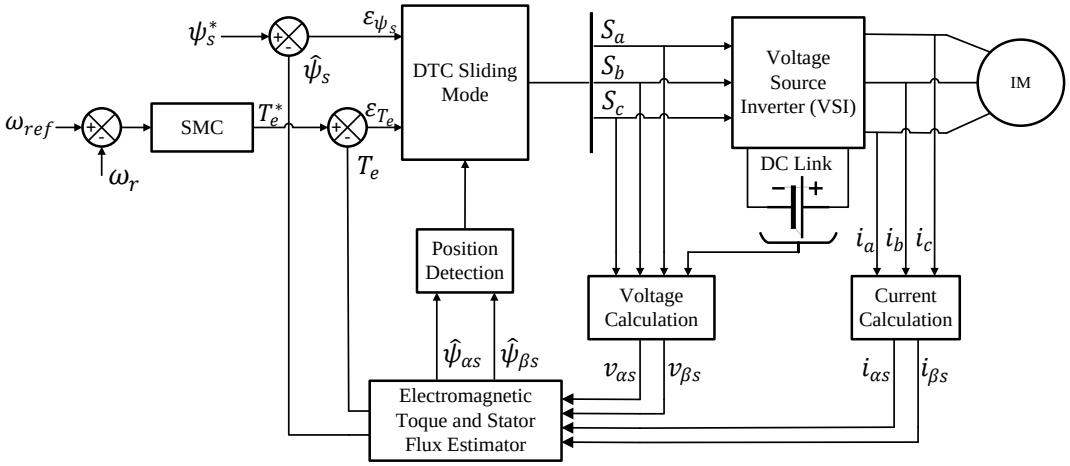

Figure 2-13: DTC with an integrated SM controller [28], [29]

Interestingly, sliding-mode control can also be used in the speed control mechanism, providing a torque reference to the DTC system. A sliding-mode speed controller is utilised by the authors in [75], in which a DTC-SVM system, fed by a three-level neutral point clamped inverter, is implemented. Further work on DTC-based sliding-mode control is completed by the authors in [76]. The technique proposed is developed using a separate sliding surface for the torque and stator flux. The torque sliding surface is based on the integral-sliding surface; however, the flux sliding surface is based on the work presented in [77]. Similarly, in [78], the authors also control the stator flux magnitude and electromagnetic torque of the motor utilising two sliding surfaces. In addition, a three-level switching vector table is utilised, enabling the implementation of the sliding-mode-based DTC mechanism proposed. The authors aim to reduce the torque, current and flux ripples with the drive presented. Synthetization of the direct torque and rotor flux control

strategies (DTRFC) making use of sliding-mode theory is attempted by the authors in [79]. Finally, the researchers in [80] provide a comparison between CDTC and DTC based on sliding-mode control for PMSM drives. The comparison is based on the starting response, torque ripple and load perturbation of the drives in question.

2.4.2.4. Artificial Neural Network Based DTC Systems

The use of Artificial Neural Networks (ANNs) can be widely applied to various applications in the field of technology and scientific research. The convenience in the use of ANNs relates to the fact that they can be used in applications in which precise mathematical approaches cannot be used to describe the problem [29], [81]. In addition, ANNs allow for a simple control architecture, insensitivity to disturbances, the ability to approximate nonlinear functions and ease of training [28], [82]. A block diagram of ANN-based DTC is shown in Figure 2-14. A large overlap can be seen when comparing ANN-based DTC to other improvements to CDTC, as the general structure of the DTC systems is the same. The ANN is integrated into the system through the replacement of the flux and torque hysteresis controllers, as well as the conventional switching table.

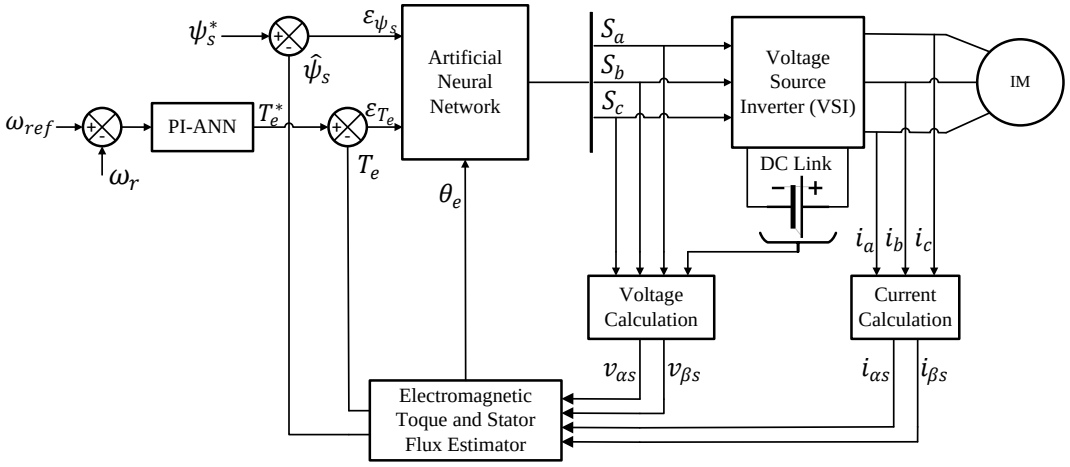

Figure 2-14: Block diagram of DTC with an integrated artificial neural network [29], [82]

There are various works that have been completed surrounding the integration of neural networks into DTC schemes. The researchers in [82] and [83] make use of ANNs in order to improve the performance of the conventional DTC scheme. Such performance improvements include a reduction in torque, flux and current ripples. Interestingly, the authors in [82] integrate an ANN into both CDTC and DTC-SVM-FTC. The results obtained indicate that the ANN DTC-SVM scheme provides improved results when compared to the other mechanisms investigated. However, a slightly different approach is taken in [83], as the authors use an artificial neural regulator in place of the conventional switching table and also implement a neural speed controller. In addition, the proposed control scheme makes use of a model reference adaptive system (MRAS) speed estimator for sensorless speed control. The results obtained by the authors indicate that the proposed scheme exhibits significant improvements when compared to CDTC. However, a comparison of the proposed scheme with other improved DTC schemes is not made.

Additionally, the authors in [84], [85] and [86] also investigate optimal vector selection strategies using ANNs, allowing for the replacement of the switching table in conventional DTC. Finally, artificial neural networks can also be used in order to estimate motor speed, providing sensorless motor control [28].

2.4.2.5. Model Predictive-Based DTC Systems

Model predictive control can enable desired improvements to the performance of CDTC systems as it allows for a reduction in torque ripple, flux ripple and switching frequency [27], [29]. In general, model predictive control calculates the future behaviour of the system in order to optimally adjust the necessary control parameters. A real-time controller makes use of a dynamic model of the process, which allows for the calculation of the future behaviour of the system [29], [87]. In general, the switching table present in CDTC is replaced with an online optimisation algorithm, which is discussed by the authors in [88], [89] and [90]. Furthermore, evaluation of a defined cost function is utilised for voltage vector selection in model predictive-based DTC [29], [91]. A block diagram of model predictive-based DTC is shown in Figure 2-15, with the electromagnetic torque, stator flux and rotor speed used to predict the future behaviour of the control variables [27], [29]. The structure of model predictive-based DTC has additional changes to the system when compared to other improvements to the CDTC mechanism. This results from both a predictive model and cost function for control output optimisation being required. The authors in [29] define three steps in which the predictive algorithm is executed, which are:

1. The estimation of variables which cannot be measured.
2. The prediction of the future behaviour of the system.
3. The use of a pre-defined cost function in order to optimize the control outputs.

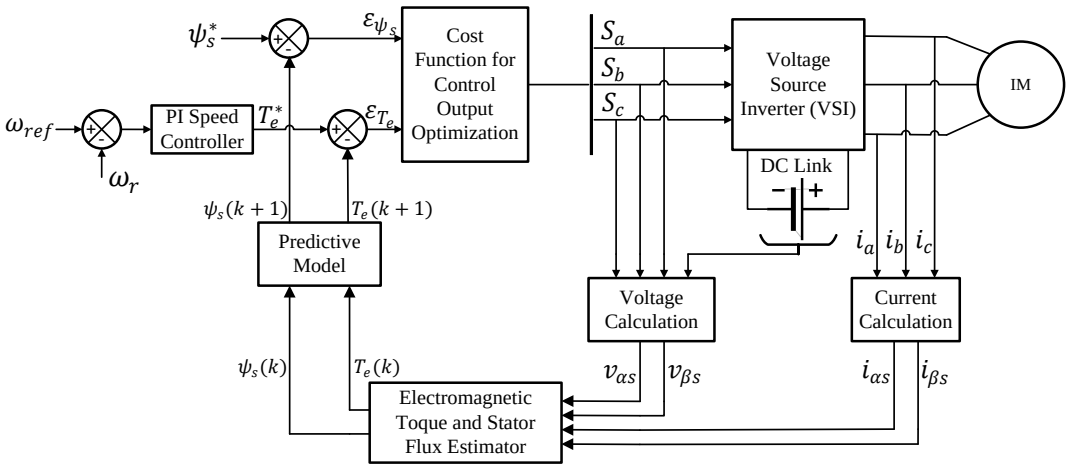

Figure 2-15: Block diagram of model predictive control-based DTC [27], [29]

The steps are repeated, considering new measurements at each sampling step. While model predictive-based DTC requires significantly more online computation in comparison to CDTC, the technique also provides various advantages. The advantages include a simple control concept,

straightforward inclusion of nonlinearities into the control model, and an easy-to-realize control methodology [27], [29].

2.5. Direct Torque Control in Electric Vehicle Applications

As detailed, there are various improvements that have been made to conventional direct torque control in order to reduce the issues associated with the control mechanism while also maintaining a fast torque response. There is a wide range of applications to which DTC techniques are applied; however, a major field of application is the traction motor control system of electric vehicles. As a result, continuous research is being carried out in the field of DTC and its application to EV drivetrains. This section aims to discuss some of the novel research carried out for DTC in EV applications.

Drivetrain efficiency is essential for extended range performance of EVs, and as a result, the authors in [15] present a new reference flux selection technique which aims to improve the efficiency of DTC IM drives that can be utilised in EV systems. The authors suggest that the technique proposed should allow for simple, practical implementation without the requirement for excessive computational resources. In addition, the technique should also be insensitive to parameter variations and free from convergence issues. DTC-SVM-FTC is employed, which includes the new reference flux selection technique proposed. In addition, a variable DC link voltage is also implemented in order to enable further performance improvements in the system. The authors chose to vary the flux and DC link voltage, as the research carried out in [92], [93], and [94] suggests that the variation of such parameters enables performance improvement of the EV drivetrain. The proposed reference flux selection technique utilises a stator current minimisation method and is chosen as it allows for maximization of the torque/ampere ratio. This is achieved through the development of a nonlinear equation for the stator current, which is essentially a function of the electromagnetic torque and stator flux. From which, the optimum values of stator flux are determined using the simulated annealing method, also allowing for a polynomial fit for optimal flux values to be generated. The proposed technique is compared to a model in which a constant flux reference is utilised, as well as a model in which a loss model technique, proposed by the authors in [94], is used in order to select the optimum reference flux value. The study indicates that the proposed technique provides a better overall system efficiency and has the lowest energy requirement during various drive cycles when compared to the other two techniques. However, only lower-speed drive cycles were tested. In addition, although the proposed method enables the implementation of field-weakening control, the authors utilize a conventional field-weakening algorithm and do not investigate maximum torque/ampere in the field-weakening region as well.

The authors in [95] also aim to improve the efficiency of EV powertrains through the presentation of a loss minimisation strategy for EVs that utilize DTC-based induction motor drives. The work presented suggests that the efficiency of the induction motor can be maximized through the selection of an optimal flux vector, which is chosen considering both the iron losses and copper losses of the motor. Initially, a detailed dynamic model of an EV is discussed as the vehicle dynamics and system architecture influence the energy efficiency of the system. The method used for the optimal reference flux selection proposed by the authors differs from the method later presented by [15], as it is based on an induction motor loss model. The loss model developed considers the copper loss in both the stator and the rotor, as well as the core loss in both the stator and rotor. The power loss, mathematically represented using the developed model, is minimised through the determination of the optimal current ratio (which consists of a ratio between the stator current components in the quadrature and direct axes). The results achieved indicate that the loss minimisation strategy proposed enables increased efficiency. However, the authors do not use a recognized drive cycle in order to show efficiency improvement. A drive cycle with a more dynamic nature, representative of urban driving conditions, would provide a more realistic representation of the increased efficiency that could be achieved. Additionally, a very small-scale model was utilised, even though it was a simulation-based study. The authors mention that increased efficiencies would be expected with larger motors; however, this is not shown, and as a result, the impact of the proposed scheme on higher power systems is not indicated.

Interestingly, conventional DTC presents advantageous properties for EV applications; however, the high torque ripple degrades the rideability and comfort of the vehicular system. These factors are prioritized as much as various technical aspects of the control mechanism in an EV, as they play a major role in the driveability of the vehicle for frequent or long periods of time. As a result of this, U. Chinthakunta *et al.* [5] propose the use of a modified torque hysteresis controller, which incorporates a multi-band error status selection method. Initially, the use of closed-loop estimators is discussed, which allows the stator flux, rotor speed and stator resistance to be estimated. A closed-loop estimator for the stator flux limits the saturation issues present with an open-loop (OL) integrator. A model reference adaptive system is used to estimate the rotor speed and stator resistance, with the authors also presenting a stability analysis of the estimator proposed. Additionally, the authors discuss the cause of the high torque ripple present in DTC systems with the conventional DTC controller, and also discuss the occurrence of flux droop in certain cases. As a result, an additional bandwidth level is proposed, which aims to minimise both the torque ripple and the flux droop. The new hysteresis controller has bandwidth levels at both $\Delta T_e/2$ and $\Delta T_e/4$, with the error status selection structure (ESS) also modified in order to include two searches for the output generation. The secondary search in the ESS structure regulates the selection of the null voltage vector and mitigates the issues of flux drooping previously present.

The proposed DTC structure is compared to other conventional hysteresis controller structures, evaluating the methods based on inverter switching frequency, current total harmonic distortion (THD), torque ripple, torque error and flux error. Various operating conditions are utilised for comparison, which include fixed and varied flux reference values, as well as fixed and varied outer bandwidth levels for the torque hysteresis controller. It was concluded that the best performance was obtained using the proposed ESS structure, with the bandwidth levels variable for certain load torque values and constant for others. While the authors present an improved hysteresis controller for CDTC, the proposed method is not compared to other improvements to the DTC system, such as DTC-SVM. Additionally, the optimal bandwidth levels are determined experimentally, which is suitable for a small-scale system. However, such determination of the optimal values may present difficulty in larger systems which are applicable for application in full-sized EV systems.

A different approach was taken by the research scholars in [96], who simulated a smaller-scale electric vehicle system which utilises CDTC and a fractional-order PI controller. The fractional-order PI controller is used as the speed controller in the proposed system and provides the torque reference to the DTC mechanism. A fractional-order PI controller was chosen by the authors in order to provide increased dynamic performance. The controller was tuned in order to minimise the integral time-weighted absolute error (ITAE). The New Europe Drive Cycle (NEDC) was used to analyse the performance of the proposed control system with a standard PI controller and the proposed fractional-order PI controller. The results obtained indicated that the fractional-order PI controller exhibited significantly less ITAE than a standard PI controller and performed adequately when tested using the NEDC. However, the authors do not present any new information or improvements to the DTC system, and as a result, the well-documented issues associated with conventional DTC can be assumed to be unresolved in the proposed mechanism presented.

Although novel DTC methodologies and optimisation techniques applied to EV powertrain systems enable further development of traction motor control mechanisms, it is also useful to provide a comparison of current techniques through a complete analysis of their performance. A comparison of such nature is provided by the authors in [97], who compare the characteristics of CDTC and DTC-SVM-FTC. The control techniques are comprehensively compared, providing results based on the efficiency, as well as the dynamic and steady-state performance of the drives, in which the speed, torque and flux linkage are investigated. Furthermore, the THD of the current and voltage, as well as the root mean square error (RMSE) of the torque, flux linkage and speed ripple are compared. Such an extensive investigation of both systems enables a determination of the suitability of the techniques for EV applications, as well as an in-depth comparison of the

techniques. Interestingly, the authors also incorporate improvements into the standard CDTC and DTC-SVM systems, which include sensorless control using a stator-current error-based MRAS, as well as efficiency optimisation techniques. The efficiency optimisation techniques employed involve the selection of optimal stator flux reference values, as well as the use of a variable DC link voltage. Selection of the optimal stator flux reference values is carried out through the use of a look-up table, which was generated using the loss minimisation strategy proposed in [94]. A thorough investigation carried out by the authors indicated that the DTC-SVM technique employed provided better performance than CDTC. The analysis carried out included the use of a small-scale vehicle model subjected to three common drive cycles, which were the New York City Cycle (NYCC), the New European Driving Cycle (NEDC), and the Delhi Driving Cycle (DDC). Although the authors present a comprehensive investigation of a small-scale system, a discussion around the changes that may occur in a large-scale system suitable for standard EV drivetrains could have added to the paper. Additionally, a comparison of the efficiencies in systems in which a fixed DC link voltage and reference flux value would also have provided further insight.

Additional work surrounding the application of direct torque control in electric vehicle applications is also presented by the research scholars in [98] and [99]. The authors in [98] present a comparison between CDTC and DTC using a multi-layer neural network. The main aim is to replace the switching table present in CDTC with a multi-layer neural network in order to minimise the issues observed in CDTC. The results show that the implemented neural network-based DTC scheme allows for significant torque and current ripple reduction compared to CDTC. While the results obtained are a notable improvement from CDTC, the authors do not investigate manners in which the efficiency of the drive can be improved through the use of optimal flux reference values or a variable DC link voltage. Additionally, common drive cycles were not utilised to simulate the conditions that vehicles may encounter in urban or high driving conditions. However, while the authors in [99] investigate a new control strategy based on DTC with the integration of sliding-mode control, their focus is not on a comparison with CDTC. The author's focus is to present a control scheme which can be utilised for a four in-wheel drive electric vehicle. The choice of a four in-wheel drive EV was made due to the improved handling that the structure can offer, with sliding-mode control-based DTC proposed in order to replace the hysteresis controller and switching table present in CDTC and minimise the associated issues. Interestingly, an important part of the work presented by the authors is the modelling of the electronic differential system proposed. The electronic differential is required to provide reference speeds for each of the four in-wheel motors based on the steering angle and throttle position. The electronic differential must provide speeds that prevent the vehicle from slipping. While favourable dynamic and steady-state speed tracking results are obtained from the simulation of

the system, a very high torque ripple can be noticed. Additionally, although the electronic differential provides reference speed values which prevent the vehicle from slipping, there are other methods of generating torque references for four in-wheel drive electric vehicles. An example of such a method is the multi-objective optimal torque distribution strategy presented by the authors in [100], which is applied to four in-wheel motor drive electric vehicles.

2.6. Field-Oriented Control

FOC offers improved dynamic control when compared to the variable-voltage variable-frequency (VVVF) method, enabling fast torque response. In addition, the amplitude, position, and frequency of the space vectors for the voltages, currents and magnetic flux can be controlled [10], [42]. FOC is applicable for high-speed operation, and sensorless speed control can be implemented when indirect FOC is utilised [42]. FOC offers reduced torque ripple compared to DTC schemes; however, FOC is not without disadvantages. It requires computationally intensive online transformations and calculations, and the control method is dependent on the parameters and speed of the induction motor, reducing the robustness of the control mechanism [42], [45].

Field-oriented control, also referred to as vector control, utilises the dynamic model of the induction motor in order to design the controller, and enables high dynamic performance to be achieved from a squirrel-cage IM. Such high dynamic performance is comparable to that seen from a DC motor [45]. Indirect or direct control methods can be utilised in FOC schemes; however, the direct control method requires accurate knowledge of the air-gap flux vector, resulting in the need for air-gap flux sensors [10], [45]. However, mechanical vibrations and temperature variations make the attachment of air-gap flux sensors impractical in the harsh operating conditions present in EV applications [10]. Furthermore, the use of sensing coils also suffers from drawbacks during low-speed operation, as sensing coils introduce inaccuracy when sensing low voltages, and they suffer from poor signal-to-noise ratio [10]. Such issues make the accurate deduction of the air-gap flux impractical at low speeds. As a result of the issues associated with direct FOC, it is not reviewed in this chapter, as it is not suitable for use in EV applications. However, indirect FOC is considered in detail.

As mentioned, the dynamic model of the induction motor is utilised in FOC, and the mathematical model of the induction motor is transformed from the stationary a-b-c reference frame to the synchronously rotating d-q reference frame. Initially, all three-phase sinusoidal quantities are transformed to the stationary α-β reference frame, using equation 2-14 [10], [42], [45].

$$\begin{bmatrix} f_{\alpha s} \\ f_{\beta s} \end{bmatrix} = \frac{2}{3} \begin{bmatrix} 1 & -\frac{1}{2} & -\frac{1}{2} \\ 0 & \frac{\sqrt{3}}{2} & -\frac{\sqrt{3}}{2} \end{bmatrix} \begin{bmatrix} f_{as} \\ f_{bs} \\ f_{cs} \end{bmatrix} \tag{2-14}$$

Following which, the variables are transformed into the rotating d-q reference frame, which rotates synchronously at a speed ω_e. The variables can be transformed from the stationary α-β reference frame to the synchronously rotating d-q reference frame utilising equation 2-15 [10], [42], [45].

$$\begin{bmatrix} f_{ds} \\ f_{qs} \end{bmatrix} = \begin{bmatrix} cos\theta_e & sin\theta_e \\ -sin\theta_e & cos\theta_e \end{bmatrix} \begin{bmatrix} f_{\alpha s} \\ f_{\beta s} \end{bmatrix} \tag{2-15}$$

Where $\theta_e = \omega_e t$. Transformation into the synchronously rotating d-q reference frame allows for the sinusoidal variables in the stationary a-b-c reference frame to be represented as DC quantities [10], [42], [45]. The dynamic equivalent circuits of the induction motor in the synchronously rotating reference frame are shown in Figure 2-16.

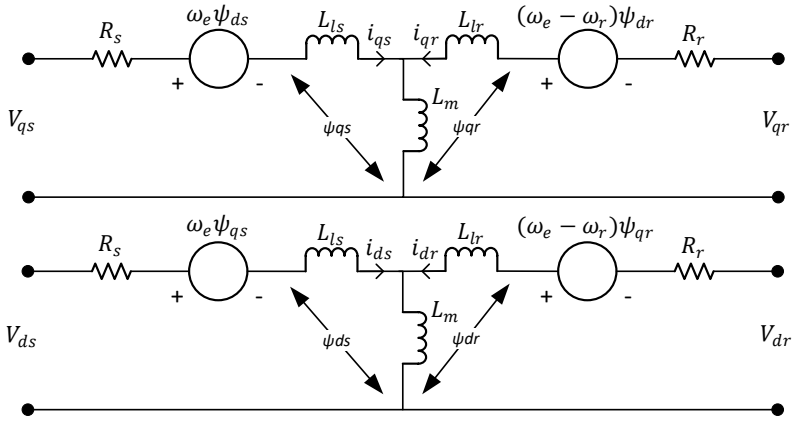

Figure 2-16: Induction motor dynamic equivalent circuits in the synchronously rotating q- and d-axes [42], [45]

The transformed variables and resulting equivalent circuit allow for the various stator and rotor voltages of the induction motor to be expressed using equations 2-16 – 2-19 [10], [42], [45].

$$v_{ds} = R_s i_{ds} + p\psi_{ds} - \omega_e \psi_{qs} \tag{2-16}$$

$$v_{qs} = R_s i_{qs} + p\psi_{qs} + \omega_e \psi_{ds} \tag{2-17}$$

$$v_{dr} = R_r i_{dr} + p\psi_{dr} - (\omega_e - \omega_r)\psi_{qr} \tag{2-18}$$

$$v_{qr} = R_r i_{qr} + p\psi_{qr} + (\omega_e - \omega_r)\psi_{dr} \tag{2-19}$$

Where in equations 2-16 – 2-19, R_s is the per-phase stator resistance, R_r is the referred rotor resistance per phase, p is the differential operator, ω_e is the synchronous speed, and ω_r is the rotor speed. In general, the rotor circuit of the induction motor is short-circuited, and as a result, v_{dr} andv_{qr} are zero. The stator and rotor fluxes can be represented in the synchronously rotating d-q axis using equations 2-20 – 2-23 [10], [42], [45].

$$\psi_{ds} = L_s i_{ds} + L_m i_{dr} \tag{2-20}$$

$$\psi_{qs} = L_s i_{qs} + L_m i_{qr} \tag{2-21}$$

$$\psi_{dr} = L_r i_{dr} + L_m i_{ds} \tag{2-22}$$

$$\psi_{qr} = L_r i_{qr} + L_m i_{qs} \tag{2-23}$$

Where in equations 2-20 – 2-23, L_s is the per-phase stator inductance, L_r is the per-phase rotor inductance, and L_m is the per-phase mutual inductance. Manipulation of the voltage and flux

equations allows for an indirect vector control structure to be developed. Interestingly, the development of the indirect field-oriented control (IFOC) equations requires alignment of the rotor flux vector (ψ_r) with the d-axis [10], [42], [45]. Figure 2-17 shows the structure of the IFOC scheme.

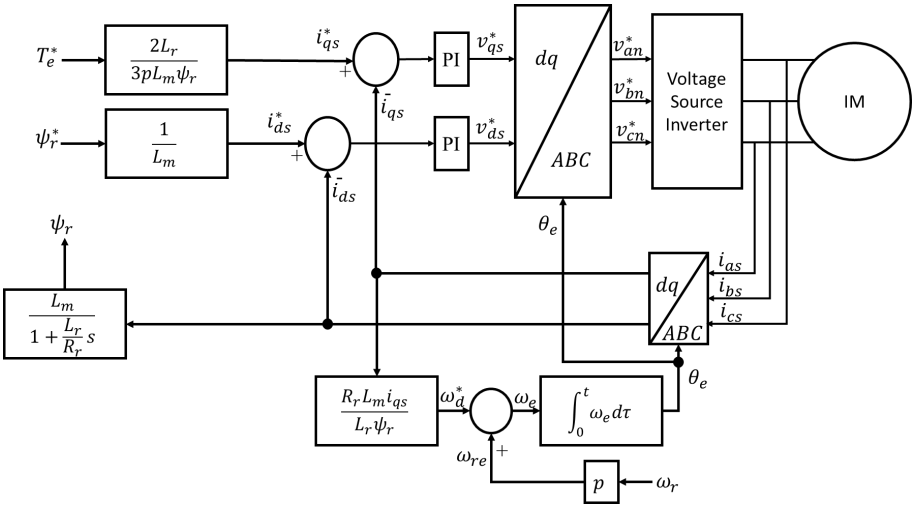

Figure 2-17: Indirect field-oriented control scheme [10], [45], [101]

The control structure of IFOC shown in Figure 2-17 indicates that it is essential for the electromagnetic torque, rotor flux, and slip speed to be defined in terms of the stator currents represented in the d-q reference frame. The electromagnetic torque in the d-q (synchronously rotating) reference frame can be expressed using equation 2-24 [10], [42], [45].

$$T_e = \left(\frac{3}{2}\right)\left(\frac{P}{2}\right)\frac{L_m}{L_r}|\overrightarrow{\psi_r}|i_{qs} \tag{2-24}$$

Where P is the number of poles in the induction motor. The d-axis rotor flux linkage can be expressed using equation 2-25 [10], [42], [45].

$$\psi_{dr} = \left(\frac{L_m}{\tau_r p + 1}\right) i_{ds} \tag{2-25}$$

Where p is the differential operator, and τ_r is the rotor time constant, which can be found as $\tau_r = L_r/R_r$. The instantaneous rotor flux position (θ_e) can be represented by equation 2-26 and requires the slip speed of the induction motor [10], [42], [45].

$$\theta_e = \int_0^t (\omega_{sl} + \omega_r) dt \tag{2-26}$$

Finally, the slip speed of the induction motor can be found using equation 2-27 [10], [42], [45].

$$\omega_{sl} = \frac{L_m R_r}{\overrightarrow{\psi_r} L_r} i_{qs} \tag{2-27}$$

Despite IFOC presenting significant advantages compared to direct FOC, there are still drawbacks associated with the conventional IFOC structure. IFOC can be utilised for high-performance induction motor drives and is suitable for use in EV applications; however, the rotor constant (τ_r) is significantly dependent on the operating temperature and magnetic saturation of the motor [10]. The rotor time constant has a dominant effect on the decoupling condition, and as a result,

variation leads to thermal degradation of the electrified powertrain performance [10], [102]. Various methods have been investigated in order to present a solution to the variation in the rotor time constant; however, there are two methods commonly utilised to solve the issue. The first method is to perform online identification of the rotor time constant, updating the parameters of the motor used in the IFOC controller accordingly. Whereas the second method is to ensure the IFOC controller is insensitive to motor parameter variations through the development of a more sophisticated and robust control algorithm [10].

2.7. Field-Oriented Control in Electric Vehicle Applications

Recently, the authors in [102] presented a notable control technique, which aims to mitigate the degradation in EV speed performance capability due to thermal effects during the operation of the vehicle. Traditionally, FOC is very dependent on the induction motor parameters, which change in EV operation due to drive cycle schedules, traffic states, temperature and vehicle loading [102], [103]. As FOC is sensitive to such changes, performance degradation can be noticed. It is as a result of this parameter variation that the authors aim to implement a robust closed-loop control technique that is largely unaffected by the temperature variation. It is indicated that sensorless speed control, which makes use of rotor flux estimation, is a key technique when aiming to minimise the impact of parameter variation. However, speed estimation is significantly dependent on the motor parameters, resulting in the need for a robust observer. The authors propose the use of a linear parameter varying (LPV) observer, suggesting that it enables robust and efficient EV operation. Prior to the design and implementation of the proposed LPV controller-observer, the authors indicate the impact of higher temperature on the speed performance of an IM. It is indicated that when full load is applied in motoring mode, lower speeds are obtained, and higher speeds are obtained when full load is applied in generating mode. As a result, the necessity of the research is apparent. The proposed technique utilises an LPV observer for speed estimation, LPV current controllers for generation of the voltage vectors to drive the inverter, and robust speed and flux controllers making use of a robust input-output feedback linearization (RIOL) approach. In addition, loop shaping utilising a mixed H_∞ sensitivity gain structure, as was proposed in [104], was utilised in order to achieve the design objectives set out. In addition to minimizing sensitivity due to parameter variation, the authors also implement the control structures and tuning in order to provide good tracking performance despite disturbances, develop noise rejection ability and handle the actuator constraints. In order to demonstrate the effectiveness of the proposed LPV controller-observer, the authors provide a comparison with high order sliding-mode control (HOSMC) based FOC and conventional FOC. The results obtained indicated that the proposed method had significantly less speed error in cases in which rotor and stator resistance variations were present. Additionally, simulation and experimental-based results indicated that the proposed LPV-FOC method performs significantly

better than conventional FOC at high temperatures when the WLTP Class 3 drive cycle is utilised as a reference speed profile. The improved performance includes better speed tracking, with lower voltage and current values required. The lower voltage and current values required increase efficiency and minimise vehicle performance degradation. While the method proposed tackles an essential issue in FOC schemes and provides improved results, the method is significantly more complicated than conventional FOC techniques. Additionally, a comparison with an equivalent DTC technique may provide interesting results, as DTC is also a major control technique for EV systems.

The review of DTC techniques applied to electric vehicles conducted in this chapter indicated that recent research works have placed a large emphasis on drivetrain efficiency and subsequent efficiency improvements through novel motor control techniques. There are also research works that discuss the efficiency of EV traction motor drive systems in which FOC is applied. J Estima *et al.* [105] provide an efficiency analysis of drivetrain topologies applied to electric or hybrid electric vehicles. While indirect field-oriented control is utilised in the research, the authors focus their attention on two drive train topologies which can be utilised in electric vehicle applications. The first is one in which a battery-powered inverter directly supplies the traction motor control mechanism, and the second includes a bidirectional DC-DC converter between the battery system and the three-phase inverter. In both cases, a PMSM is utilised as the traction motor in the vehicle powertrains. While the topology, which includes a DC-DC converter link between the battery and inverter, provides various theoretical advantages, the system may suffer from disadvantages which include additional power losses due to the DC-DC converter, increased system complexity, and increased cost. In addition to the efficiency analysis of the two topologies, the authors also propose a variable-voltage control method, which aims to improve the efficiency of the topology containing the DC-DC converter. The variable voltage control method proposed utilises the modulation index of the SVPWM technique implemented, as this allows for both the mechanical speed and PMSM load level to be taken into account. Both simulation and experimental-based results obtained by the authors suggest that the topology with a DC-DC converter provides significantly better efficiency results in conditions in which the traction motor operates at a low speed with light loads. This is commonly the case in urban drive cycles, and as a result, the authors conclude that the second topology with variable voltage control is favourable for vehicles designed mainly for urban driving conditions. Further, it was also found that the second topology provided improved voltage distortion and power factor results, leading to a possible reduction in acoustic noise. The authors present a simple variable voltage control method for a DC-DC converter that can be utilised in EV systems; however, the authors do not consider other parameters which could also be optimized to increase efficiency, such as motor flux.

W. Qinglong *et al.* [106] present a simulation and experimental-based study on the suitability of indirect field-oriented control for asynchronous traction motor drives in EV applications. The authors utilised IFOC instead of direct FOC for their investigation as it enables improved control system stability and is convenient for use in EV applications. The results obtained show that IFOC allows for high start-up torque and fast dynamic response, which makes it suitable for EV applications. However, the control structure of IFOC has been studied previously, and the authors do not suggest any further improvements that can be made. Additionally, the speed response of the structure is not discussed, and as a result, the dynamic speed response of the system is not shown. Lastly, it may have been interesting for the authors to show a comparison of the IFOC technique used with another applicable control mechanism for EV systems.

Finally, there are also various other works that have been carried out surrounding FOC for electric vehicle applications. An investigation of different speed controllers in an IFOC traction motor drive system for BEVs is presented by the authors in [107]. The use of a fuzzy logic speed controller is compared with a conventional PI speed controller, which is used to generate the torque reference for the IFOC scheme. The authors make use of the ECE-15 drive cycle in order to indicate the performance of the respective controllers, showing that the fuzzy logic controller performed favourably when considering energy consumption, speed tracking performance and energy recovery. While the results presented indicate that the fuzzy logic controller performs well in EV applications, the authors do not consider improvements to the FOC scheme itself, such as reducing the sensitivity of the scheme to IM parameter variations.

Additionally, the authors do not consider various PI controller tuning techniques, which may improve the performance of the PI speed controller. The authors in [108] work to reduce the effects of parameter variation on the IFOC scheme by presenting a back-electromotive-force (back-EMF) based MRAS estimator. The authors suggest that the proposed scheme is independent of the stator resistance and inductance parameters and also presents robustness against inverter nonlinearity. The work presented leads to the development of a sensorless torque-controlled IM drive that is suitable for application in EV systems, specifically for the purpose of fault-tolerant limp-home operation. Such operation allows an EV to operate in an acceptable manner, even in cases in which a failure or fault has occurred. This results in increased safety and reliability of the vehicle. The results obtained through experimental analysis using the proposed back-EMF-based MRAS system are desirable when considering starting from standstill, as well as forward and backward motoring operation. However, the authors only present results for a 50% change in stator resistance. Although the proposed system performs well under this operating condition, additional conditions should be discussed in order to comprehensively conclude that the proposed method is insensitive to stator resistance variations. Interestingly, field-oriented

control can also be applied to other subsystems (other than the traction motor control) in EVs. An example of this is the application of FOC to the electrical variable transmission (EVT) in hybrid electric vehicles. Such application of FOC is investigated by the research scholars in [109], in which the EVT is utilised in order to split the power to the wheels in a part directly coming from the combustion engine, and a part exchanged with the battery.

Table 2-4: Summary of FOC challenges and solutions (in EV systems)

Challenges associated with FOC	**Solution Presented**
Urban driving conditions (urban drive cycle and applicable traffic state) Light loading	A variable-voltage control technique is proposed based on the three-phase inverter modulation index. The method proposed enables improved efficiency, less voltage distortion and improved power factor results for low speeds and light loads, as are present in urban driving conditions [105] **(2012)**.
Fault-tolerant limp-home operation Temperature variation	A robust control mechanism which allows for fault-tolerant limp-home operation of an EV is developed. The mechanism is independent of the stator resistance and inductance parameters and is robust against inverter nonlinearity. A back-EMF-based MRAS estimator is used to provide independence from the stator resistance and inductance parameters. Additionally, the fault-tolerant operation incorporated enables increased vehicle safety and reliability [108] **(2017)**.
Temperature variation Drive cycle schedules Traffic states	The technique proposed ensures the IFOC scheme implemented does not suffer from degradation in speed performance due to temperature variation caused by the dynamic operating conditions of EVs. Additionally, good tracking performance is realised, and noise rejection ability is developed [102] **(2020)**.

A summary of the challenges associated with FOC techniques in EV applications, as well as the associated solutions proposed in literature, are presented in Table 2-4. FOC is dependent on the IM parameters, which change during EV operation as a result of drive cycle schedules, traffic states, temperature and vehicle loading. Subsequently, these issues are focused on in detail.

2.8. Additional Control Required in EV Systems

Although DTC and FOC form the main structure of the control mechanism, additional control should be integrated with the DTC or FOC scheme in order to ensure the desired operation of the vehicular system. Two essential control techniques which should be incorporated are field-weakening control and sensorless speed control. In many of the systems reviewed in this chapter, such techniques were easily integrated into the DTC or FOC schemes proposed.

Due to the application nature of electric vehicles, the traction motor is frequently required to run at speeds above the base speed of the motor [110]. Such high-speed operation of the traction motor allows the vehicle to meet the speed requirements of highway driving. However, the speed of the traction motor system, utilising vector control, is limited by the maximum inverter voltage and the maximum current rating of the motor windings [110]. As a result, the implementation of field-weakening control is required for operation of the traction motor above the rated speed specification [110], [111]. In order to ensure the stability of the traction motor when operating in the field-weakening region, motor torque limits must be implemented. The motor torque in the field-weakening region is limited by the DC link voltage and inverter current rating.

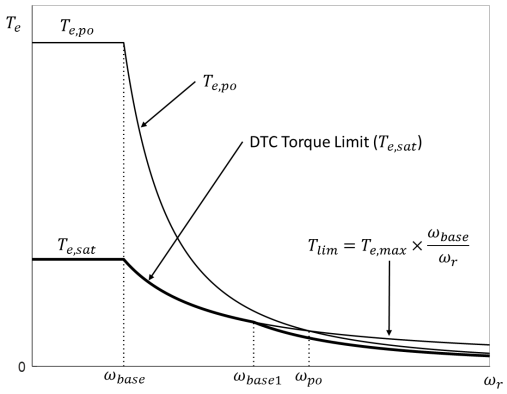

Figure 2-18: Torque limiting in the field-weakening region [111]

As a result, the authors in [111] propose a field-weakening method, which includes reference torque limiting in order to allow for stable operation of the motor, with good dynamic performance across the entire speed range of the drive. There are three regions that should be considered when operating a drive across its entire speed range. The regions, as well as the torque limits, are depicted in Figure 2-18. The torque limits are based on the maximum machine overload torque (which is extended to the field-weakening region), as well as the pull-out torque of the traction motor [111]. The maximum overload torque is depicted by $T_{e,max}$ and T_{lim} in Figure 2-18, with T_{lim} indicating the maximum overload torque in the field-weakening region. Additionally, the pull-out torque of the induction motor is represented by $T_{e,po}$ in the both the normal operating speed range and the field-weakening region. Finally, the torque limit curve which should be implemented in the control mechanism is shown in bold. The proposed method makes use of the $(1/\omega_r)$ field-weakening strategy in order to compute the stator flux reference, providing almost optimal stator flux orientation [111], [112].

There is also various other literature available which investigates field-weakening control techniques. For instance, the authors in [113] investigate maximum torque control in the field-weakening region for stator-flux-oriented induction motor drives. The authors suggest that the

conventional field-weakening method, discussed in [111], does not allow for maximum torque capability in the field-weakening region to be realised. Furthermore, flux-weakening control in the voltage extension region, which can be applied to induction motors, is presented by the authors in [114]. The authors suggest that higher torque can be achieved in the voltage extension region; however, additional torque ripple is present when operating in this region. Finally, the authors in [110] investigate field-weakening control applicable to EVs with asynchronous motor drives.

Sensorless direct torque control is advantageous in hostile environments and offers various advantages for use in EV systems. Some of the advantages include reduced hardware complexity, reduced size of the machine drive, reduced cost, less maintenance, increased reliability, and better noise immunity [115]. There are various methods that can be utilised to estimate the speed of an induction motor within a DTC or FOC mechanism, which include open-loop estimators (which use monitored stator voltages and currents), model reference adaptive systems, and estimators using artificial intelligence (neural network, and fuzzy-logic-based systems) [116], [117]. There have been various reviews conducted on sensorless control techniques for motors applicable to electric vehicle applications. The authors in [115] and [117] provide surveys on sensorless control techniques for induction motor drives. Furthermore, the authors in [118] review sensorless speed control techniques for AC drives, where their focus is also extended to PMSMs. Lastly, the authors in [37] review the sensorless speed control techniques which are applicable to EVs and HEVs.

2.9. Summary of the Motor Control Techniques Applied to EV Applications

The review presented in this chapter indicates that there are various research works that involve the application of DTC or FOC to the traction motor control system of an electric vehicle. A summary of the aims and scope of such research works is provided in Table 2-5. It is evident that there has been a large focus on drivetrain efficiency improvements in state-of-the-art research conducted recently. Such work includes efficiency comparisons between applicable control methods and novel loss minimisation strategies through the variation of stator flux and the DC link voltage. Furthermore, work continues to be done on improving the performance of DTC-based drives (to minimise ripple and harmonic distortion), and reduction of the sensitivity of IFOC-based control schemes to motor parameters. Finally, the advantages and disadvantages of each of the research works are summarized in Table 2-6.

Table 2-5: Aim/scope of research works which investigate DTC and FOC in EV applications

Reference	Year	Control Method	Aim/Scope of Work
[98]	2006	DTC	Minimisation of the issues present in CDTC through the replacement of the conventional switching table with a multi-layer neural network.
[95]	2007	DTC	Efficiency improvement of DTC-based IM drives through the use of a variable flux reference selection technique, derived from the IM loss model.
[105]	2012	FOC	The analysis of drivetrain efficiency in two different drivetrain topologies in which FOC is utilised for control of the PMSM traction motor. The drivetrain topologies analyzed include one in which the three-phase inverter is directly supplied by the battery system and another in which a DC-DC converter is utilised between the battery system and three-phase inverter. Additionally, the authors also propose a variable-voltage control technique for the second topology.
[107]	2013	FOC	The comparison of a fuzzy logic speed controller with a conventional PI speed controller for IFOC-based traction motor drive systems. The comparison is made with the use of the ECE-15 drive cycle.
[108]	2017	FOC	Reduction of the impact of motor parameter variation on the performance of an IFOC scheme for EV traction motor systems. A back-EMF-based MRAS estimator is proposed, which is independent of the stator resistance and inductance parameters. Ultimately, the IFOC system designed with a back-EMF-based MRAS estimator is developed for fault-tolerant limp-home operation of the EV.
[99]	2018	DTC	Presentation of a control scheme for a four in-wheel drive EV which utilises a sliding-mode-based DTC scheme. Additionally, an electronic differential system is proposed, which provides speed references to each of the four in-wheel motors based on the steering angle and throttle position.
[5]	2019	DTC	Improvement of vehicle rideability and comfort of the EV through the reduction of torque ripple seen in conventional DTC making use of a modified torque hysteresis controller.

			The modified torque hysteresis controller implements a multi-band error status selection method. Additionally, an MRAS estimator is used for the estimation of the rotor speed and stator resistance.
[97]	2019	DTC	A comprehensive comparison of CDTC and DTC-SVM-FTC, considering the efficiency, as well as the dynamic and steady-state drive performance. Improvements are also made to the systems for further comparison, which include the implementation of sensorless control using a stator-current error-based MRAS, as well as the incorporation of efficiency optimisation techniques.
[96]	2020	DTC	Minimisation of the ITAE in the speed response and improvement of the overall speed response of the system using a fractional-order PI controller with a CDTC scheme.
[102]	2020	FOC	Mitigation of the degradation of EV speed performance due to thermal effects during the operation of the vehicle. An LPV controller-observer is proposed in order to enable robust and efficient EV operation, ensuring the speed estimation carried out is insensitive to parameter variation.
[106]	2020	FOC	Assessment of the suitability of IFOC for asynchronous traction motor drives in EV applications.
[15]	2020	DTC	Efficiency improvement in DTC-based IM drivetrains through the use of a variable flux reference selection method, which utilises a stator current minimisation technique. A variable DC link voltage is also utilised for performance improvement.

Table 2-6: Merits/demerits of research works which investigate DTC and FOC in EV applications

Reference	Year	Control Method	Merits/Demerits
[98]	2006	DTC	It is shown that the proposed technique using a multi-layer neural network can significantly reduce the torque and current ripples noticed in CDTC. However, no efficiency improvements were investigated, and common drive cycles were not utilised in the simulation study.

[95]	2007	DTC	Efficiency improvement is obtained using a technique which considers the iron and core losses in both the rotor and the stator. However, a very small-scale simulation-based model is used without the use of common and recognised drive cycles.
[105]	2012	FOC	A comprehensive efficiency analysis between two drivetrain topologies is provided. Additionally, the variable-voltage control technique proposed is based on the three-phase inverter modulation index and therefore has a simple control structure. The method proposed enables improved efficiency, less voltage distortion and improved power factor results for low speeds and light loads, as are present in urban driving conditions. However, other efficiency optimisation techniques, such as the variation of motor flux, are not considered.
[107]	2013	FOC	The research indicates that a fuzzy logic speed controller improves the speed performance of an IFOC-based EV traction motor drive when considering energy consumption, speed tracking performance and energy recovery. However, improvements to the IFOC scheme are not considered. Such improvements may include the design of a more robust control mechanism which mitigates the sensitivity of the IFOC scheme to motor parameter variation.
[108]	2017	FOC	A robust control mechanism which allows for fault-tolerant limp-home operation of the EV is developed. The mechanism is independent of the stator resistance and inductance parameters and is robust against inverter nonlinearity. Additionally, the fault-tolerant operation incorporated enables increased vehicle safety and reliability. However, only a 50% change in stator resistance is considered in the results presented.
[99]	2018	DTC	The use of a four in-wheel drive EV enables improved handling. Additionally, the electronic differential proposed enables mitigation of slipping, with the complete system generating favourable dynamic and steady-state speed tracking results. However, high torque ripple can be noticed,

			and other control methods suitable for four in-wheel drive EVs are not compared.
[5]	2019	DTC	The multi-band error status selection method is useful in mitigating the flux droop seen in conventional DTC and also improving the overall performance of the system (torque ripple, torque error, flux error and current THD). However, optimal bandwidth levels are determined experimentally in the proposed method, which may be difficult in large-scale systems applicable to EVs.
[97]	2019	DTC	A comprehensive comparison of CDTC and DTC-SVM-FTC is given, showing their suitability for EV applications based on a wide range of factors. Additionally, the use of sensorless speed control and efficiency optimisation techniques can also be analysed. However, other DTC techniques are not compared in the study, and the changes that would occur when using a larger scale system are not discussed.
[96]	2020	DTC	The fractional-order PI speed controller proposed enables a significant reduction of the ITAE when compared to a conventional PI speed controller. Additionally, the controller performs adequately when tested using the NEDC. However, as no improvements are made to the CDTC scheme, the issues associated with CDTC are still present.
[102]	2020	FOC	The technique proposed ensures the IFOC scheme implemented does not suffer from degradation in speed performance due to temperature variation caused by the dynamic operating conditions of EVs. Additionally, good tracking performance is realised, and noise rejection ability is developed. Furthermore, a lower supply voltage and current are required when compared to conventional FOC and HOSMC-based FOC. While the method proposed enables significantly improved results, the proposed FOC scheme is significantly more complicated than conventional FOC.
[106]	2020	FOC	The suitability of IFOC in EV applications is verified. However, no additional improvements to the scheme are suggested, even though the IFOC scheme has been previously studied.

[15]	2020	DTC	Improved efficiency and lower energy requirement when compared to similar methods. The method can be implemented without the need for excessive computational resources and is insensitive to parameter variations, and is free from convergence issues. Although the method allows for maximum torque/ampere during operation below the base speed, this is not the case in the field-weakening region.

2.10. Conclusion

Electric vehicles are becoming an increasingly important component in the development of the transport industry. They provide a solution to the pollution and greenhouse gases emitted as a result of the tailpipe emissions produced by internal combustion engine vehicles. The traction motor control mechanism is an essential component in the electric vehicle powertrain, and as a result, the objective of this chapter is to review the novel and state-of-the-art improvements currently seen in electric motor control theory, which have been applied in electrified automotive systems. The review conducted indicated that recent literature has focused largely on efficiency improvements and ensuring motor parameter insensitivity in the control schemes. Such improvements ensure more efficient powertrain configurations, enabling increased vehicle range, while also ensuring that the control mechanisms developed are highly robust and reliable. Research is expected to continue in these areas as they enable significantly improved traction motor control mechanisms.

3. Chapter 3 – Methodology

3.1. Introduction

A growing interest in EV systems as a solution to the mitigation of greenhouse gas emissions and urban air pollution caused by the transport sector indicates the need for investigation into effective traction motor control systems suitable for EV applications. Furthermore, the literature review undertaken provides an indication of current works on EV traction motor control systems. Consequently, this chapter aims to provide the methodology followed for the research work undertaken in this dissertation. The methodology discusses motor selection and sizing, as well as the control techniques implemented. Focus is given to both theoretical reasoning behind design selections made and the technical operation of the control systems.

3.2. Overview of the Methodology

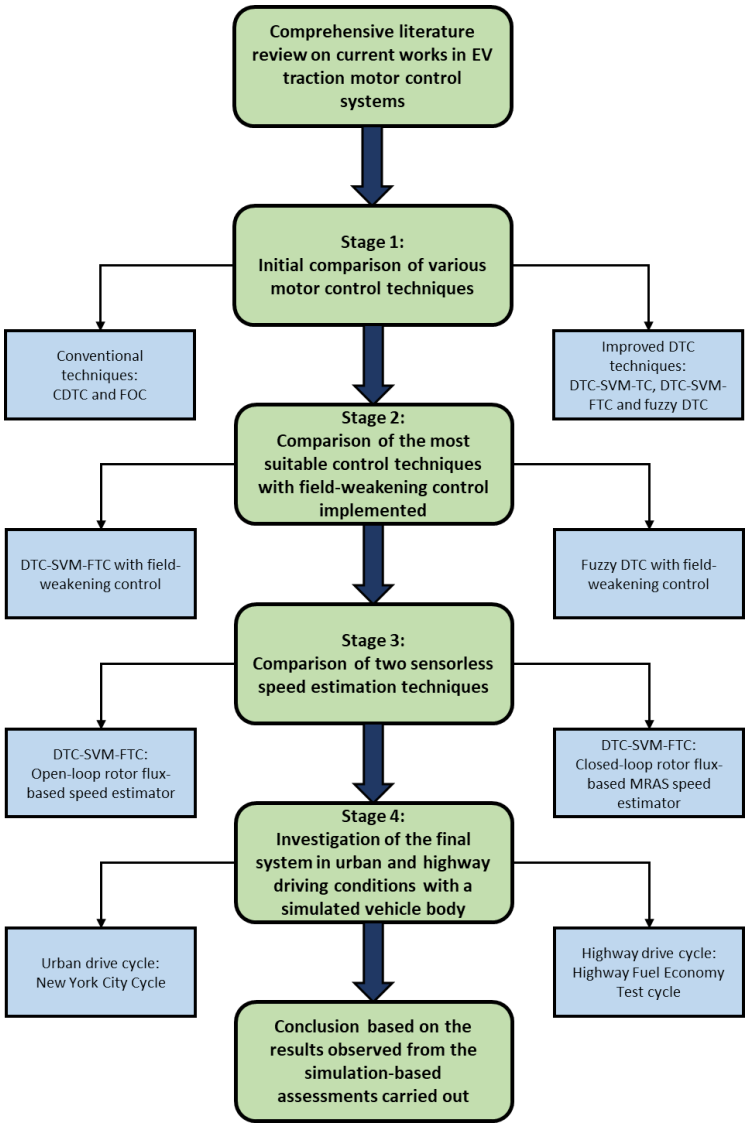

Figure 3-1: Overview of the implemented methodology

Figure 3-1 presents an overview of the methodology utilised to conduct the research work discussed in this dissertation. A comprehensive review of literature was used to understand current research works that are focused on traction motor control systems for EV applications. The simulation-based investigation carried out consists of four stages (as shown in Figure 3-1), which are as follows:

1. Stage 1 – The first stage of the investigation involves an initial comparison of various motor control techniques to determine their suitability for use in the traction motor control system of an EV. This stage investigates five separate techniques, which are conventional DTC, FOC, DTC-SVM-TC, DTC-SVM-FTC, and fuzzy DTC. Field-weakening is not included in this stage of the investigation, and as a result, the drive cycle utilised does not exceed the rated speed of the motor. The techniques investigated are assessed using the speed, torque, current and stator flux results observed, and the two most suitable techniques are extended in stage two of the investigation.
2. Stage 2 – Field-weakening control is implemented in the DTC-SVM-FTC and fuzzy DTC systems in the second stage of the investigation. The second stage aims to compare the DTC-SVM-FTC and fuzzy DTC techniques while also ensuring that the field-weakening control aspect of the control mechanisms is operating correctly. As in the first stage of the investigation, the overall system is assessed based on the speed, torque, current and stator flux results observed; however, the field-weakening control system is reviewed based on the speed tracking of the motor (with focus on speeds which are above the rated speed of the motor), the stator flux variation, and the stability of the motor throughout the drive cycle (torque limiting). One of the two methods investigated in this stage is extended for further investigation in stage 3.
3. Stage 3 – This stage of the investigation aims to assess the performance of two sensorless speed estimation techniques when integrated into the DTC-SVM-FTC mechanism. The two techniques assessed are open-loop rotor flux-based speed estimation and closed-loop rotor flux-based MRAS speed estimation. While similar metrics to those used in the first two stages are used to assess the performance of the two mechanisms, the steady-state speed error provides an important indication of the sensorless speed estimation techniques. The most favourable of the two techniques is chosen to complete the control mechanism, which is further investigated in stage 4.
4. Stage 4 – Investigation of the complete traction motor control mechanism in realistic urban and highway driving conditions is essential for accurately assessing the suitability of the control technique. As a result, stage 4 investigates the complete system using portions of the New York City Cycle and Highway Fuel Economy Test cycle (adjusted for this case study). Furthermore, a simulated vehicle body is utilised to provide accurate vehicle loads.

3.3. Electric Vehicle Parameters

Table 3-1 shows the primary parameters, and Table 3-2 the dynamic specifications of the prototype vehicle investigated in this dissertation. The primary parameters and specifications are based on current literature in which designs were carried out, as well as four/five-seater electric vehicles that are currently being manufactured and are available [36], [119], [120], [121].

Table 3-1: Primary parameters of the prototype vehicle

Primary Parameter	Value	Primary Parameter	Value
Curb mass (kg)	1150	Rolling resistance coefficient	0.015
Gross mass (kg)	1400	Front area (m^2)	2.300
Rolling radius (m)	0.300	Aerodynamic drag coefficient	0.275

Additionally, the dynamic performance specifications are also based on everyday use in urban areas and highways; for example, the maximum highway speed limit is 120 km/h, and a 0-100 km/h acceleration time of less than 15 seconds is acceptable for smaller cars used for transportation [122].

Table 3-2: Dynamic performance specifications of the prototype vehicle

Dynamic Performance Specification	Value
Maximum speed (km/h)	≥130
0-100 km/h acceleration time (s)	≤15
Maximum Gradeability (%)	≥30 (at 20 km/h)

3.4. Electric Motor Parameter Matching

Electric motors are used as traction motors in electric vehicles, enabling the transformation of electrical energy into mechanical energy [36]. As a result of this, the dynamic performance characteristics of an EV are directly determined by the performance of the traction motor [36], [119]. In order for a suitable traction motor to be selected, various motor parameters, including the rated power, maximum power, base speed, maximum speed, and maximum torque, must be determined [36]. Initially, the type of motor being utilised in the study must be selected. Current EV drives can be evaluated in order to determine a suitable motor for the investigation being carried out.

The authors in [17], [123], [124] and [125] investigate the advantages and disadvantages of different motors based on various parameters. An evaluation of the motors based on this research is shown in Table 3-3. The evaluation rates each motor based on various metrics, with each metric carrying a maximum score of 5. Each metric is weighted equally to determine an average rating for each motor out of 5. Currently, induction motor and PMSM-based EV drives are the most commonly used, representing the majority of the vehicles available on the market [17], [14], [123]. The current use of such motors in commercially available vehicles corresponds to the evaluation undertaken in Table 3-3, in which induction motor and PMSM drives were found to be the most favourable. As a result of this comparison, an induction motor was chosen for use in this investigation due to its controllability, reliability, and cost.

Table 3-3: Evaluation of the motors used in EV drivetrains [17], [123], [124], [125]

Parameter	**Motor Type**				
	DC	IM	SRM	PMSM	PM BLDC
Power Density	2.25	3.5	3.5	4.75	5
Efficiency	2.25	3.5	4	4.75	5
Controllability	5	4.5	3	4	4
Reliability	3	5	5	4	4
Maturity	5	4.75	3.75	4.5	4
Cost Level	4	5	4	3	3
Noise Level	3	5	2	5	5
Maintenance	2	4.5	4.5	4.5	5
Speed Range	2.5	4	4.5	4.5	4
Robustness	3	5	4.5	4	4.25
Size and Weight	3	4	4	5	4
Average	**3.18**	**4.43**	**3.89**	**4.36**	**4.30**

In order to determine the specifications of the selected motor, the maximum power of the motor must first be determined. The peak power of the motor must enable it to satisfy various vehicle specifications, which are the maximum velocity of the vehicle, the climbing performance of the vehicle, and the 0-100km/h acceleration time of the vehicle [36], [119], [120], [126]. The authors in [36], [119], [120] and [126] propose a method of parameter matching to allow for the motor specifications to be determined. The proposed method is utilised for the parameter matching carried out in this investigation. Equation 3-1 determines the power required for the vehicle to meet its maximum speed specification [36], [119], [120], [126].

$$P_{maxspeed} = \frac{1}{3600\eta_t}\left(mgfv_{max} + \frac{C_D A v_{max}^3}{21.15}\right) \quad (3\text{-}1)$$

Equation 3-2 determines the power required for the vehicle to meet its climbing performance (gradeability) specification [36], [119], [120], [126].

$$P_{climbing} = \frac{1}{3600\eta_t}\left(mgfv_c \cos\alpha_{max} + mgv_c \sin\alpha_{max} + \frac{C_D A v_c^3}{21.15}\right) \quad (3\text{-}2)$$

Equation 3-3 determines the power required for the vehicle to meet its 0-100 km/h acceleration time specification [36], [119], [120], [126].

$$P_{acceleration} = \frac{1}{3600 t_m \eta_t}\left(\delta m \times \frac{v_m^2}{7.2} + mgf \times \frac{v_m}{1.5} \times t_m + \frac{C_D A v_m^3}{21.15 \times 2.5} \times t_m\right) \quad (3\text{-}3)$$

Where in equations 3-1 – 3-3; η_t is the driveline efficiency (measured from the power source to the driven wheels), the vehicle mass (kg) is represented by m, g represents the gravitational acceleration (9.80 m/s^2), the front area of the vehicle (m^2) is denoted by A, f represents the tyre rolling resistance coefficient, C_D is the aerodynamic drag coefficient, the maximum velocity of the vehicle (km/h) is given by v_{max}, α_{max} represents the maximum grading angle of the vehicle (rad), v_c is the climbing/grading velocity of the vehicle (km/h), δ is the rotational inertial factor of the vehicle, t_m is the specified 0-100 km/h acceleration time of the vehicle (s), v_m is the final acceleration speed (km/h) and ρ_a is the air density (1.202 kg/m^3).

As mentioned previously, the maximum power of the motor must be able to meet the power requirements in equations 3-1 – 3-3. As a result, the maximum power required from the motor can be given by equation 3-4 [36], [119], [120], [126].

$$P_{max} \geq \max\left[P_{maxspeed}; P_{climbing}; P_{acceleration}\right] \quad (3\text{-}4)$$

The rated power specification of the motor can be determined from the maximum power specification and the overload factor of the traction motor used in the vehicle. The authors in [127] and [128] discuss the overload capabilities of traction motors in electric vehicles. The ability for the traction motor to be overloaded for short periods of time (to meet the maximum power requirements) allows for a smaller motor to be chosen, translating to lower vehicle power consumption [127], [128]. Based on the discussions carried out by the authors in [36], [120], [127] and [128], a maximum overload factor of 1.5 (50% overload) was chosen for this investigation. As a result, the rated power of the traction motor required can be found using equation 3-5 [36], [119], [120], [126].

$$P_{rated} = \frac{P_{max}}{k} \; and \; P_{rated} > P_{maxspeed} \quad (3\text{-}5)$$

In which k is the overload factor chosen. In addition to the maximum and rated power specifications of the motor, the maximum speed of the motor must also be determined. The maximum speed specification of the motor can be determined through the use of equation 3-6 [36], [120], [126].

$$n_{max} = \frac{v_{max} i_0}{0.377r} \tag{3-6}$$

Where; v_{max} is the maximum velocity of the vehicle, i_0 is the gear ratio (utilising a fixed gear system in the electric vehicle), and r is the rolling radius. The gear ratio can be chosen and is not calculated specifically. However, the ratio has a minimum value which is required in order for the vehicle to meet its gradeability performance specification. This minimum limit is given in equation 3-7 [36], [119], [120].

$$\frac{r}{\eta_t T_{max}} \left(mgfcos\alpha_{max} + mgsin\alpha_{max} + \frac{C_D A v_c^2}{21.15} \right) \leq i_0 \tag{3-7}$$

In which, T_{max} is the maximum torque of the motor. All of the other parameters in equation 3-7 have been previously defined. The maximum torque of the motor can be found using equation 3-8 [119], [129].

$$T_{max} = \frac{9.55 P_{max}}{n} \tag{3-8}$$

In which n is the rated speed of the motor. Utilising equations 3-1 – 3-8, the required traction motor specifications can be determined. The required specifications are shown in Table 3-4 and are based on research articles [36], [119], [120] and [126]. Notably, the maximum speed required is approximately 2.7 times the base speed of the induction motor. A motor control scheme with field-weakening implemented allows the motor to operate at speeds above its base speed; as a result, the maximum speed requirement calculated is achievable [45]. The specifications of the induction motor selected for use in this investigation, meeting the specifications shown in Table 3-4, are given in Appendix A, Table A-1.

Table 3-4: Required traction motor specifications

Parameter	Value	Parameter	Value
Maximum Power	55 kW	Maximum Speed	8046 rpm
Motor Overload Factor	~1.5	Maximum Torque	177.72 N.m
Rated Power	37 kW	Gear Ratio	7
Base Speed (Rated Speed)	3000 (2952) rpm		

3.5. Traction Motor Control Techniques

3.5.1. Selection of Applicable Traction Motor Control Techniques for Investigation

The electric machine and drive system in an EV powertrain are essential for enabling the dynamic performance specifications of the EV to be met. As these are core technologies in the EV powertrain, adequate operation of the vehicle requires a correctly designed and implemented traction motor control circuit [14], [17], [25]. As an induction motor was selected for use in this investigation (from the evaluation carried out in Table 3-3), there are three control methods that

can be considered, which are variable-voltage variable-frequency (VVVF) control, field-oriented control (FOC) and direct torque control (DTC) [10], [14], [17].

The VVVF mechanism is a relatively simple method of control and implementation, which is widely used in various applications found in industry [10]. It is advantageous as it enables the electromagnetic torque capability of the induction motor to be maximised [42]. However, the VVVF method has some disadvantages in EV applications. The torque is not directly controlled, and as a result, the torque control provided in VVVF control is not fast or accurate enough for high-performance EV applications [10], [42], [45]. Additionally, field orientation is not utilised, and the motor status is ignored [42].

Improved dynamic control and a fast torque response, when compared to the VVVF method, can be achieved with the use of FOC. Furthermore, various other parameters can be controlled, which include the amplitude, position and frequency of the space vectors for the voltages, currents and magnetic flux [25], [10], [42]. High-speed operation can be achieved with the use of FOC, with sensorless speed control operation also possible in indirect FOC systems [25], [42]. Lower torque ripple can be achieved in FOC schemes when compared to the performance of DTC-based systems; however, there are also certain disadvantages associated with the FOC mechanism. The robustness of the control mechanism is impacted as a result of the dependence of FOC schemes on the parameters and speed of the induction motor. Additionally, various calculations and transformations must be carried out during the operation of the control mechanism (online), meaning FOC is a computationally intensive control method [25], [42], [45].

Similar performance to that observed in FOC schemes, without the need for intensive online coordinate transformations, can be achieved with the use of DTC [10], [25], [27]. Additionally, as direct control of the motor torque is possible in DTC, a fast torque response is achieved without the requirement for the feedback current control performed in FOC [10], [25], [27]. Furthermore, realistic urban (frequent starting/stopping and acceleration) and highway (high-speed operation) driving requirements can be met with the use of DTC, with more advanced DTC mechanisms also allowing for sensorless speed control [25], [27]. However, despite the benefits that DTC provides, conventional direct torque control (CDTC) structures suffer from high torque and current ripple, with a slower start-up response also noticeable [10], [27], [42]. High noise levels and challenging control at low speeds are also introduced due to the variable switching frequency present in CDTC mechanisms [25], [27], [42].

As a result of the characteristics of the applicable motor control techniques discussed, both FOC and DTC were preferred for investigation in the traction motor control mechanism being

investigated in this dissertation. Both techniques offer significant advantages over the VVVF method, which is unlikely to offer adequate performance for the vehicle system being investigated. Certain methods of FOC and DTC implementation also allow for speed estimation from sensed stator voltages and currents, eliminating the requirement for mechanical speed sensors at the motor shaft, thereby reducing the cost of the traction motor control system [27]. As a result, the techniques allow for a reduced size of the motor drive, reduced hardware complexity, improved noise invulnerability, increased reliability, and less maintenance [27]. High-speed operation, as well as frequent starting/stopping and acceleration, are performance requirements the EV traction motor should be able to satisfy. Dynamic operation of the motor, as well as robust flux weakening control, can be achieved with the use of both FOC and DTC schemes [25], [27].

3.5.2. Conventional Direct Torque Control

The conventional DTC system discussed in this chapter is based on the block diagram shown in Figure 2-3 and uses hysteresis control to ensure the desired electromagnetic torque and stator flux magnitude values are achieved. As a detailed methodology of the CDTC algorithm is provided in the literature review (section 2.4.1), the equations and general algorithm overview are not presented again in this section. However, it is important to note the hysteresis controller band limits and the inverter input voltage used in the conventional DTC system implemented in this dissertation.

The operation of the torque and flux hysteresis controllers are defined by equations 2-8 and 2-9, respectively. As DTC mechanisms directly control the electromagnetic torque, a PI speed control loop is required to obtain the desired speed. A torque reference corresponding to the desired speed is generated by the PI controller in the speed control loop. The authors in [130] discuss conventional values for the hysteresis controller band limits and suggest that the limits can be adequately determined using equations 3-9 and 3-10.

$$h_{T_e} = 8\%\, T_{e_N} \tag{3-9}$$

$$h_{\psi} = 2\%\, \psi_{s_N} \tag{3-10}$$

In which, h_{T_e} and h_{ψ} are the torque and stator flux hysteresis controller band widths respectively, and T_{e_N} and ψ_{s_N} are the nominal torque and stator flux values of the induction motor being utilised in the system. The hysteresis controller band limits implemented in this investigation were chosen based on the discussion provided by the authors in [130]; however, the values used were adjusted due to the nature of the vehicle system in this dissertation. Table 3-5 indicates the parameter values used in both the speed PI controller as well as the torque and flux hysteresis controllers. The stator flux hysteresis controller limits the maximum and minimum values of the stator flux, resulting in a circular stator flux trajectory created by the boundaries of the hysteresis band (seen in Figure 2-5) [42]. The stator flux hysteresis controller has very little impact on the

torque ripple, which is controlled mainly through the torque hysteresis band. In general, the torque ripple responds proportionally to changes in the limits of the torque hysteresis band; however, lower torque hysteresis band limits result in an increased switching frequency and proportional increase in inverter switching losses [42].

Table 3-5: CDTC model parameters

Parameter	Value
Torque Hysteresis Controller Band Limits (HB_{Te})	Lower Limit = -3 Upper Limit = 3
Flux Hysteresis Controller Band Limits (HB_{ψ})	Lower Limit = 0.005 Upper Limit = 0.005

Adequate operation of the DTC system requires that a certain DC voltage level can be supplied to the inverter, which must also be calculated. The minimum DC link voltage for the operation of an SVPWM switching scheme-based inverter in the linear modulation region is found using equation 2-10. Notably, circular flux trajectory DTC can also be achieved while operating the inverter in the overmodulation range; however, linear modulation is used in the investigation provided in this dissertation. Based on the findings in [44] (equation 2-10), the modulation index and DC link values applicable to the DTC mechanism implemented in this investigation are shown in Table 3-6. A DC link voltage of 10% greater than the minimum voltage required for operation in the linear modulation region was used to supply the three-phase inverter.

Table 3-6: Overmodulation and DC link parameters for the CDTC control mechanism

Parameter	Value
Linear range modulation index	$0 < m_i \leq \sim 0.907$
Maximum modulation index for Overmodulation	0.950
Minimum DC Voltage required for linear modulation	565.62 V
Implemented DC supply voltage (10% greater than the minimum)	622 V
Sampling Frequency	500 kHz

3.5.3. Improved DTC Mechanisms

The researchers in [10], [27], and [45] highlight the disadvantages associated with the conventional direct torque control structure as a result of the use of hysteresis controllers, as well as the variable switching frequency of the system. Such disadvantages, including high electromagnetic torque, stator flux and current ripples, have led to extensive research into the improvement of conventional DTC. The characteristics of the improved methods developed in comparison to conventional DTC are shown in Table 3-7. The methods reviewed in Table 3-7 are space vector modulation-based DTC (DTC-SVM), model predictive-based DTC (MPC-DTC), fuzzy logic-based DTC (fuzzy DTC), artificial neural network-based DTC (ANN-DTC) and sliding mode control-based DTC (SMC-DTC).

Table 3-7: Comparison of improvement techniques for DTC systems [27], [28], [29]

Metric	CDTC	DTC-SVM	MPC-DTC	Fuzzy DTC	ANN-DTC	SMC-DTC
Dynamic torque response	Fast	Fast	Fast	Very Fast	Very Fast	Fast
Torque and flux ripple	High	Low	Low	Very Low	Very Low	Medium
Current THD	High	Lower	Lower	Lower	Lower	Lower
Switching Frequency	Variable	Constant	Constant	Constant	Constant	Almost Constant
Computation time	Low	Medium	Medium	High	High	High
Switching Loss	High	Low	Low	Low	Low	Medium
Algorithm Complexity	Simple	Simple	Simple	More Complex	More Complex	Complex

In addition to the conventional DTC mechanism discussed, the DTC-SVM and Fuzzy DTC techniques were chosen for investigation in this dissertation. The DTC-SVM technique enables improved performance (reduced ripples, reduced current distortion, and constant switching frequency) with simple algorithm complexity, while the Fuzzy DTC technique offers further improved ripple and dynamic torque response performance. However, the Fuzzy DTC technique has a higher algorithm complexity and computation time when compared to DTC-SVM. The objective of the implementation of these two advanced DTC mechanisms is to mitigate the issues observed in the conventional DTC system. However, there are various other suitable control methods given in Table 3-7, which could also have been chosen. SMC-DTC was avoided as it has higher switching losses, a larger required computation time, and a more complex algorithm construction. In addition, sliding mode control can cause undesired chattering in the quantity being controlled as a result of the discontinuous section of the control mechanism [25]. Table 3-7 indicates that MPC-DTC has very similar performance characteristics to the DTC-SVM technique chosen in this chapter. However, MPC-DTC requires both the use of a predictive model (to predict the future behaviour of the system) as well as a pre-defined cost function, which allows for optimisation of the control outputs [25]. Furthermore, the authors in [29] suggest that hysteresis regulation is used in conventional MPC-DTC. In comparison, DTC-SVM makes use of a PI controller with fundamental motor and DTC calculations, whereas fuzzy DTC uses fuzzy membership functions for the selection of the inverter switching states. A method not evaluated in Table 3-7 is deadbeat control-based DTC schemes. Deadbeat control utilises different control

strategies in steady state and transient operation; however, the researchers in [46] suggest that deadbeat control is sometimes not feasible due to the limitation of inverter voltages and currents.

3.5.3.1. DTC-SVM-TC

DTC-SVM techniques correctly select switching states for the voltage source inverter with the implementation of a voltage modulator [49]. As a result, the hysteresis controllers and switching table utilised in CDTC systems are no longer required in DTC-SVM. However, the hardware topology present in DTC-SVM is still similar to that utilised in conventional DTC [28]. As with conventional DTC, only the stator parameters of the IM are required for adequate operation of the DTC-SVM system. The implemented SVM technique aims to allow for reduced torque/flux ripples and harmonic distortion in the current waveform through optimal selection of the inverter switching states and maintaining a constant switching frequency. This dissertation focuses on two of the three different variations of the DTC-SVM control structure, which are DTC-SVM using closed-loop torque control, and DTC-SVM using both closed-loop torque and flux control [28].

The DTC-SVM closed-loop torque control structure proposed for investigation has been discussed previously in the literature review provided (section 2.4.2.1), with a block diagram of the mechanism shown in Figure 2-7. As a result, the methodology for implementation of the mechanism will not be provided again in this chapter. However, Table 3-8 shows the necessary parameters used for the implementation of the DTC-SVM-TC mechanism in this dissertation.

Table 3-8: Parameters used in the implementation of the DTC-SVM-TC mechanism

Parameter	Value
Torque PI Controller	$P = 0.01$
	$I = 2$
Implemented DC supply voltage (10% greater than minimum)	622 V
SVPWM Switching Frequency	20 kHz
Sampling Frequency	500 kHz

3.5.3.2. DTC-SVM-FTC

The DTC-SVM-TC structure presents a useful strategy to improve the performance obtained from a CDTC mechanism and requires only a single PI controller for the control of the inverter switching states. However, as only one PI controller is implemented, the stator flux is controlled in an open-loop manner [50]. Issues introduced due to the open-loop control of the stator flux are solved with the use of the DTC-SVM-FTC mechanism, which implements a second PI controller to allow for closed-loop control of the stator flux. Stator flux coordinates are used for the DTC-SVM-FTC mechanism investigated in this dissertation, with a block diagram of the control structure shown in Figure 2-8. The stator flux and torque errors are used as inputs to the flux and

torque PI controllers, respectively, from which stator reference voltage components in the rotating d-q reference frame are generated. The DC voltage commands in the rotating d-q reference frame are then transformed into the stationary α-β reference frame, with the α-β components used to generate the SVM switching scheme to control the voltage source inverter [28], [46], [50]. The transformation from the rotating d-q reference frame to the stationary α-β reference frame is shown in equation 3-11 [10], [42].

$$\begin{bmatrix} f_{\alpha s} \\ f_{\beta s} \end{bmatrix} = \begin{bmatrix} cos\theta_e & -sin\theta_e \\ sin\theta_e & cos\theta_e \end{bmatrix} \begin{bmatrix} f_{ds} \\ f_{qs} \end{bmatrix} \tag{3-11}$$

Furthermore, the authors in [57] present a method in which the flux and torque PI controllers can be designed using the Symmetric Optimum Criterion, based on a simplified induction motor model. The research indicates that the flux PI controller values can be approximately determined using equations 3-12 and 3-13 [57].

$$K_{p\psi} = \frac{1}{2T_s} \tag{3-12}$$

$$T_{i\psi} = 4T_s \tag{3-13}$$

In which, $K_{p\psi}$ and $T_{i\psi}$ are the proportional gain and integral time constant of the flux PI controller, respectively, and T_s is the sample time of the control system. The integral time constant of the torque PI controller can also be determined using equation 3-13; however, the authors use an experimental method in order to determine the proportional gain of the torque PI controller [57]. While the methodology and equations suggested in [57] were considered for the design of the PI controllers in the DTC-SVM-FTC mechanism investigated in this dissertation, it was found that the equations resulted in very high proportional and integral gains which impacted the voltage waveform supplying the traction motor used. As a result, the gains used were adjusted to improve the response of the mechanism implemented. The necessary parameters used for the implementation of the DTC-SVM-FTC mechanism in this dissertation are shown in Table 3-9.

Table 3-9: Parameters used in the implementation of the DTC-SVM-FTC mechanism

Parameter	**Value**
Flux PI Controller	$P = 50$
	$I = 25$
Torque PI Controller	$P = 0.2$
	$I = 100$
Implemented DC supply voltage (10% greater than the minimum)	622 V
SVPWM Switching Frequency	20 kHz
Sampling Frequency	500 kHz

3.5.3.3. Fuzzy DTC

A fuzzy DTC system enables reduced torque and flux ripple when compared with CDTC through the replacement of the hysteresis controllers and switching look-up table with a fuzzy logic controller. However, despite this, the general structure of the DTC system remains the same [61]. The block diagram of the fuzzy DTC mechanism implemented in this dissertation is shown in Figure 2-9, with a detailed methodology of the implementation of general fuzzy DTC systems also provided in the literature review (section 2.4.2.2). As a result, the basic methodology is not repeated in this section.

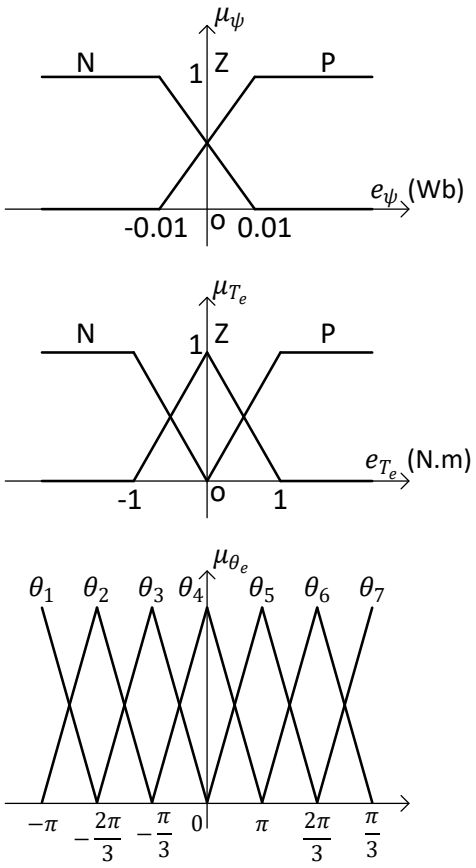

Figure 3-2: Implemented fuzzy membership functions for conversion of input variables [61], [62], [63]

However, discussing certain aspects of the principal units implemented in the fuzzy logic controller used for DTC investigated in this dissertation is essential. The implementation of the fuzzy logic controller is based on the research carried out by the authors in [61], [62] and [63], with the implementation of the four principal units of the fuzzy logic controller as follows:

1. The fuzzifier, which utilises fuzzy membership functions to convert analogue inputs into fuzzy variables, receives the flux error, torque error and stator flux angle as analogue inputs. The fuzzy membership functions used in the implementation of the controller are shown in Figure 3-2. The flux and torque error membership functions contain two and three overlapping fuzzy sets, respectively.

2. The fuzzy rule base, which describes the behaviour of the fuzzy controller, is defined in Table 3-10. The fuzzy rule base is defined to ensure a fast and stable torque response while also allowing the system to maintain the stator flux at the reference value.
3. The fuzzy inference engine implemented utilises Mamdani's procedure based on min-max decision in order to perform approximate reasoning through the association of the input variables with the fuzzy rule base.
4. The defuzzifier, which aims to convert the fuzzy output of the controller to an analogue signal which can be used in the DTC mechanism, utilises the smallest of maximum (SOM) method for defuzzification. The output fuzzy membership function is comprised of seven singleton subsets and is shown in Figure 3-3.

Table 3-10: Implemented fuzzy rule base [61], [62], [63]

e_ψ	e_{T_e}	θ_1	θ_2	θ_3	θ_4	θ_5	θ_6	θ_7
P	**P**	V_2	V_3	V_4	V_5	V_6	V_1	V_2
	Z	V_7	V_0	V_7	V_0	V_7	V_0	V_7
	N	V_6	V_1	V_2	V_3	V_4	V_5	V_6
N	**P**	V_3	V_4	V_5	V_6	V_1	V_2	V_3
	Z	V_0	V_7	V_0	V_7	V_0	V_7	V_0
	N	V_5	V_6	V_1	V_2	V_3	V_4	V_5

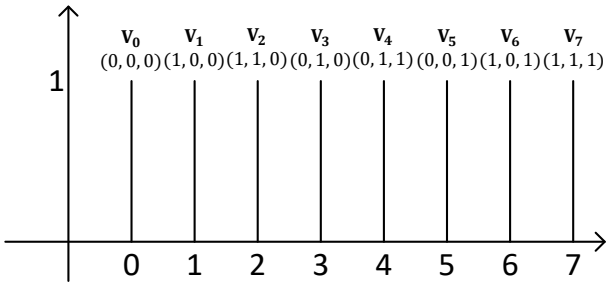

Figure 3-3: Implemented fuzzy membership functions for conversion of the output [61], [62], [63]

3.5.4. Field-Oriented Control

The field-oriented control system discussed in this chapter is based on the block diagram shown in Figure 2-17. As a detailed methodology of the FOC algorithm is provided in the literature review (section 2.6), the equations and general algorithm overview are not presented again in this section. However, it is important to note the PI controller design values used to generate the reference voltages for the SVPWM switching scheme utilised in the FOC system implemented in this dissertation. Table 3-11 shows the PI controller values, as well as other important parameters of the FOC scheme implemented. The PI controller design values were chosen to enable a fast and stable torque response with low torque, current and flux ripples.

Table 3-11: Parameters used in the implementation of the FOC mechanism

Parameter	Value
d-axis PI Controller	$P = 0.1$
	$I = 5$
q-axis PI Controller	$P = 0.1$
	$I = 100$
Implemented DC supply voltage (10% greater than the minimum)	622 V
SVPWM Switching Frequency	20 kHz
Sampling Frequency	500 kHz

3.6. Field-Weakening Control for DTC Systems

High-speed operation of the traction motor is frequently required due to the application nature of EVs and the speed requirements of highway driving. However, high-speed operation (above the rated speed specification) of an induction motor, when utilising vector control mechanisms, is limited by the maximum current rating of the motor windings as well as the maximum inverter voltage [25], [110]. As a result, the integration of field-weakening control is required to allow the traction motor to operate above the rated speed specification [110], [111]. The inverter current rating and DC link voltage limit the motor torque in the field-weakening region, and as a result, motor torque limits are required to ensure stable operation of the induction motor in the field-weakening region. The authors in [111] provide research in this area with the proposal of a field-weakening method which allows for good dynamic performance and stable operation of the motor across the entire speed range of the drive. Such drive performance is ensured with the implementation of reference torque limits. The proposed method was chosen for use in this study due to its suitability for use in direct torque-controlled EV drive systems. The operation of a traction motor drive across its entire speed range requires three regions to be considered, which are depicted in Figure 2-18 (section 2.8). The pull-out torque of the traction motor, as well as the maximum machine overload torque (which is extended to the field-weakening region), define the torque limits shown in Figure 2-18 [111]. Computation of the stator flux reference value which provides almost optimal stator flux orientation is carried out with the use of the $(1/\omega_r)$ field-weakening method [111], [112]. Due to the implementation of this strategy, the stator flux reference in the DTC algorithm is calculated utilising equation 3-14 [111].

$$|\psi_s^*| = \frac{\psi_{s,rated}\omega_{base}}{|\omega_r|} \; for \; |\omega_r| > \omega_{base} \tag{3-14}$$

In which, $\psi_{s,rated}$ is the rated stator flux, ω_{base} is the base speed of the drive, which can be calculated using equation 3-15, and ω_r is the speed of the rotor [111].

$$\omega_{base} = \frac{V_{s,max}}{\psi_{s,rated}} \tag{3-15}$$

Where, $V_{s,max}$ is the maximum phase voltage that the inverter can supply. The maximum phase voltage which the inverter can supply is determined by the DC link voltage, the PWM switching strategy, dead-time effects of the inverter, and the ON-state voltage drops of the inverter [111]. The torque limits necessary for stable operation of the traction motor drive, which correspond to Figure 2-18, can be calculated utilising equation 3-16 [111].

$$\begin{cases} T_{e,sat} = T_{max}, \ \ if\ |\omega_r| \leq |\omega_{base}| \\ T_{e,sat} = \dfrac{T_{max}\omega_{base}}{|\omega_r|}, if\ \omega_{base} < |\omega_r| \leq \omega_{base1} \\ T_{e,sat} = 3\dfrac{P}{2}\left(\dfrac{1-\sigma}{L_s}\right)\left(\dfrac{\tau_r \omega_{slip_1}\psi_s^2}{1+\left(\sigma\omega_{slip1}\tau_r\right)^2}\right), \\ if\ |\omega_r| > \omega_{base1} \end{cases} \tag{3-16}$$

In which, $T_{e,sat}$ is the torque saturation limit required in each region of operation, T_{max} is the maximum machine overload torque, ω_{base1} is a speed which is based on ω_{po} (the speed at which the maximum machine overload torque and the pull-out torque intersect in the field-weakening region, as shown in Figure 2-18), P is the number of pole pairs in the induction motor, ω_{slip1} is the slip frequency which corresponds to ω_{base1}, σ is the total leakage factor ($\sigma = 1 - L_m^2/L_sL_r$), and τ_r is the rotor time constant ($\tau_r = L_r/R_r$). L_s and L_r are the stator and rotor self-inductances, respectively, and L_m is the magnetising inductance of the induction motor. As a result, various other terms need to be calculated and defined for the torque limits to be calculated. The speed ω_{po} can be calculated using equation 3-17 [111].

$$\omega_{po} = 3\frac{P}{2}\left(\frac{1-\sigma}{2\sigma L_s}\right)\left(\frac{\psi_{s,rated}^2}{T_{max}}\right)\omega_{base} \tag{3-17}$$

A practically employed field-weakening technique should use a boundary speed (ω_{base1}), which is slightly less than ω_{po}. This suggests that the boundary speed utilised should be slightly less than the theoretical boundary speed calculated, limiting the motor torque to slightly less than the pull-out torque of the machine [111]. As a result, for the purpose of this investigation, the boundary speed (ω_{base1}) was chosen to be 95% of the theoretical boundary speed (ω_{po}). The slip frequency, which corresponds to ω_{base1} can be calculated using equation 3-18 [111].

$$\omega_{slip1} = \frac{1-\sqrt{1-(2K\sigma)^2}}{2K\sigma^2\tau_r} \tag{3-18}$$

In which K can be given by equation 3-19.

$$K = \frac{T_{max}L_s}{3\frac{P}{2}(1-\sigma)\left(\frac{\omega_{base}}{\omega_{base1}}\right)\psi_{s,rated}^2} \tag{3-19}$$

The torque limits in the field-weakening region are determined through online calculation and are dependent on the operating conditions of the motor. However, the speed boundaries of each

section of the field-weakening region must be designed using Equations 3-15 and 3-17. The calculated speed boundaries required for field-weakening in this study are shown in Table 3-12. Figure 3-4 shows the motor torque limits and the torque saturation limit calculated to maintain stable traction motor operation

Table 3-12: Speed limits in the field-weakening region

Parameter	Value	Parameter	Value
ω_{base}	3000 rpm	ω_{base1}	8624 rpm
ω_{po}	9075 rpm		

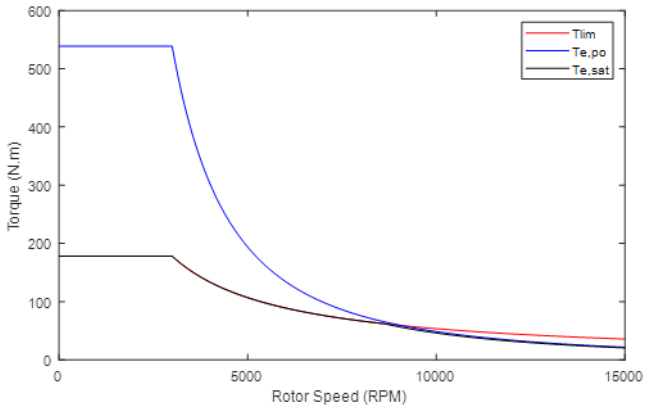

Figure 3-4: Calculated Torque limits for field-weakening operation

3.7. Sensorless Speed Control

As an EV system could be considered a hostile environment, sensorless DTC offers various advantages, which include a reduction in hardware complexity, cost, maintenance, and size of the machine drive, while also allowing for improved noise immunity and increased reliability [115]. Numerous well-developed induction motor speed estimation methods which can be used within a DTC system are available. These methods include open-loop estimators (which use monitored stator voltages and currents), artificial intelligence-based estimators (neural network and fuzzy-logic-based systems) and model reference adaptive systems (MRAS) [116], [117]. An open-loop rotor flux-based estimation technique is convenient for speed estimation in DTC systems, as the parameters of the induction motor are completely known, and the method allows for the instantaneous rotor speed to be estimated with the use of basic induction motor model equations [116], [117]. However, the accuracy of open-loop rotor flux-based speed estimation is highly dependent on the accuracy of the induction motor parameters used [116]. Furthermore, open-loop estimators usually exhibit poorer performance at low rotor speeds, with the steady-state and transient performance of drive systems which utilise open-loop speed estimators greatly impacted by parameter variations [116]. As a result, the performance of both an open-loop rotor flux-based estimation technique and an MRAS mechanism are investigated for induction motor speed estimation in the EV traction motor system discussed in this dissertation.

3.7.1. Open-Loop Rotor Flux-Based Speed Estimation

In all of the previous DTC models investigated in this chapter, only the stator parameters were required; however, for online estimation of the rotor speed using the rotor flux-based estimation technique, the rotor voltages, currents, and fluxes are also required. The rotor currents in the stationary α- and β-axis can be calculated using equations 3-20 and 3-21, respectively [131].

$$i_{\alpha r} = \frac{1}{L_m}\left\{\int (v_{\alpha s} - R_s i_{\alpha s})dt - L_s i_{\alpha s}\right\} \tag{3-20}$$

$$i_{\beta r} = \frac{1}{L_m}\left\{\int (v_{\beta s} - R_s i_{\beta s})dt - L_s i_{\beta s}\right\} \tag{3-21}$$

The α- and β-axis components of the rotor flux can be found from the rotor current components. The rotor flux in the α- and β-axes are given by equations 3-22 and 3-23, respectively [117], [131].

$$\psi_{\alpha r} = L_r i_{\alpha r} + L_m i_{\alpha s} \tag{3-22}$$

$$\psi_{\beta r} = L_r i_{\beta r} + L_m i_{\beta s} \tag{3-23}$$

As a result, the rotor flux magnitude can be found using equation 3-24 [131].

$$|\psi_r| = \sqrt{\psi_{\alpha r}^2 + \psi_{\beta r}^2} \tag{3-24}$$

Accurate estimation of the flux components is essential, as it directly impacts the accuracy of the speed estimation system [116]. The estimation technique chosen has been utilised in commercially available and industrial DTC induction motor drives [116]. The online rotor flux-based speed estimation system calculates the instantaneous rotor speed through the use of equation 3-25 [116].

$$\omega_r = \omega_{mr} - \omega_{sl} \tag{3-25}$$

Where ω_{mr} is the speed of the rotor flux relative to the stator, and ω_{sl} is the angular slip frequency. The speed of the rotor flux and the angular slip frequency can be found using equations 3-26 and 3-27, respectively [116], [117].

$$\omega_{mr} = \frac{\psi_{\alpha r}\frac{d\psi_{\beta r}}{dt} - \psi_{\beta r}\frac{d\psi_{\alpha r}}{dt}}{|\psi_r|^2} \tag{3-26}$$

$$\omega_{sl} = \frac{2T_e R_r}{3P|\psi_r|^2} \tag{3-27}$$

Where P is the number of pole pairs, and R_r is the rotor resistance. As a result, using equations 3-20 – 3-27, the instantaneous rotor speed can be estimated using equation 3-28 [116], [117].

$$\omega_r = \frac{\psi_{\alpha r}\frac{d\psi_{\beta r}}{dt} - \psi_{\beta r}\frac{d\psi_{\alpha r}}{dt}}{|\psi_r|^2} - \frac{2T_e R_r}{3P|\psi_r|^2} \tag{3-28}$$

All equivalent circuit parameters of the motor used in the online speed estimation system are given in Appendix A, Table A-2. All calculations required for the estimation of the instantaneous

rotor speed must be performed during the operation of the system. As a result, the calculations are required to be implemented in an estimator model.

3.7.2. MRAS-Based Speed Estimation

Closed-loop speed estimation mechanisms allow for increased accuracy when compared with open-loop mechanisms, and as a result, a rotor flux-based MRAS system is investigated. The general structure of an MRAS speed estimation mechanism is shown in Figure 3-5, in which both a reference and adaptive model are required. The state variables in the reference (x_α and x_β) and adaptive ($\hat{x}_\alpha$ and $\hat{x}_\beta$) models are compared, with the difference between the values (ε_α and ε_β) used in an adaption mechanism. An estimation of the rotor speed ($\hat{\omega}_r$) value is obtained at the output of the adaption mechanism and is used to adjust the adaptive model until an accurate estimation of the rotor speed is obtained [116]. The reference model utilises measured quantities (commonly the stator voltages and currents, as shown in Figure 3-5) in order to estimate the state variables [116].

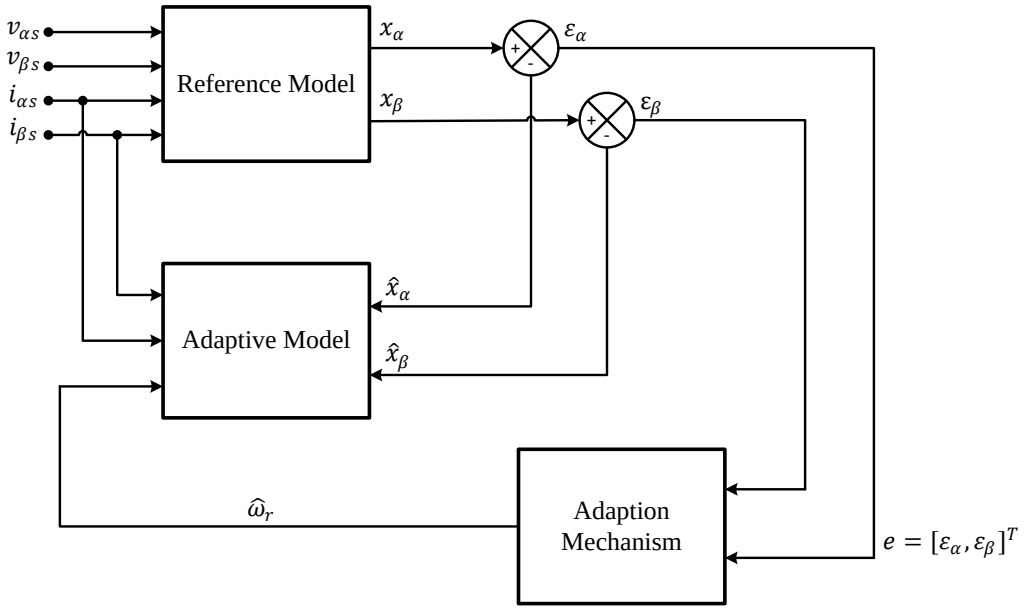

Figure 3-5: General structure of an MRAS speed estimation system [116]

Popov's hyperstability criterion can be used to derive an appropriate adaption mechanism, which allows for a system with a fast and stable response. The adaption mechanism usually consists of a PI-type controller, which uses the state variable error as an input [116]. The suitability of a PI-type controller for the adaption mechanism is described by Popov's criterion for hyperstability, with Popov's theorem also indicating the form of the speed tuning signal (ε) required [116]. Although a proof is not provided in this chapter, Popov's criterion for hyperstability can be used to indicate that estimation of the rotor flux components in the stator reference frame, estimated in the reference and adaptive models of an MRAS, can be used to successfully estimate the rotor speed at the output of the adaption mechanism [116].

Estimation of the rotor flux-linage components (stationary reference frame) in the reference model is carried out using the 'stator voltage model', which makes use of the stator voltage equations of the induction motor. The resulting rotor flux in the stationary α-β reference is found using equations 3-29 and 3-30 [116].

$$\psi_{\alpha r} = \frac{L_r}{L_m}\left[\int (v_{\alpha s} - R_s i_{\alpha s})dt - L'_s i_{\alpha s}\right] \tag{3-29}$$

$$\psi_{\beta r} = \frac{L_r}{L_m}\left[\int (v_{\beta s} - R_s i_{\beta s})dt - L'_s i_{\beta s}\right] \tag{3-30}$$

In which, L'_s represents the stator transient inductance, with all of the other parameters previously defined. While the stator voltage equations in the stationary α-β reference frame can be used for estimation of the rotor flux components without the inclusion of a rotor speed component, expression of the rotor flux components using rotor voltage equations leads to a set of equations in which the rotor speed is included [116]. As a result, such a set of equations is suitable for use in the adaptive model and is shown in equations 3-31 and 3-32 [116].

$$\hat{\psi}_{\alpha r} = \frac{1}{\tau_r}\int \left(L_m i_{\alpha s} - \hat{\psi}_{\alpha r} - \omega_r \tau_r \hat{\psi}_{\beta r}\right)dt \tag{3-31}$$

$$\hat{\psi}_{\beta r} = \frac{1}{\tau_r}\int \left(L_m i_{\beta s} - \hat{\psi}_{\beta r} + \omega_r \tau_r \hat{\psi}_{\alpha r}\right)dt \tag{3-32}$$

The speed tuning signal, which is used as the input to the adaption mechanism, is calculated by finding the angular difference of the outputs of the reference and adaptive models. As a result, the speed tuning signal can be calculated using equation 3-33 [116].

$$\varepsilon = Im\left(\bar{\psi}'_r \hat{\bar{\psi}}'^{*}_r\right) = \psi_{\beta r}\hat{\psi}_{\alpha r} - \psi_{\alpha r}\hat{\psi}_{\beta r} \tag{3-33}$$

The use of a PI controller and the speed tuning signal in equation 3-33 provides a stable nonlinear feedback system. The estimated rotor speed value is tuned by the PI controller when there is a non-zero error between the rotor flux estimates in the reference and adaptive models ($\bar{\psi}'_r \neq \hat{\bar{\psi}}'_r$) [116]. Therefore, when the difference between the output of the reference and adaptive models is zero, the estimated rotor speed is equivalent to the actual rotor speed [116]. As a result, the estimated speed can be expressed using equation 3-34 [116].

$$\hat{\omega}_r = K_p \varepsilon + K_i \int \varepsilon dt \tag{3-34}$$

The application of pure integrators required in the rotor flux MRAS mechanism described above makes practical implementation of the reference model challenging due to initial value and drift issues. As a result, the use of a low-pass filter is preferred in place of the pure integrator in practical systems [116]. Consequently, the MRAS mechanism investigated in this dissertation makes use of low-pass filters, mitigating the need for pure estimators in the reference model of the speed estimation system. The resulting set of equations for rotor flux estimation in the reference model is provided in equations 3-35 and 3-36 [116].

$$\left(p+\frac{1}{T}\right)\psi'_{\alpha r}=\frac{L_r}{L_m}\left(v_{\alpha s}-R_s i_{\alpha s}-L'_s p i_{\alpha s}\right) \tag{3-35}$$

$$\left(p+\frac{1}{T}\right)\psi'_{\beta r}=\frac{L_r}{L_m}\left(v_{\beta s}-R_s i_{\beta s}-L'_s p i_{\beta s}\right) \tag{3-36}$$

As equations 3-35 and 3-36 indicate modified rotor flux components at the output of the reference model, a high-pass filter is required before the inputs to the adaptive model to ensure corresponding values are estimated in the adaptive model. Resultantly, the final form of the rotor flux-based MRAS system implemented in this dissertation is shown in Figure 3-6.

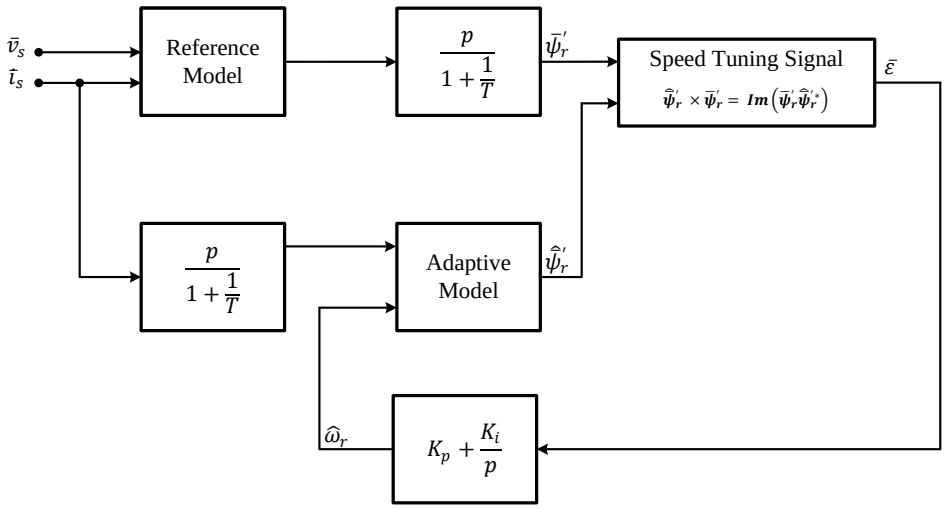

Figure 3-6: Structure of the implemented closed-loop rotor flux-based MRAS [116]

The authors in [116] suggest that the cut-off frequency of the high-pass filter is a few Hertz in practice, and as a result, rotor speed estimation at very low speeds becomes inaccurate. This can be problematic in cases where the drive is operated at zero frequency for longer than a few seconds and is a disadvantage of the rotor flux-based MRAS described [116].

3.8. Conclusion

The selection of a motor for an EV system is a significant part of the system design, as the motor must be chosen to ensure that the intensive performance requirements of the EV system can be met. As a result, this chapter, which aims to present the methodology used for the research work carried out, includes an investigation of motor selection based on theoretical parameters and is extended to motor sizing through parameter matching calculations. The selection of an induction motor requires the use of field-oriented control or direct torque control schemes. Through a theoretical and technical discussion of various aspects of an EV traction motor control system, the methodology for the implementation of various suitable control models was realised. The performance of the control models discussed is assessed in a simulation-based study, which is presented in the chapters that follow.

4. Chapter 4 – Initial Comparison of Traction Motor Control Systems (Simulation Results)

4.1. Introduction

Theoretically, both DTC and FOC mechanisms provide convenient solutions for control of the traction motor drive in EV applications. Chapter 3 discussed the methodology behind the implementation of conventional DTC and FOC mechanisms, as well as various improvements to CDTC (DTC-SVM-TC, DTC-SVM-FTC and fuzzy DTC). This chapter aims to provide an initial simulation-based assessment of the suitability of each of these techniques for use in the traction motor control mechanism of an EV. The techniques are assessed using a simple drive cycle and are compared based mainly on the torque, current and flux ripples, as well as the THD of the current waveform observed from each system. The simulations carried out in this chapter contain only the standard structure of the control mechanism and do include field-weakening or sensorless control functionality. However, the most applicable control techniques are extended and simulated with more advanced control structures, with the results provided in later chapters of this dissertation.

4.2. Conventional Direct Torque Control Results

As mentioned in the methodology, a 500 kHz sampling frequency was utilised in the study of CDTC in this dissertation, as the sampling frequency has a major impact on the torque, flux and current ripples observed. The sampling frequency is consistent in all motor control systems investigated in this chapter, allowing for an accurate comparison of the techniques. Figure 4-1 shows the induction motor speed response in comparison to the reference or desired speed. Ramp speed inputs were utilised during the simulation due to the nature of acceleration in vehicle systems. The figure shows that the motor drive system responds well to acceleration and deceleration, with very little noticeable overshoot or undershoot.

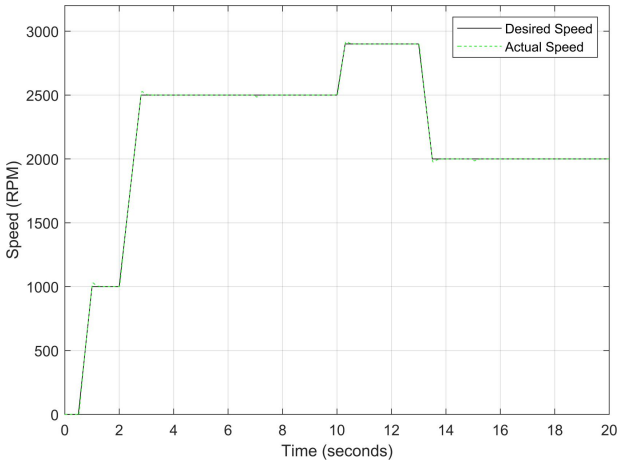

Figure 4-1: CDTC – Induction motor speed

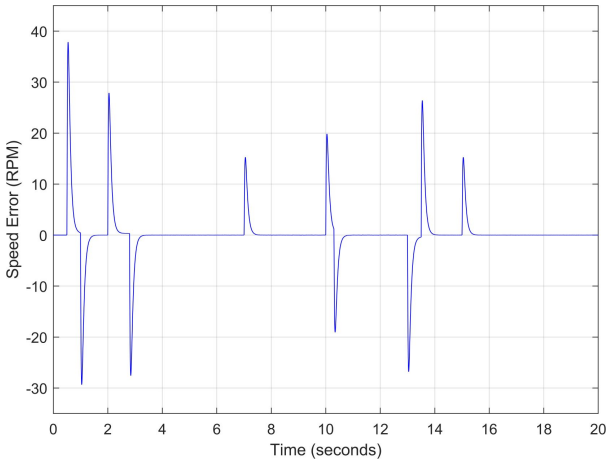

Figure 4-2: CDTC – Induction motor speed error

However, the maximum speed at which the motor was driven was 2900 rpm. The rated speed of the induction motor utilised is 2952 rpm, which was not exceeded as field-weakening control was not implemented in the CDTC mechanism. As mentioned previously, the implementation of field-weakening control is required to operate the motor above its rated speed specification and is therefore required in order to operate the motor at the maximum required speed of 8046 rpm. Figure 4-2 shows the induction motor speed error when compared to the desired or reference speed, utilising the drive cycle shown in Figure 4-1. The speed error graph indicates that desirable results were achieved as an overshoot/undershoot of less than 3% was obtained in all speed changes in the drive cycle. In addition, there is no steady-state error. The implemented mechanism allows for a fast response, minimal overshoot, and no noticeable steady-state error.

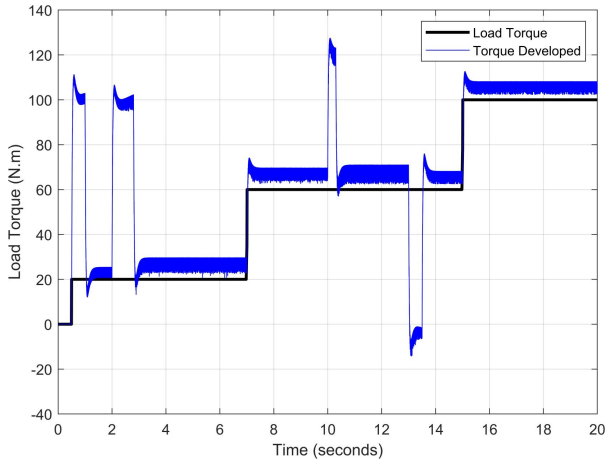

Figure 4-3: CDTC – Torque developed by induction motor (500 kHz)

The torque ripple is an important metric in the performance of the traction motor drive system, as the rideability and comfort of the EV system are degraded as a result of high torque ripple. The developed torque that the induction motor supplied to the load in comparison to the load torque is shown in Figure 4-3. Several notable results can be highlighted from the developed torque. Initially, when accelerating, the motor must supply a greater torque than is required by the load in order to allow for the desired speed to be achieved. Figure 4-3 indicates that this is the case

during all periods in which the motor is accelerating. Additionally, when decelerating, the developed torque is lower than the load torque. The DTC model implemented provides fast torque response with very little overshoot, a major benefit in the use of DTC schemes. The torque developed responds well to step inputs in the load torque, with no noticeable delay in the response. The favourable dynamic torque response observed from the CDTC scheme is advantageous for vehicular systems.

However, one of the issues that can be noticed in Figure 4-3 is the large torque ripple, which is especially apparent when the motor is operated at higher speeds. When the motor is operating at 2900 rpm, a torque ripple of approximately 8.75 N.m can be observed. The torque ripple is directly proportional to the width of the torque controller hysteresis band. However, there is a delay between the sampling of the values and the changing of the appropriate switching states in digital implementation. As a result, the torque ripple is dependent on the hysteresis controller as well as the sampling frequency of the digital controller. Reducing the torque controller hysteresis band width too much can increase the torque ripple, as incidents of overshoot in the estimated torque, that are above the hysteresis band, can cause the reverse voltage vector to be selected, resulting in sharp decreases in torque. The torque graph shown in Figure 4-3 was generated with a simulation sampling frequency of 500 kHz. Figure 4-4 shows the torque developed by the induction motor with a sampling frequency of 200 kHz. It can be observed that the developed torque ripple is noticeably higher than when a sampling frequency of 500 kHz was used. The result indicates the strong dependence of the DTC mechanism on the processor speed.

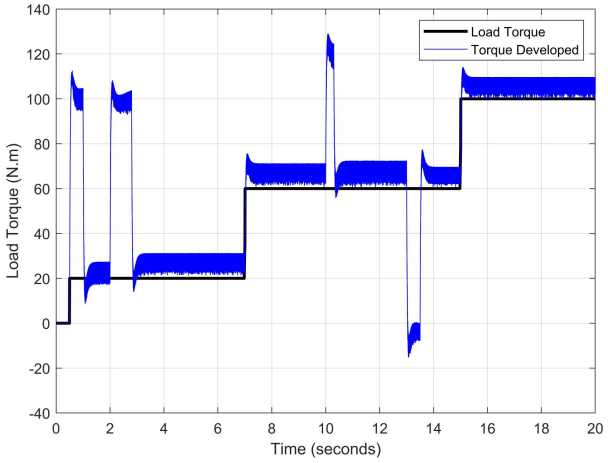

Figure 4-4: CDTC – Torque developed by induction motor (200 kHz)

Another issue which can be noticed with the CDTC scheme implemented is the presence of steady-state torque error. Furthermore, the steady-state torque error is higher with operation at higher speeds, and is a result of the torque being controlled from the speed error. The speed PI controller provides a torque reference which is required to maintain the desired speed, and as a result, higher torque is required in certain operating conditions. The steady-state torque error

results from the friction component in the induction motor utilised in the mechanism and reduces with the reduction of this component or in smaller traction motors.

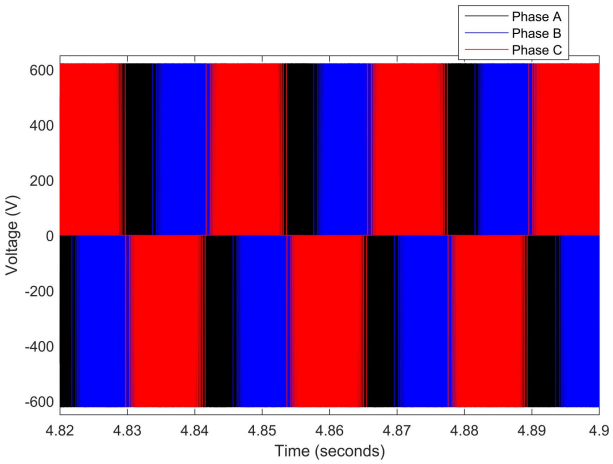

Figure 4-5: CDTC – Three-phase inverter voltage

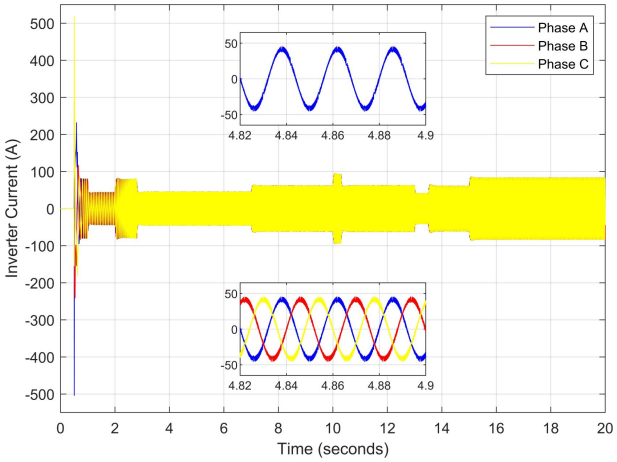

Figure 4-6: CDTC – Three-phase inverter current

The steady-state voltage generated from the two-level three-phase inverter supplying the induction motor is shown in Figure 4-5. The voltage shown was measured during steady-state conditions while the motor was operating at 2500 rpm with a load torque of 20 N.m. All three phases are shown, indicating the phase relationship of the voltages. One of the issues found in CDTC is a variable inverter switching frequency, as the torque and flux slopes vary with operating conditions, which affects the switching controlled by the hysteresis controllers.

Figure 4-6 shows the inverter current supplied to the induction motor during the entire drive cycle. In addition, zoomed-in portions of both the Phase A and the three-phase steady-state inverter current supplied to the induction motor, when the motor was operating at 2500 rpm with a load torque of 20 N.m, are shown. The inverter current is sinusoidal; however, there is a high current ripple (harmonic content). The high current ripple is one of the disadvantages of conventional direct torque control, as previously mentioned in the theoretical review of CDTC. The three-phase inverter current shown presents an expected result, as the currents in each of the three phases are

separated by 120 degrees, as expected in a three-phase system. Notably, the current has a peak amplitude of approximately 50 A when the load torque is 20 N.m. However, Figure 4-6 shows the change in the current when the load torque which the motor is supplying is increased. From 15 to 20 seconds, the induction motor was operating at 2000 rpm with a load torque of 100 N.m. The result clearly indicates the relationship between the current drawn by the motor and the load torque.

In addition to the current ripple in the waveform, the harmonic distortion found using fast Fourier transform (FFT) analysis also provides a useful metric for assessing the quality of the current waveform. Figure 4-7 shows the result of FFT analysis on the current waveform, and was measured during steady-state conditions, while the motor was operating at 2500 rpm (fundamental frequency of ~41.67 Hz) with a load torque of 20 N.m. Furthermore, the analysis was done over ten cycles, allowing for a resolution of ~4.17 Hz. The total harmonic distortion (THD) calculated during this period is 7.43%. Additionally, 5^{th}, 7^{th} and 11^{th} harmonic components are noticeable, with magnitudes of ~0.5-0.7% of the fundamental component. While the current waveform is sinusoidal, it is expected that both the current ripple content and THD will improve when utilising improved motor control techniques.

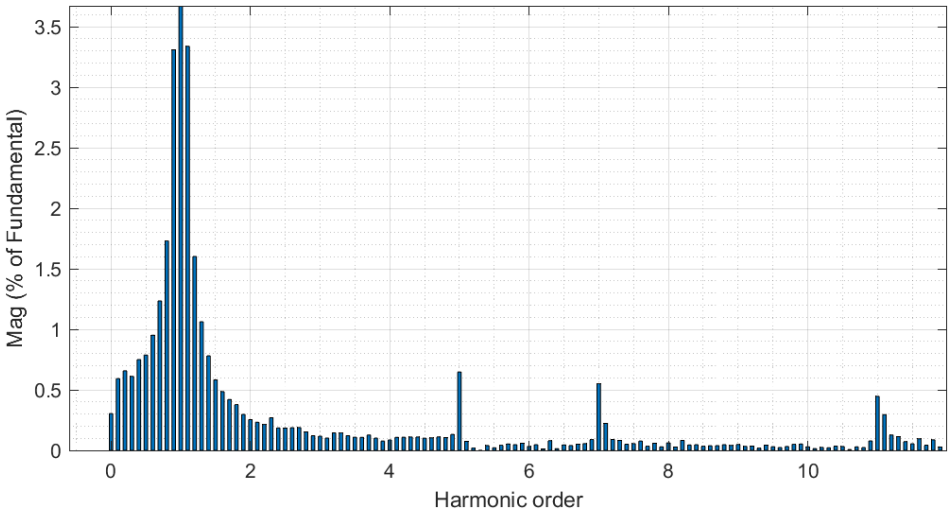

Figure 4-7: CDTC – FFT analysis of the current waveform (phase A)

Figure 4-8 shows the q- and d-axis components of the stator flux. Notably, the flux in both the q- and d-axes have an amplitude of approximately 1.04 Wb, as controlled by the stator flux magnitude reference. The reference stator flux magnitude was kept constant at 1.04 Wb throughout the simulation, and as a result, Figure 4-8 shows an expected result. Although Figure 4-8 confirms that the stator flux in the q- and d-axes have the correct magnitude, a more notable result can be seen by plotting the flux values on the d-q axis. The plot results in the stator flux trajectory being generated, which is shown in Figure 4-9.

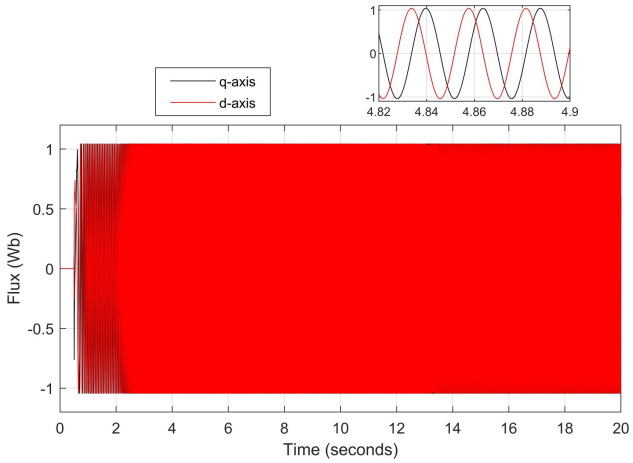

Figure 4-8: CDTC – Stator flux (d- and q- axis)

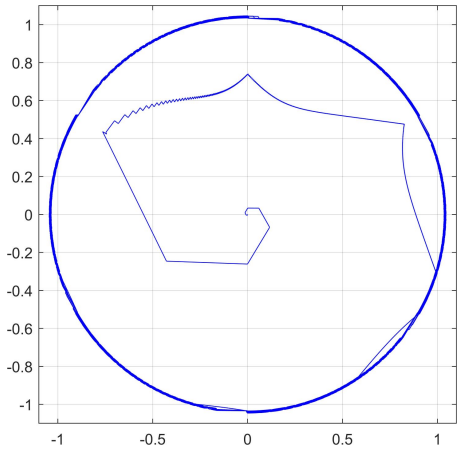

Figure 4-9: CDTC – Stator flux trajectory

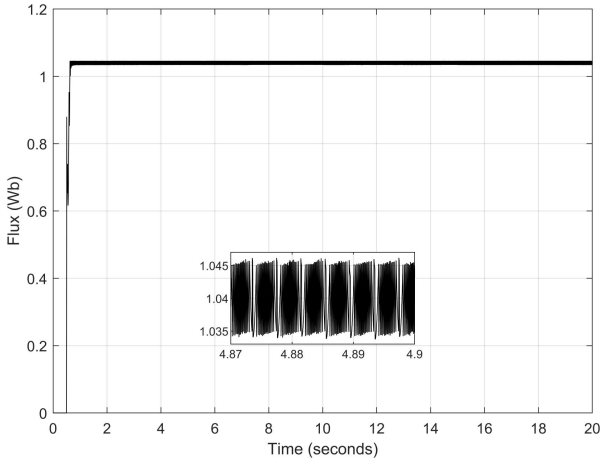

Figure 4-10: CDTC – Stator flux magnitude

The stator flux trajectory shown is equivalent to the theoretical stator flux trajectory of conventional DTC, shown in Figure 2-5. The result shows that the flux initially starts outside of the hysteresis band circles, which occurs at start-up. However, after a few switching sequences, the flux vector follows the circular flux trajectory. The result achieved is desirable, as the stator flux (excluding the initial switching sequences) follows a circular flux trajectory and remains inside the hysteresis band. Such a result indicates that the correct DC voltage has been supplied

to the inverter in order to enable circular flux trajectory DTC. In addition, it also indicates that the flux hysteresis controller is operating expectedly. The stator flux is forced between the hysteresis band as the stator flux increments are correctly selected. This can be further confirmed by the stator flux magnitude plot shown in Figure 4-10. The flux magnitude remains constant throughout the 20-second drive cycle, with the ripple maintained between approximately 1.035 and 1.045 Wb. This can be seen more clearly in the zoomed-in portion of the plot, indicating the ripple when the motor was operating in steady-state conditions, with a speed of 2500 rpm and a load torque of 20 N.m.

The DTC control mechanism implemented produces expected results for conventional DTC, implemented with the use of hysteresis controllers. The speed response obtained is a favourable result, as the reference speed is tracked with little overshoot and no steady-state error. In addition, the developed torque of the motor responds quickly to changes in the load torque with minimal overshoot. The stator flux trajectory observed perfectly matches the theoretical result expected. The stator flux vector rotates in a circular manner, contained within the hysteresis band controller limits. However, despite some of the favourable results obtained, issues such as high torque ripple, high current ripple, a high total harmonic distortion, and variable switching frequency were observed. In addition, it was observed that a high-speed processor is required for adequate implementation of conventional DTC in EV applications. The issues observed are undesirable for implementation in EV systems.

4.3. DTC-SVM-TC – Results

The induction motor speed response in comparison to the reference or desired speed, as well as the induction motor speed error, are shown in Figure 4-11 and Figure 4-12, respectively.

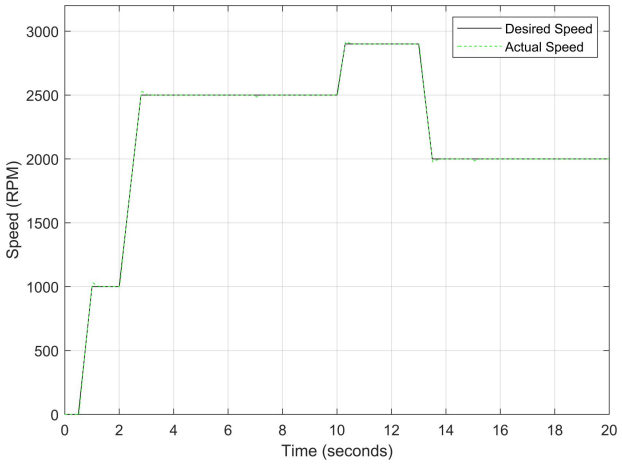

Figure 4-11: DTC-SVM-TC – Induction motor speed

CDTC provided favourable speed control results, and the DTC-SVM-TC mechanism provides equivalent results. The system provides a speed response with negligible steady-state error and

less than 3% overshoot/undershoot in cases where dynamic speed response is required during the drive cycle. However, the use of a torque PI controller and an SVM inverter switching scheme in place of hysteresis controllers and a switching look-up table provides advantageous results when reviewing the developed torque response of the induction motor shown in Figure 4-13. It is useful to note that an SVM frequency of 20 kHz was utilised, as is indicated in Table 3-8. The torque ripple is decreased in almost all sections of the drive cycle compared to CDTC, with the only increase noticed when the motor is operating at 1000 rpm with a load torque of 20 N.m.

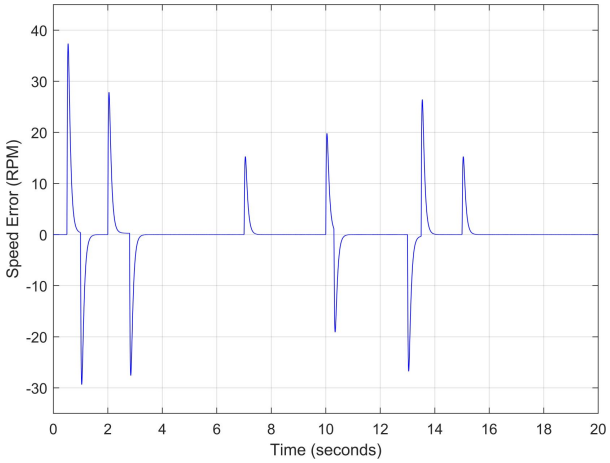

Figure 4-12: DTC-SVM-TC – Induction motor speed error

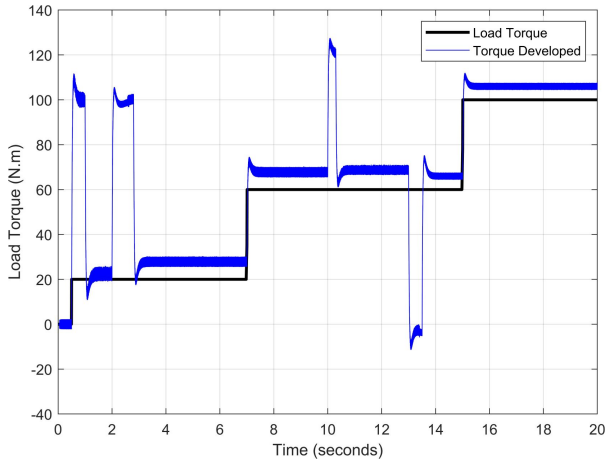

Figure 4-13: DTC-SVM-TC – Torque developed by induction motor (500 kHz)

Furthermore, the DTC-SVM-TC mechanism responds well to step inputs in the load torque, maintaining a fast dynamic torque response with very little overshoot/undershoot during all sections of the drive cycle. A more in-depth comparison of CDTC and DTC-SVM-TC is provided in Table 4-1 (found in section 4.7) and indicates that DTC-SVM-TC significantly assists in the reduction of unwanted torque ripple observed in CDTC. Steady-state torque error can also be noticed from the torque developed when utilising the DTC-SVM-TC mechanism. Although the issue was also present in the CDTC mechanism implemented, the smaller torque ripple present in DTC-SVM-TC makes the issue more apparent. As the steady-state torque error results from the

characteristics of the traction motor used in the system, the error is present in all motor control mechanisms investigated in this chapter.

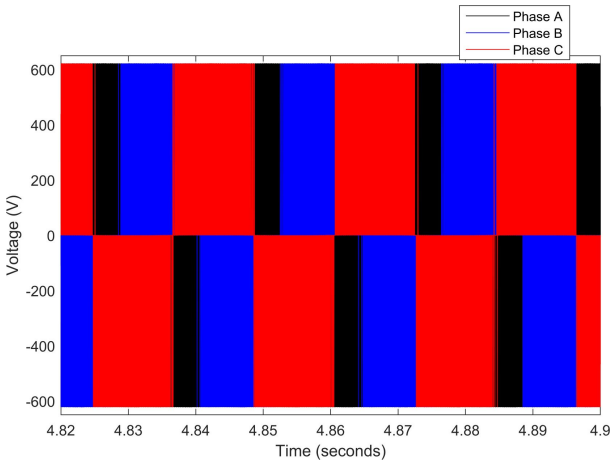

Figure 4-14: DTC-SVM-TC – Three-phase inverter voltage

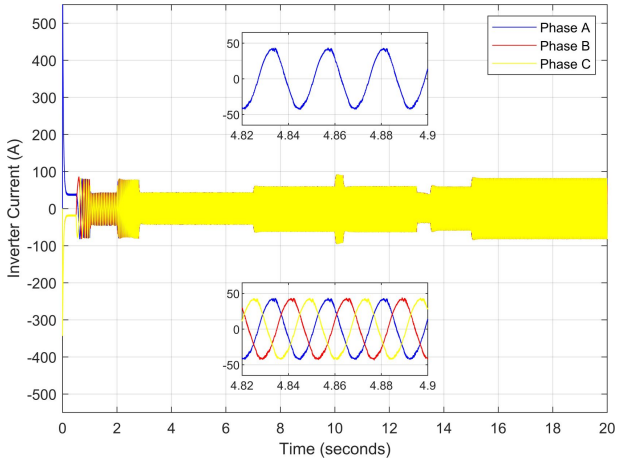

Figure 4-15: DTC-SVM-TC – Three-phase inverter current

Figure 4-14 shows the steady-state voltage generated from the two-level three-phase inverter supplying the induction motor while operating at 2500 rpm with a load torque of 20 N.m. As with the CDTC mechanism, an expected three-phase voltage waveform is generated. However, the current ripple and distortion resulting from sector changes and a variable switching frequency present in the CDTC mechanism are reduced with the use of DTC-SVM-TC. The improved current waveform and current distortion (found using FFT analysis) are shown in Figure 4-15 and Figure 4-16, respectively. Zoomed-in portions of both the phase A and three-phase steady-state current, measured when the motor was operating at 2500 rpm with a load torque of 20 N.m, are shown in Figure 4-15. The zoomed-in portions of the current waveform allow for the improved current ripple and harmonic distortion to be easily noticed. Although Figure 4-16 indicates an improved THD (measured to be 6.41%) when compared to CDTC, with reduced 5^{th}, 7^{th} and 11^{th} harmonic components, much higher 2^{nd}, 4^{th}, 8^{th}, and 10^{th} harmonic components are noticeable. A more in-depth comparison of the quality of the current waveforms observed from the motor control techniques investigated in this chapter is provided in Table 4-2 (found in section 4.7).

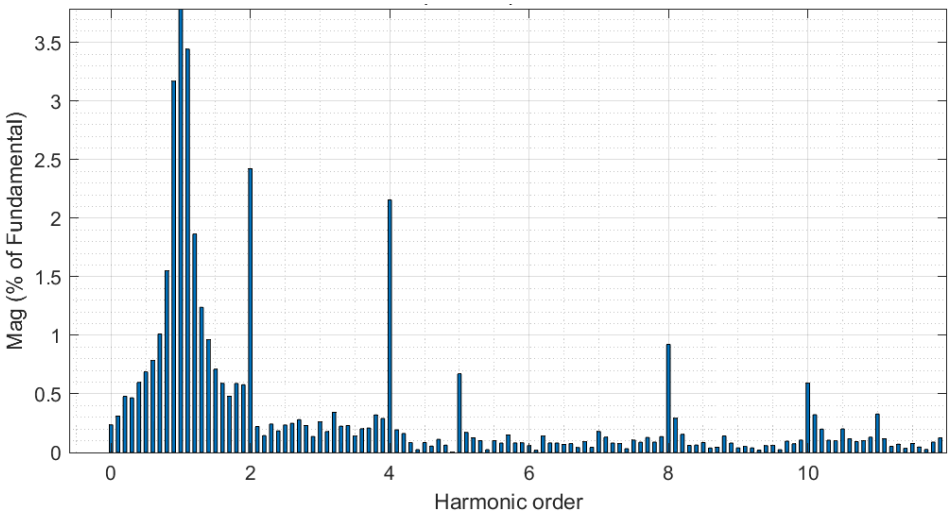

Figure 4-16: DTC-SVM-TC – FFT analysis of the current waveform (phase A)

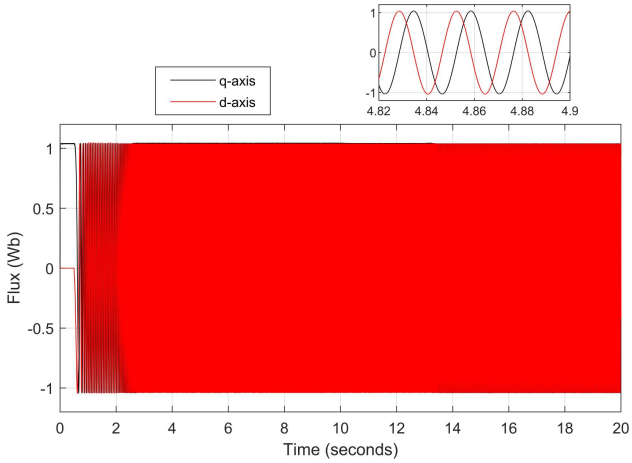

Figure 4-17: DTC-SVM-TC – Stator flux (d- and q-axis)

Figure 4-17 shows the q- and d-axis components of the stator flux. Notably, the flux in both the q- and d-axes have an amplitude of approximately 1.04 Wb, as controlled by the stator flux magnitude reference. However, one of the main characteristics of the DTC-SVM-TC mechanism is that the stator flux is controlled in an open-loop manner. The disadvantages associated with open-loop control of the stator flux can be observed mostly in the circular stator flux trajectory and stator flux magnitude results of the DTC-SVM system, shown in Figure 4-18 and Figure 4-19, respectively. Although a smooth circular stator flux trajectory is obtained in DTC-SVM-TC, Figure 4-19 indicates that the stator flux ripple is not constant throughout the drive cycle utilised. Furthermore, in certain operating conditions, the stator flux ripple obtained from the DTC-SVM-TC mechanism is larger than that observed from the CDTC mechanism. An example of this is when the motor was operating with a speed of 2500 rpm and a load torque of 20 N.m (shown in the zoomed-in portion of Figure 4-19), during which the stator current ripple was measured to be 14.8 mWb. However, a constant stator flux magnitude of 1.04 Wb is maintained throughout the drive cycle simulated. A comparison of the stator flux performance in the motor control techniques investigated in this chapter is provided in Table 4-2 (found in section 4.7).

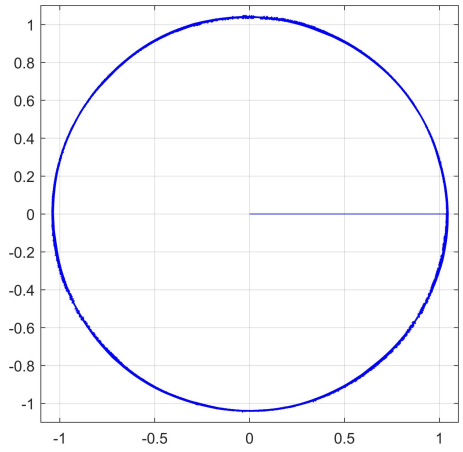

Figure 4-18: DTC-SVM-TC – Stator flux trajectory

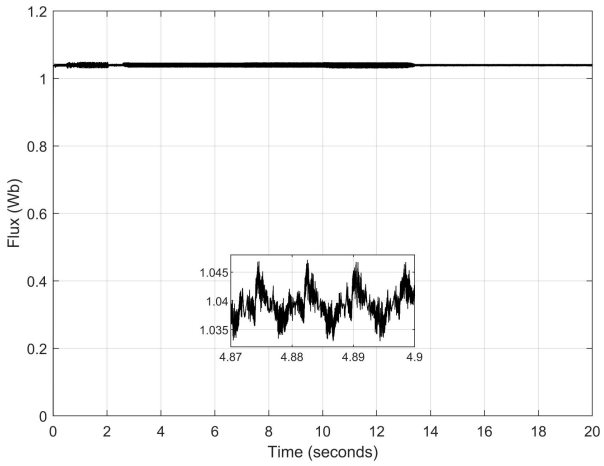

Figure 4-19: DTC-SVM-TC – Stator flux magnitude

The implementation of DTC-SVM using closed-loop torque control presents significant advantages when compared to the CDTC system investigated. Reductions in torque ripple, current ripple, and THD of the current waveform are noticed, with the method also enabling a constant switching frequency. As a result, the DTC-SVM-TC technique presented significantly improves the CDTC structure initially simulated and is more applicable for implementation in EV systems. However, the mechanism presents some disadvantages due to the open-loop flux control present. Such disadvantages can be mitigated with the use of a DTC-SVM-FTC scheme, and consequently, the DTC-SVM-FTC mechanism is investigated in the next section of this chapter.

4.4. DTC-SVM-FTC – Results

The DTC-SVM-FTC mechanism, utilising a sampling frequency of 500 kHz and an SVM frequency of 20 kHz, provides an equivalent speed response to that obtained from the DTC-SVM-TC mechanism. The induction motor speed response in comparison to the reference or desired speed and the induction motor speed error are shown in Figure 4-20 and Figure 4-21, respectively. Again, favourable steady-state and dynamic speed performance is obtained from the DTC system, with no noticeable difference between the mechanisms investigated thus far. The DTC-SVM-

FTC mechanism structure is adjusted slightly when compared to the DTC-SVM-TC mechanism, containing a torque and flux PI controller and resulting in closed-loop control of both the developed torque and stator flux.

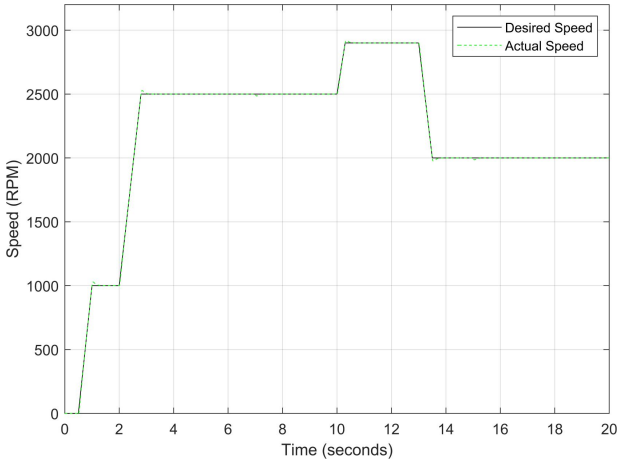

Figure 4-20: DTC-SVM-FTC – Induction motor speed

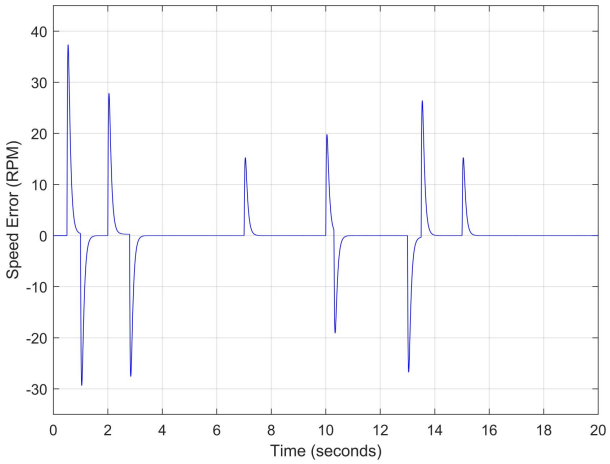

Figure 4-21: DTC-SVM-FTC – Induction motor speed error

Although the addition of a flux PI controller to the system does not impact the speed response of the system, improvements can be observed in the developed torque, inverter current waveform and the stator flux of the induction motor. The developed torque supplied to the load in comparison to the load torque is shown in Figure 4-22. The developed torque generated by the traction motor, controlled through the use of the DTC-SVM-FTC mechanism, exhibits a fast dynamic torque response, with a largely constant torque ripple throughout the drive cycle. This is a notable result, as in both CDTC and DTC-SVM-TC, the torque ripple varied considerably with the operating conditions of the motor. Furthermore, the DTC-SVM-FTC mechanism shows reduced torque ripple in a large portion of the drive cycle when compared with DTC-SVM-TC, with the highest torque ripple observed being 3.45 N.m, when the motor was operating at 2000 rpm with a load torque of 100 N.m. DTC-SVM-FTC maintains a fast and stable torque response when subjected to step inputs in the load torque while enabling further reduction of unwanted torque ripple in the system. However, as is expected, the steady-state torque error present in both

of the previous DTC mechanisms can still be observed. An in-depth analysis of the torque ripple obtained from the DTC-SVM-FTC control scheme is provided in Table 4-1 (found in section 4.7).

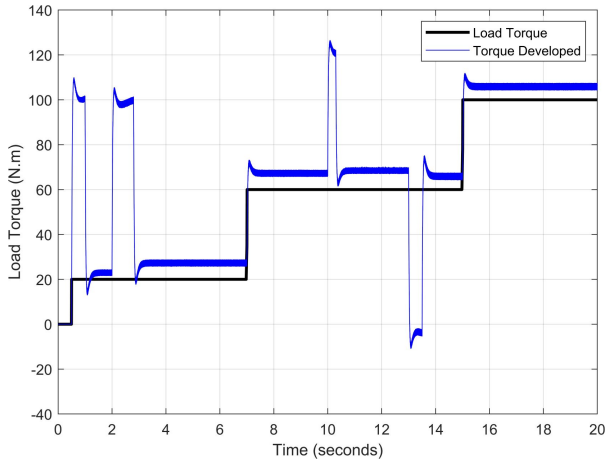

Figure 4-22: DTC-SVM-FTC – Torque developed by induction motor (500 kHz)

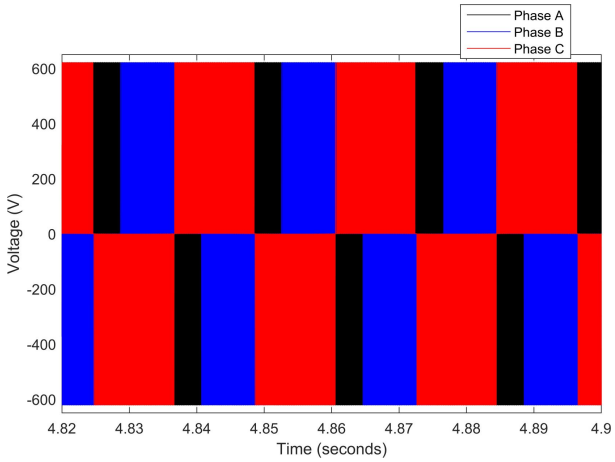

Figure 4-23: DTC-SVM-FTC – Three-phase inverter voltage

The steady-state voltage generated from the two-level three-phase inverter supplying the induction motor while operating at 2500 rpm with a load torque of 20 N.m is shown in Figure 4-23. An expected three-phase voltage is obtained, with the result equivalent to that seen from the DTC-SVM-TC scheme. However, the current waveform generated with the use of DTC-SVM-FTC, shown in Figure 4-24, shows notable improvement when compared to the current waveform generated using DTC-SVM-TC. Zoomed-in portions of both the Phase A and the three-phase steady-state inverter current supplied to the induction motor, when the motor was operating at 2500 rpm with a load torque of 20 N.m, are shown, and indicate reduced current ripple and improved current distortion. Furthermore, the harmonic distortion of the current waveform, found using FFT analysis, is also improved (with the THD measured to be 4.91%), as shown in Figure 4-25. The FFT analysis was performed over ten cycles of the current waveform while the motor was operating at 2500 rpm (fundamental frequency of ~41.67 Hz) with a load torque of 20 N.m. Although noticeable 5^{th} and 7^{th} harmonic components are present, the harmonic distortion analysis indicates the quality of the current waveform is improved when compared to both CDTC and

DTC-SVM-TC. The quality of the current waveform generated with the DTC-SVM-FTC scheme is also assessed in Table 4-2 (found in section 4.7).

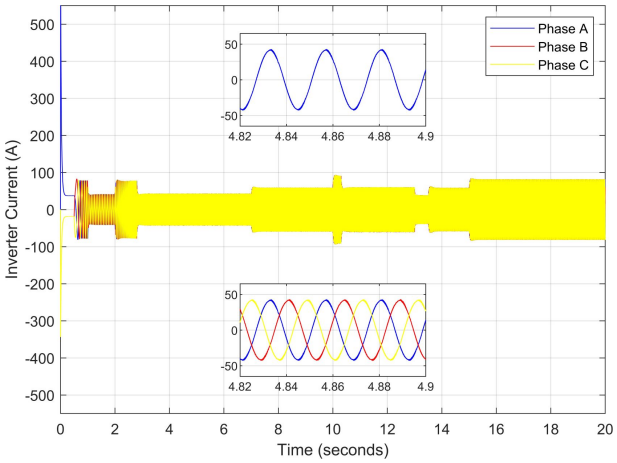

Figure 4-24: DTC-SVM-FTC – Three-phase inverter current

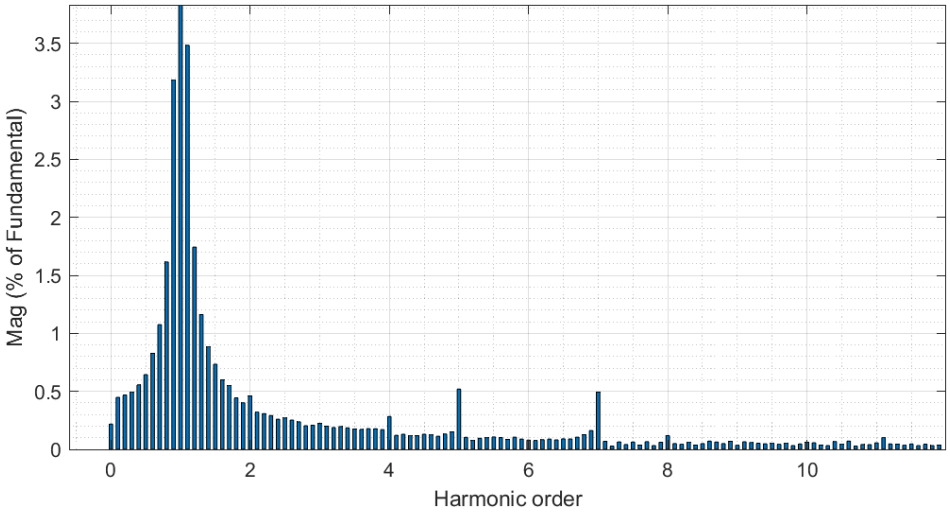

Figure 4-25: DTC-SVM-FTC – FFT analysis of the current waveform (phase A)

Figure 4-26 shows the q- and d-axis components of the stator flux. Notably, the flux in both the q- and d-axes have an amplitude of approximately 1.04 Wb, as controlled by the stator flux magnitude reference, which was maintained constant at 1.04 Wb throughout the drive cycle simulated. Interestingly, while the DTC-SVM-FTC scheme again produces a smooth circular stator flux trajectory, as shown in Figure 4-27, it can be observed that the circular flux band width is narrower than seen in both the CDTC and DTC-SVM-TC schemes. This result indicates a reduced flux ripple and is confirmed by the flux magnitude result shown in Figure 4-28. The zoomed-in portion of the plot in Figure 4-28 indicates the ripple when the motor was operating in steady-state conditions, with a speed of 2500 rpm and a load torque of 20 N.m. The ripple during this period was found to be 6 mWb, which is a significant reduction compared to the previously investigated control schemes. Such a large improvement in the stator flux ripple can be attributed to the use of closed-loop flux control while also utilising a system in which hysteresis control and

a switching look-up table are not present. The stator flux performance of the DTC-SVM-FTC control scheme is also assessed in Table 4-2 (found in section 4.7).

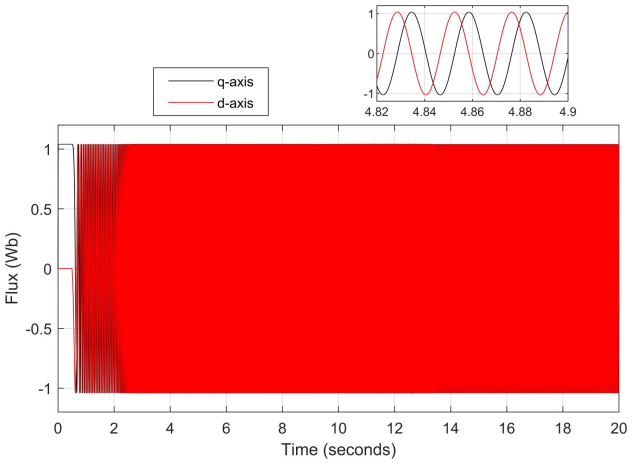

Figure 4-26: DTC-SVM-FTC – Stator flux (d- and q-axis)

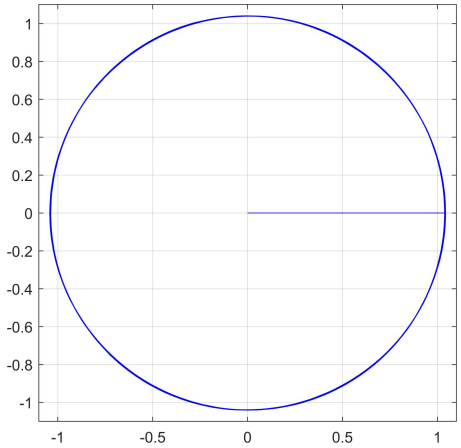

Figure 4-27: DTC-SVM-FTC – Stator flux trajectory

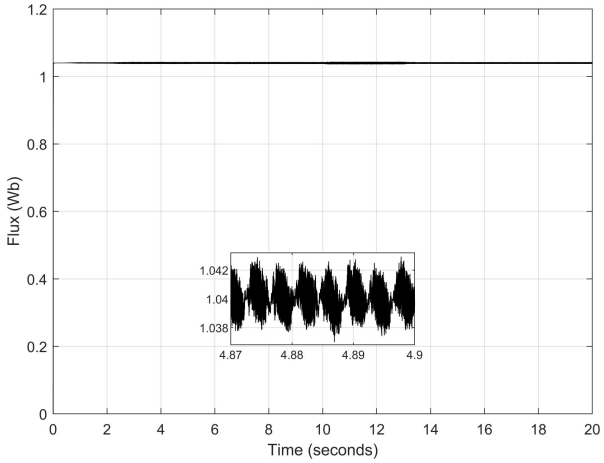

Figure 4-28: DTC-SVM-FTC – Stator flux magnitude

The implementation of DTC-SVM using closed-loop torque and flux control presents significant advantages when compared to both the CDTC and DTC-SVM systems investigated. Reductions in the torque ripple, flux ripple, current ripple, and THD of the current waveform are noticed when compared to both of the previous schemes investigated. As a result, the DTC-SVM-FTC

technique presented further improves the DTC-SVM-TC structure investigated for implementation in EV systems and is consequently a more applicable system for EV traction motor control.

4.5. Fuzzy DTC – Results

The authors in [28] and [29] both provide reviews of direct torque control techniques for induction motor drives and split the various improvements that can be made to CDTC into two categories, namely, typical and modern improvement techniques. Both articles indicate that the general structure of DTC-SVM is classified as a typical improvement technique for the CDTC system. However, the fuzzy DTC system, which is investigated in this section, is an artificial intelligence-based DTC technique and, as a result, is classified as a modern improvement technique. Theoretically, fuzzy DTC provides higher precision, with lower torque and flux ripple, and a faster dynamic torque response than DTC-SVM; however, with a more complex control algorithm and higher computation time [29]. The speed response obtained from the fuzzy DTC system is equivalent to that obtained from DTC-SVM-FTC, as shown in Figure 4-29. The system responds well to all speed changes in the drive cycle, with very little overshoot or undershoot and also exhibits negligible steady-state error. These observations are further confirmed by the induction motor speed error when compared to the desired or reference speed, shown in Figure 4-30.

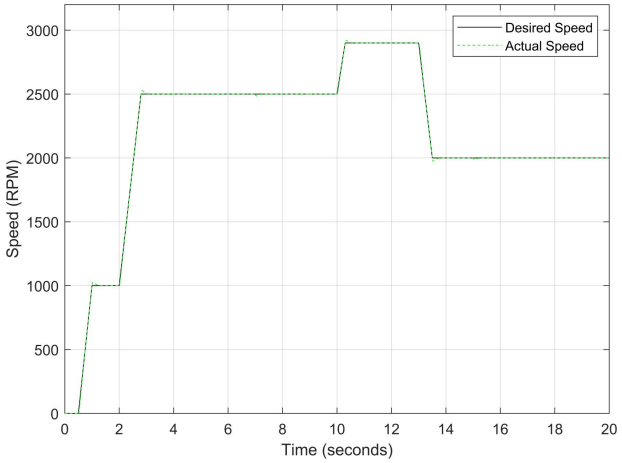

Figure 4-29: Fuzzy DTC – Induction motor speed

The developed torque that the induction motor supplies to the load in comparison to the load torque is shown in Figure 4-31. This is a notable result, as control of the developed torque through fuzzy membership functions offers improved torque ripple compared to the investigated DTC-SVM-FTC structure. The highest torque ripple at any point during the drive cycle was found to be 2.82 N.m when the motor was operating at a speed of 2900 rpm, with a load torque of 60 N.m. In addition to the reduced torque ripple exhibited, the torque ripple remains largely constant throughout the drive cycle, without major variation with changes in the speed or load torque. This is advantageous as the torque ripple in both CDTC and DTC-SVM-TC vary considerably with

the operating conditions of the motor. It should also be noted that fuzzy DTC still responds well to step inputs, allowing for a fast dynamic torque response with very little overshoot. As a result, the fuzzy DTC mechanism simulated enables improved EV rideability when compared to the DTC methods previously investigated. A more comprehensive assessment of the torque ripple during all periods of the drive cycle is provided in Table 4-1 (found in section 4.7).

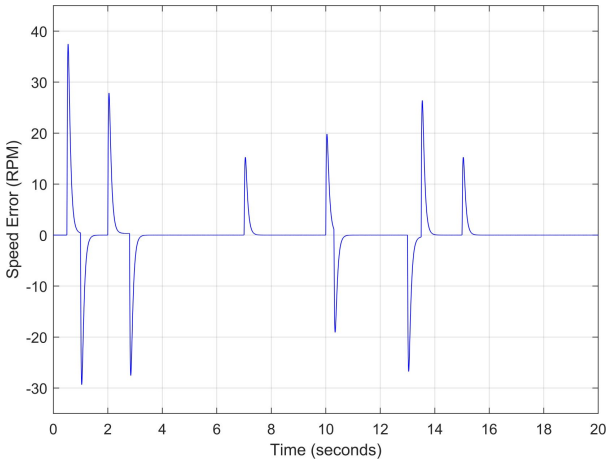

Figure 4-30: Fuzzy DTC – Induction motor speed error

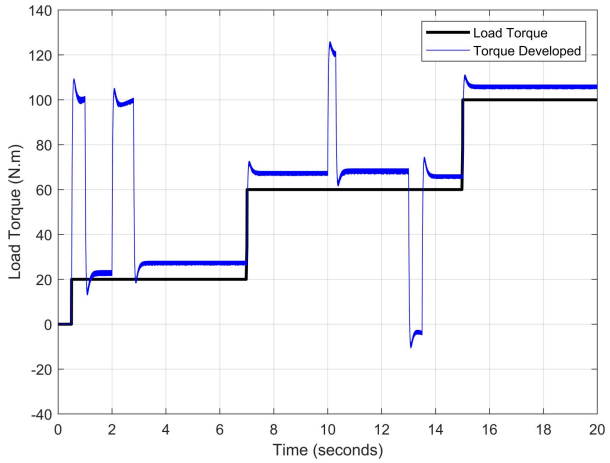

Figure 4-31: Fuzzy DTC – Torque developed by induction motor (500 kHz)

Figure 4-32 shows the steady-state voltage generated from the two-level three-phase inverter supplying the induction motor when the motor was operating at 2500 rpm with a load torque of 20 N.m. The voltage waveform shows no significant change from the DTC techniques investigated previously and is an expected result for a two-level three-phase inverter. However, the inverter current supplied to the induction motor, shown in Figure 4-33, presents an improved result compared to CDTC and both DTC-SVM systems. Zoomed-in portions of both the Phase A and the three-phase steady-state inverter current supplied to the induction motor when the motor was operating at 2500 rpm with a load torque of 20 N.m are shown, indicating the reduced current ripple and increased quality of the current waveform. Furthermore, the FFT analysis (the result of which is shown in Figure 4-34), performed while the motor was operating at 2500 rpm (fundamental frequency of ~41.67 Hz) with a load torque of 20 N.m, indicates an improvement

in the THD of the current waveform when compared to DTC-SVM-FTC, with the THD measured to be 4.33%. However, further comparison between the FFT results between fuzzy DTC and DTC-SVM-FTC indicates that the current waveform obtained when utilising fuzzy DTC also shows significantly reduced 5^{th} and 7^{th} harmonic components. As a result, the fuzzy DTC mechanism produces an improved current waveform when compared to other DTC mechanisms previously investigated. The quality of the current waveform generated from the fuzzy DTC mechanism is further discussed in Table 4-2 (found in section 4.7).

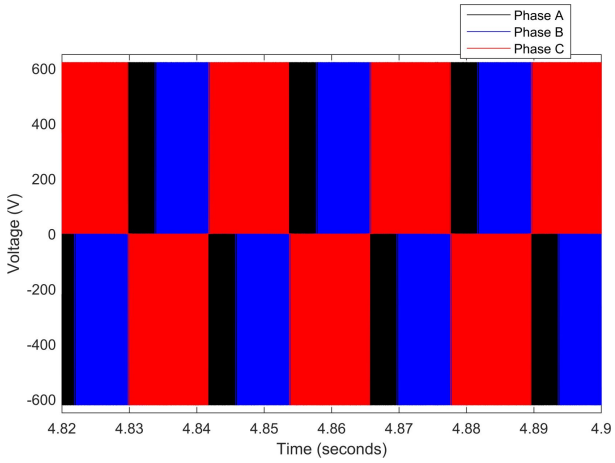

Figure 4-32: Fuzzy DTC – Three-phase inverter voltage

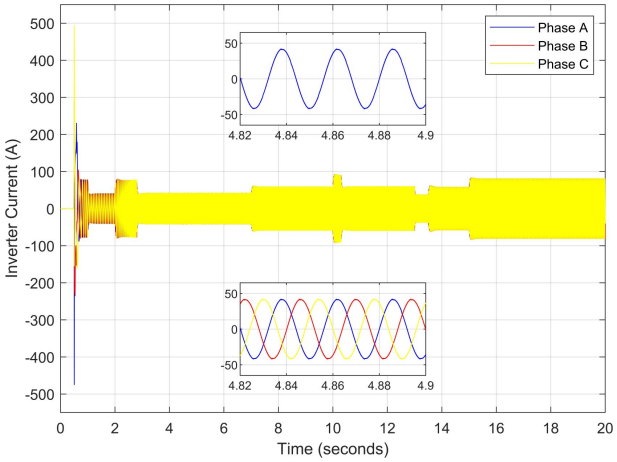

Figure 4-33: Fuzzy DTC – Three-phase inverter current

The q- and d-axis components of the stator flux, both of which are a sinusoidal waveform with an amplitude of approximately 1.04 Wb (controlled by the stator flux magnitude reference), are shown in Figure 4-35. Although Figure 4-35 indicates a desired result, the stator flux trajectory and stator flux magnitude shown in Figure 4-36 and Figure 4-37, respectively, provide a better indication of the performance of the fuzzy DTC system. A significantly narrower circular flux band width and corresponding reduced stator flux ripple can be observed from the fuzzy DTC system when compared with DTC-SVM-FTC. The significantly reduced flux ripple can be easily observed in the zoomed-in portion of the plot shown in Figure 4-37, which was measured when the motor was operating in steady-state conditions, with a speed of 2500 rpm and a load torque

of 20 N.m. A stator flux ripple of 2.78 mWb was observed during this period, which is a significant reduction in comparison to the CDTC and DTC-SVM schemes investigated in this dissertation. The large improvement noticed is due to the use of fuzzy membership functions for control of the stator flux. Additional assessment of the stator flux results obtained from the fuzzy DTC system is provided in Table 4-2 (found in section 4.7).

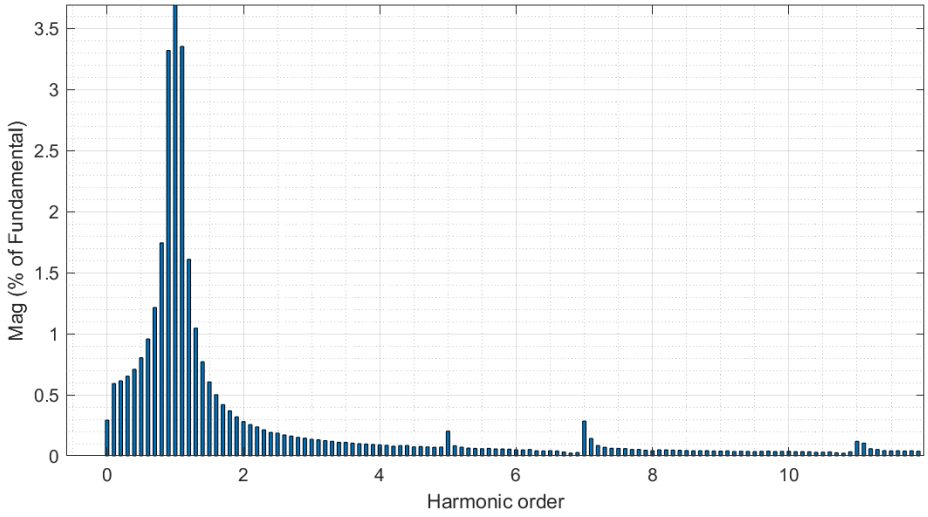

Figure 4-34: Fuzzy DTC – FFT analysis of the current waveform (phase A)

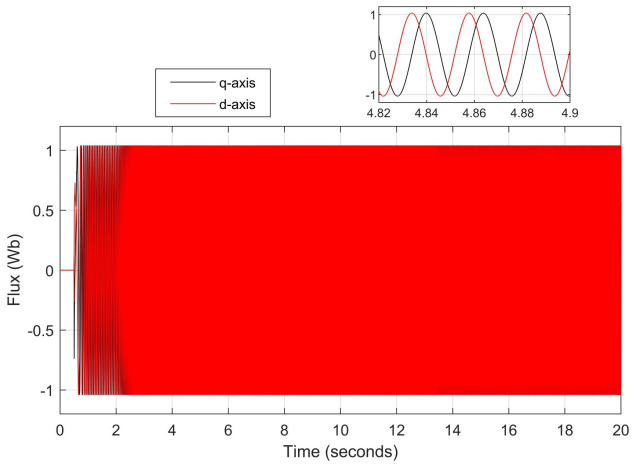

Figure 4-35: Fuzzy DTC – Stator flux (d- and q-axis)

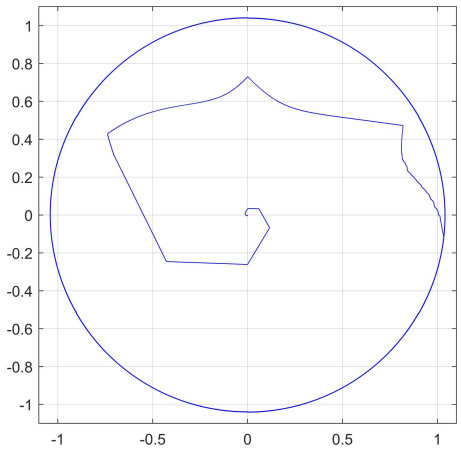

Figure 4-36: Fuzzy DTC – Stator flux trajectory

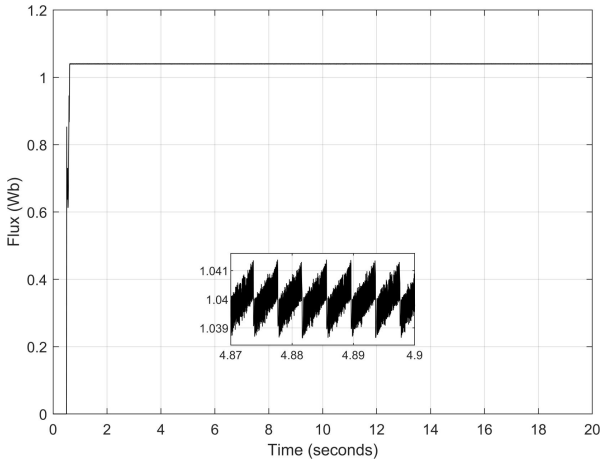

Figure 4-37: Fuzzy DTC – Stator flux magnitude

Control of the electromagnetic torque and stator flux with the use of a fuzzy logic controller provides significant advantages over the hysteresis and SVM control methods utilised in CDTC and DTC-SVM. The fuzzy DTC system exhibits significantly improved torque, current and flux ripples, improving the overall performance of the traction motor drive. However, the fuzzy DTC mechanism has a more complex algorithm structure and is a more computationally expensive control scheme.

4.6. Field-Oriented Control – Results

In comparison to CDTC, field-oriented control requires coordinate transformation into the synchronously rotating reference frame rather than the stationary stator reference frame. FOC requires the electromagnetic torque and rotor flux as reference inputs and makes use of the decoupling of the stator current into two orthogonal components for control of the inverter switching states. An SVM switching technique is also utilised in FOC, and an SVM frequency of 20 kHz was implemented in the mechanism investigated in this chapter. Reduced torque ripple and an improved stator current waveform are expected from the FOC system when compared with CDTC; however, it is worth noting that the FOC scheme is a more computationally intensive online control method. The induction motor speed response in comparison to the reference or desired speed and the induction motor speed error are shown in Figure 4-38 and Figure 4-39, respectively. The drive cycle used to test the DTC mechanisms investigated was utilised again for the FOC system to offer comparable results. FOC produces an equivalent speed response to the DTC systems previously investigated, with a fast and stable dynamic response, negligible steady-state error and an overshoot/undershoot of less than 3% during all speed changes in the drive cycle.

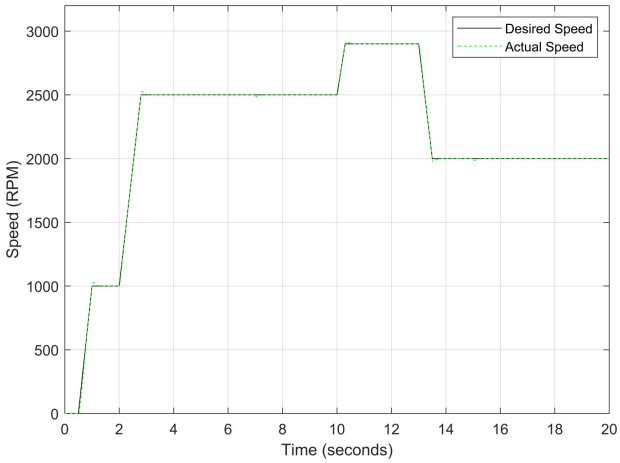

Figure 4-38: FOC – Induction motor speed

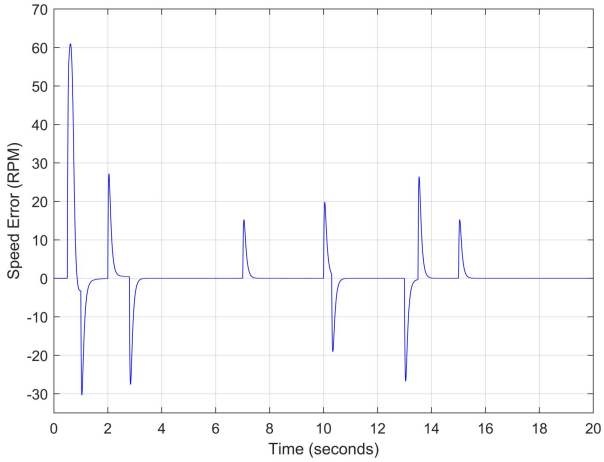

Figure 4-39: FOC – Induction motor speed error

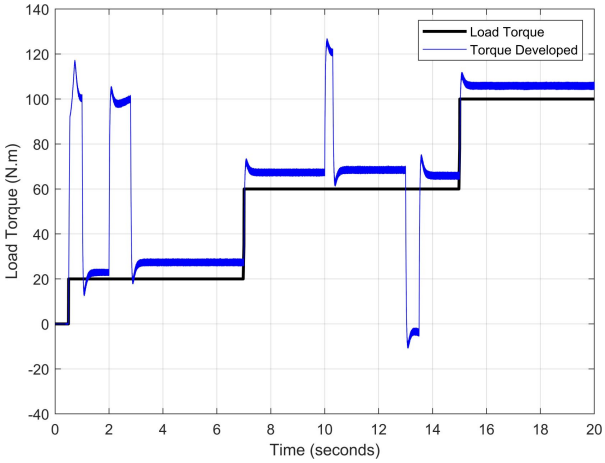

Figure 4-40: FOC – Torque developed by induction motor (500 kHz)

Although the FOC system produced a similar speed response result to that observed from CDTC, the FOC scheme provides notable improvements in the developed electromagnetic torque. Figure 4-40 shows the developed torque supplied to the load in comparison to the load torque. The result indicates that FOC is also able to produce a fast and stable dynamic torque response, responding well to step inputs in the load torque with very little overshoot or undershoot. Interestingly, the torque ripple observed from the FOC system remains largely constant throughout the drive cycle,

with the highest torque ripple measured to be 3.7 N.m, when the motor was operating at 2000 rpm with a load torque of 100 N.m. This is an important result, as the torque response obtained from the FOC system is comparable to that obtained from improved DTC systems. FOC mitigates a large amount of the unwanted torque ripple observed in CDTC and performs in a similar manner to the DTC-SVM-FTC scheme investigated. Further analysis of the torque ripple observed from the FOC scheme is provided in Table 4-1 (found in section 4.7).

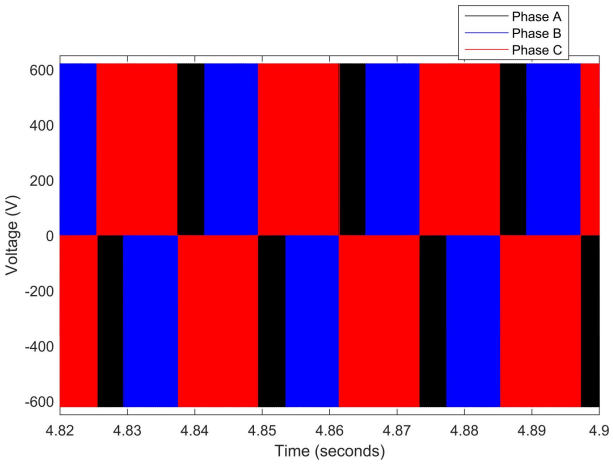

Figure 4-41: FOC – Three-phase inverter voltage

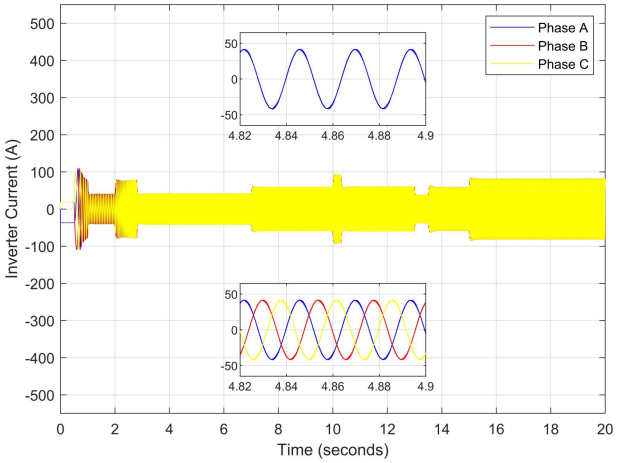

Figure 4-42: FOC – Three-phase inverter current

The FOC system exhibits an expected steady-state voltage result, as shown in Figure 4-41. The result shown is the steady-state voltage generated from the two-level three-phase inverter supplying the induction motor when the motor was operating at 2500 rpm with a load torque of 20 N.m. While the steady-state inverter voltage result is equivalent to that observed from CDTC, the current waveform, shown in Figure 4-42, and the FFT analysis of the current waveform, shown in Figure 4-43, indicate significantly improved results. Zoomed-in portions of both the Phase A and the three-phase steady-state inverter current supplied to the induction motor when the motor was operating at 2500 rpm with a load torque of 20 N.m are also shown in Figure 4-42. It can be observed from the zoomed-in portions shown that a current waveform with low ripple and distortion is generated. This is further confirmed by the FFT analysis, which was performed

over ten cycles of the current waveform while the motor was operating at 2500 rpm (fundamental frequency of ~41.67 Hz) with a load torque of 20 N.m. A THD of 4.76% was measured, with no undesirable odd harmonic components present in the waveform. As a result, the current waveform generated from the FOC scheme exhibits comparable characteristics to that observed from DTC-SVM-FTC and fuzzy DTC. Additional analysis of the current waveform quality is provided in Table 4-2 (found in section 4.7).

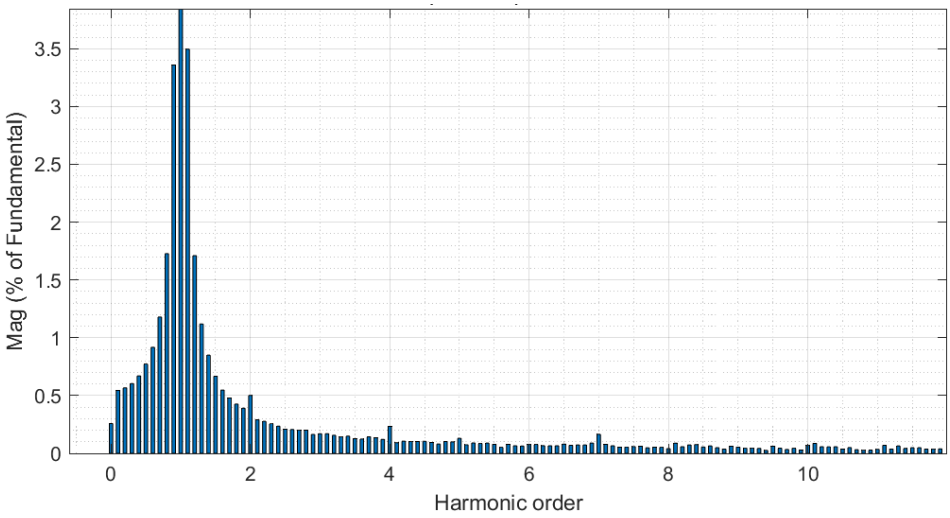

Figure 4-43: FOC – FFT analysis of the current waveform (phase A)

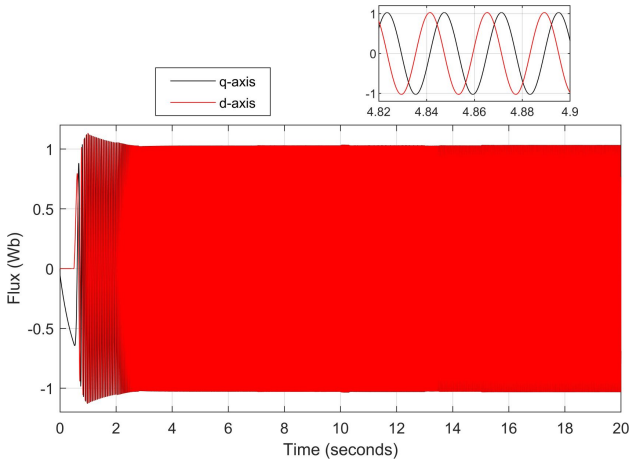

Figure 4-44: FOC – Stator flux (d- and q-axis)

Figure 4-44 and Figure 4-46 show the q- and d-axis components of the stator and rotor flux, respectively. Interestingly, the FOC system utilises the rotor flux as a reference rather than the stator flux, and as a result, the stator flux is not directly controlled in the field-oriented control scheme. However, the FOC system still provides a desirable stator flux response, with the flux in the q- and d-axes having a largely consistent amplitude of approximately 1.03 Wb throughout the drive cycle utilised. This results in a largely constant stator flux magnitude, as shown in Figure 4-45. Figure 4-45 also shows a zoomed-in portion of the stator flux when the motor was operating in steady-state conditions, with a speed of 2500 rpm and a load torque of 20 N.m. This zoomed-in portion indicates that the FOC scheme exhibits a low stator flux ripple (measured to be 4.70

mWb during this period), which is comparable to the improved DTC schemes investigated in this chapter. However, the stator flux result obtained from the FOC system indicates that the stator flux has some initial overshoot, which is not present in any of the DTC systems investigated and also takes significantly longer to reach the desired value on start-up. Despite the performance of the stator flux during start-up, the overall performance of the drive system is not impacted.

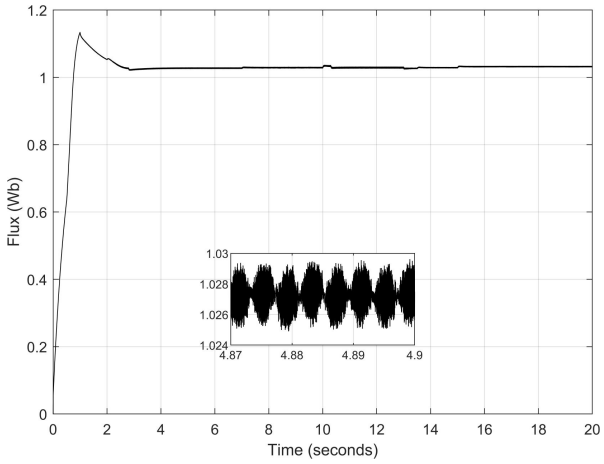

Figure 4-45: FOC – Stator flux magnitude

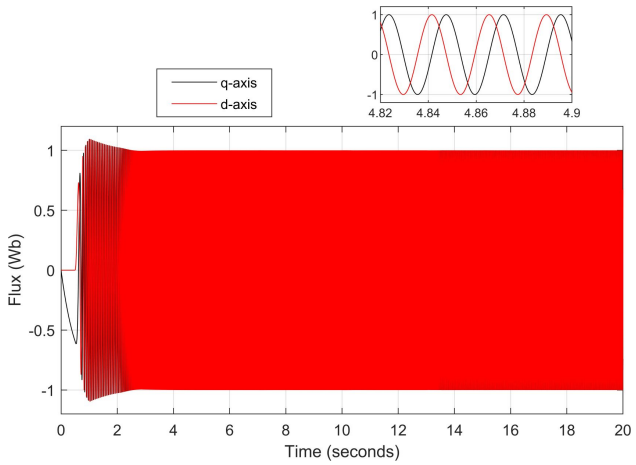

Figure 4-46: FOC – Rotor flux (d- and q-axis)

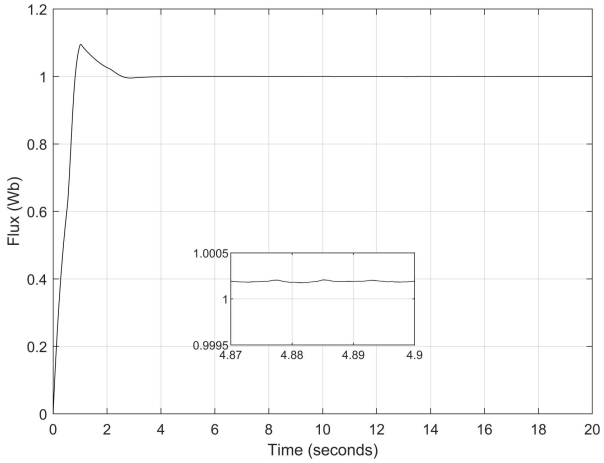

Figure 4-47: FOC – Rotor flux magnitude

The rotor flux magnitude result shown in Figure 4-47 also indicates an initial overshoot in the rotor flux. The rotor flux reference was maintained constant at 1 Wb throughout the drive cycle tested, and once the rotor flux returns to the reference value after the initial overshoot, it can be observed that the rotor flux is consistently controlled with negligible ripple or steady-state error. This is further confirmed by the zoomed-in portion of the rotor flux shown in Figure 4-47, which was measured when the motor was operating with a speed of 2500 rpm and a load torque of 20 N.m. Further analysis of the stator flux performance of FOC in comparison to the DTC schemes investigated is provided in Table 4-2 (found in section 4.7).

In general, the field-oriented control system showed various improvements compared to the CDTC scheme. Low torque, current and flux ripples were observed, with the current waveform supplying the induction motor also found to have a favourable THD. Furthermore, a fast and stable torque response was still achieved with FOC, with the system offering largely comparable results to those obtained from the improved DTC schemes investigated. However, FOC exhibits some initial overshoot in the stator and rotor flux results, which is not seen in the improved DTC mechanisms. It is also important to note that while FOC provides improved results when compared with CDTC, it is a more computationally intensive online control method.

4.7. Discussion and Initial Comparison of Control Techniques

Determination of the most suitable control techniques for application in the traction motor control system of an EV is most effectively carried out through the comparison of the speed, torque, current and flux responses of the systems investigated. The mechanisms all offered comparable speed control results, exhibiting fast and stable dynamic speed responses, with negligible overshoot or undershoot in response to ramp changes in the drive cycle utilised. Ramp changes in the desired speed were preferred to step changes as they more accurately simulate the operating conditions an EV may experience. Furthermore, both the DTC and FOC mechanisms investigated provided a fast and stable torque response when subjected to step changes in the load torque. However, the steady-state torque ripple provides a useful metric for comparison of the control mechanisms.

The steady-state torque ripple for each control method during various operating conditions of the drive cycle is provided in Table 4-1, with a graphical comparison of the methods shown in Figure 4-48. The comparison indicates that CDTC provides the worst torque ripple results, with the highest ripple in most operating conditions and significant variation in the torque ripple between operating conditions. DTC-SVM-TC provides reduced torque ripple in all operating conditions compared to CDTC, except when the motor is operating at 1000 rpm. DTC-SVM-TC performs particularly well when the motor is operating at 2000 rpm; however, the mechanism also shows

significant torque ripple variation across operating conditions, with poor ripple performance at lower speeds. DTC-SVM-FTC, fuzzy DTC and FOC all exhibit significantly better torque ripple results than CDTC and DTC-SVM-TC. In all three mechanisms, the ripple is significantly reduced in most operating conditions and remains largely constant throughout the drive cycle. While DTC-SVM-FTC performs better than FOC, fuzzy DTC performs significantly better than all of the other mechanisms, offering significantly reduced and stable steady-state torque ripple results.

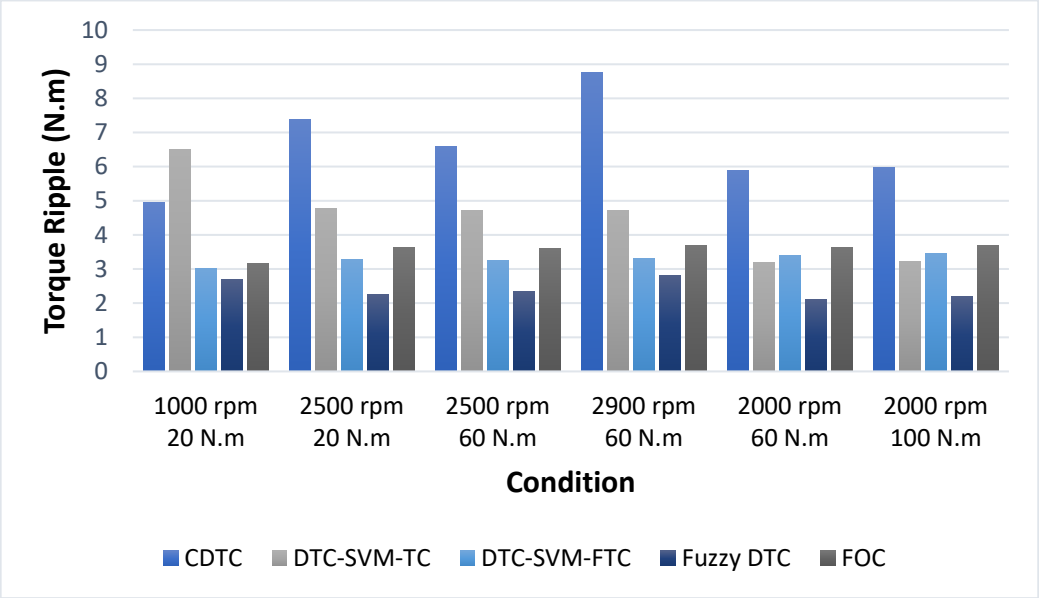

Figure 4-48: Comparison of motor control techniques (torque ripple)

Table 4-1: Comparison of motor control techniques (torque ripple)

Operating Condition	Torque Ripple (N.m)				
	CDTC	DTC-SVM-TC	DTC-SVM-FTC	Fuzzy DTC	FOC
1000 rpm, 20 N.m	4.95	6.50	3.01	2.70	3.17
2500 rpm, 20 N.m	7.38	4.77	3.27	2.25	3.62
2500 rpm, 60 N.m	6.58	4.71	3.26	2.34	3.61
2900 rpm, 60 N.m	8.75	4.70	3.30	2.82	3.7
2000 rpm, 60 N.m	5.90	3.2	3.39	2.10	3.64
2000 rpm, 100 N.m	5.98	3.22	3.45	2.19	3.7

A comparison between the current and flux results of the systems investigated is provided in Table 4-2, with a graphical comparison given in Figure 4-49. The current and flux results shown were obtained when the motor was operating in steady-state conditions, with a speed of 2500 rpm and a load torque of 20 N.m. The comparison indicates that similarly to the steady-state torque ripple results discussed, DTC-SVM-FTC, fuzzy DTC and FOC are the best-performing methods, offering the lowest current and flux ripples, as well as reduced THD of the current waveform.

DTC-SVM-TC provides a significantly improved current waveform when compared with CDTC; however, the mechanism controls the stator flux in an open-loop manner and suffers from a high flux ripple. The fuzzy DTC system performs significantly better than any of the other systems investigated when analysing the current ripple, flux ripple and current THD. DTC-SVM-FTC and FOC have similar performance when considering the current waveform; however, FOC has a reduced stator flux ripple.

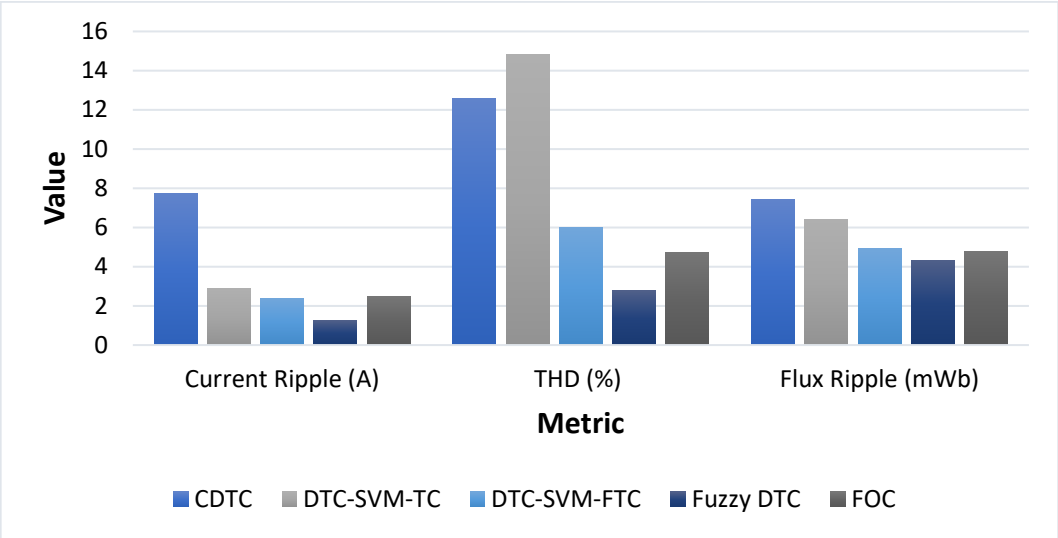

Figure 4-49: Comparison of motor control techniques (current and flux)

Table 4-2: Comparison of motor control techniques (current and flux)

Condition: 2500 rpm with a torque load of 20 N.m					
Metric	**CDTC**	**DTC-SVM-TC**	**DTC-SVM-FTC**	**Fuzzy DTC**	**FOC**
Current Ripple (A)	7.72	2.87	2.40	1.27	2.47
Stator Flux Ripple (mWb)	12.6	14.8	6.00	2.78	4.70
THD (%)	7.43	6.41	4.91	4.33	4.76

4.8. Conclusion

Due to the importance of the traction motor control system in EV drivetrains, this chapter aims to provide an initial comparison of various induction motor control techniques to assess their suitability for application in EV mechanisms. The investigation was carried out using the standard structure of each control mechanism, without field-weakening or sensorless speed control, and indicated that fuzzy DTC provides the most promising overall performance for EV applications. However, DTC-SVM-FTC and FOC also provide suitable performance and show improvement compared to CDTC and DTC-SVM-TC. As DTC-SVM-FTC provides improved torque ripple when compared with FOC, DTC-SVM-FTC and fuzzy DTC are preferred for further investigation. The next chapter of this dissertation investigates the performance of both systems when field-weakening control is integrated into the control mechanism.

5. Chapter 5 – Comparison of Traction Motor Control Systems with Field-Weakening Control (Simulation Results)

5.1. Introduction

Initial investigation of the standard motor control structures indicated that DTC-SVM-FTC and fuzzy DTC are suitable techniques for use in EV traction motor control mechanisms. However, without the inclusion of field-weakening control, the mechanisms cannot meet the speed requirements of high-speed urban and highway driving. As a result, field-weakening control is an essential component in the traction motor control system of an EV and is investigated in the DTC-SVM-FTC and fuzzy DTC systems in this chapter. Field-weakening control enables operation of the traction motor above the rated speed specification. Consequently, the drive cycle used for the simulations discussed in this chapter was designed to assess the performance of the drive system across the entire speed range required while also investigating whether the control structure enables stable operation throughout the drive cycle. In order to maintain consistency between investigations in this dissertation, a sampling frequency of 500 kHz was utilised for the mechanisms in this chapter, with an SVM frequency of 20 kHz utilised for the DTC-SVM-FTC system.

5.2. Comparison of DTC-SVM-FTC and Fuzzy DTC

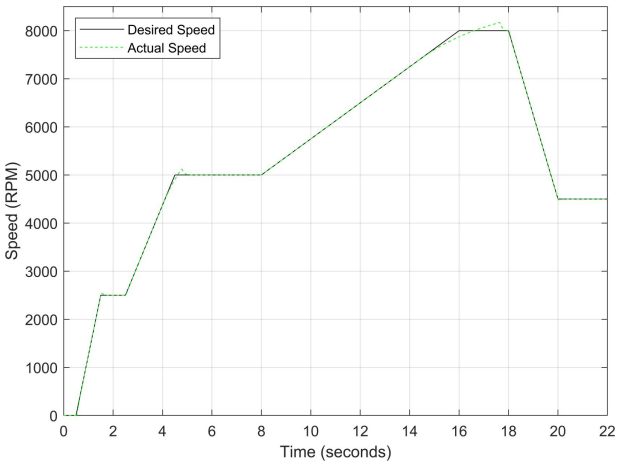

Figure 5-1: DTC-SVM-FTC with FW – Induction motor speed

The fundamental structure of both the DTC-SVM-FTC and fuzzy DTC mechanisms is unchanged when field-weakening is added; however, a dynamic flux reference calculator, as well as the torque limits discussed in section 3.6, are also incorporated into the model. Figure 5-1 and Figure 5-2 show the motor speed in comparison to the reference or desired speed for the DTC-SVM-FTC and fuzzy DTC systems, respectively. The initial drive cycle used to test the traction motor control systems in Chapter 4 is not applicable to test the field-weakening functionality of the drive system, as field-weakening enables the operation of the motor above its base speed. As a result,

the drive cycle is adapted to have a maximum speed of 8000 rpm, which is approximately the maximum motor speed required.

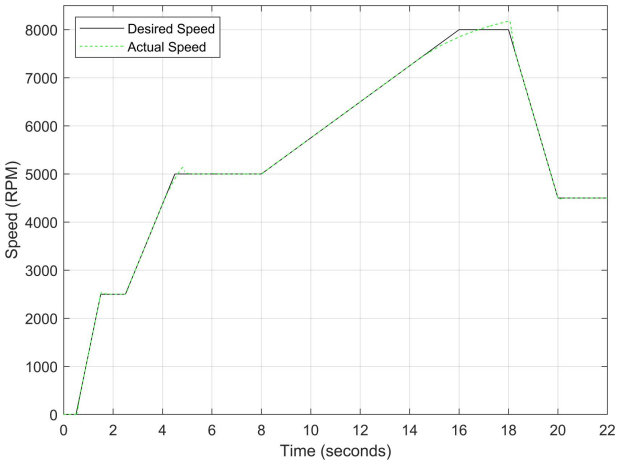

Figure 5-2: Fuzzy DTC with FW – Induction motor speed

Both Figure 5-1 and Figure 5-2 show that the speed is correctly tracked for most of the drive cycle in both of the control mechanisms being investigated. However, the results show that there are sections during which the motor acceleration does not match the desired acceleration, and as a result, the motor takes longer to reach the desired steady-state speed. This is a result of the torque limiting that is implemented with the incorporation of field-weakening control. The torque is limited to ensure that the motor remains in stable operation. The sections of the drive cycle in which the desired acceleration is not achieved in both systems can be more clearly observed in Figure 5-3 and Figure 5-4, which show the induction motor speed error when compared to the desired or reference speed in the DTC-SVM-FTC and fuzzy DTC systems, respectively.

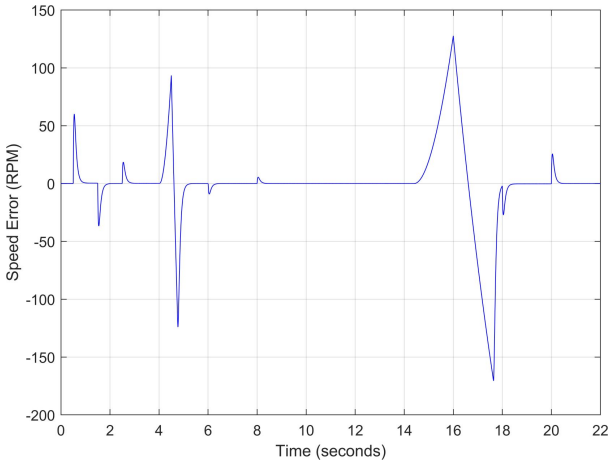

Figure 5-3: DTC-SVM-FTC with FW – Induction motor speed error

Both the speed and speed error results highlight that there is a difference between the two systems in regions in which torque limiting is required (4 to 5 seconds and 14 to 18 seconds). For operation at the reference speed defined by the drive cycle used, fuzzy DTC has a slightly higher torque reference than DTC-SVM-FTC, and as a result, torque limiting occurs marginally earlier in the fuzzy DTC system. This results in a higher speed error in the fuzzy DTC system in regions where

torque limiting is required. However, the higher speed error occurs only under operating conditions in which the system cannot meet the desired acceleration, and a lower acceleration must be used to ensure stable operation of the motor. In general, this is not a concern, as it is not expected that acceleration of this nature is required in normal operating conditions. The drive cycle utilised in this chapter was designed to allow for illustration of the torque limiting functionality that was implemented in the field-weakening system. If high levels of acceleration are required in certain cases, the PI controller in the speed control loop can be designed to minimise the speed error in operating conditions in which torque limiting is required.

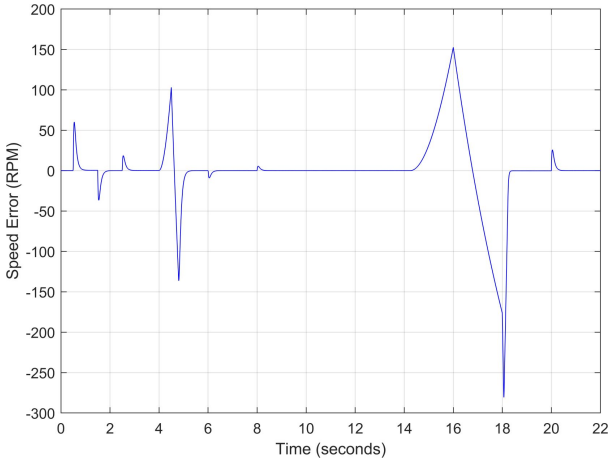

Figure 5-4: Fuzzy DTC with FW – Induction motor speed error

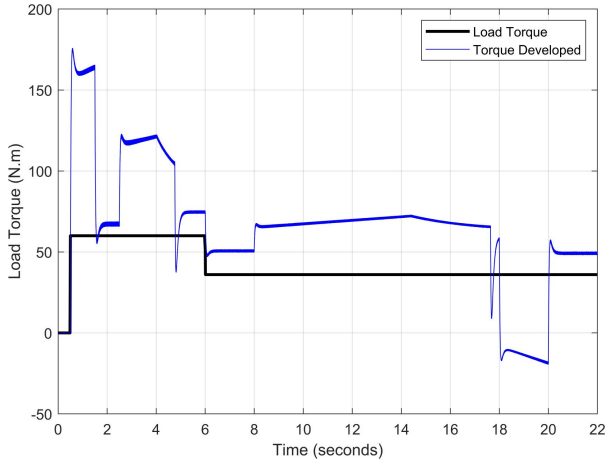

Figure 5-5: DTC-SVM-FTC with FW – Torque developed by induction motor (500 kHz)

Figure 5-5 and Figure 5-6 show the developed torque that the induction motor supplied to the load in comparison to the load torque when field-weakening was implemented in the DTC-SVM-FTC and fuzzy DTC models, respectively. The figures indicate that both schemes produce suitable torque ripple across the required speed range (with a maximum speed of more than two times the base speed). A very notable result occurs when the motor is not able to match the desired acceleration (4 to 5 seconds and 14 to 18 seconds). The torque graph shows that the torque is limited in order to maintain stable operation of the motor. The torque limiting is inversely proportional to the speed, governed by the second region in equation 3-16, as the operating

condition of the motor matches the mathematical inequality given by $\omega_{base} < |\omega_r| \leq \omega_{base1}$. The implemented field-weakening algorithm enables the motor to meet the maximum speed requirement while being forced to accelerate in a stable manner.

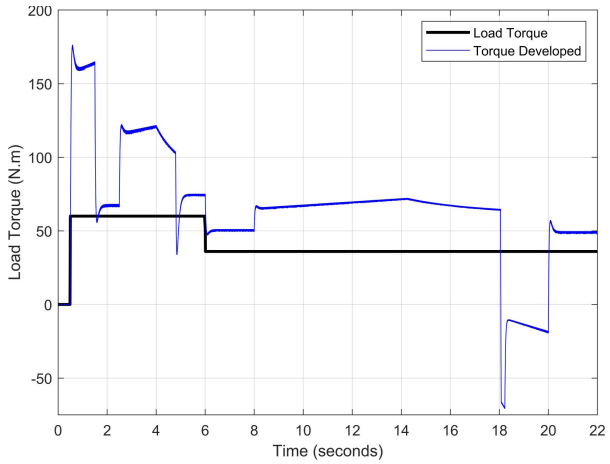

Figure 5-6: Fuzzy DTC with FW – Torque developed by induction motor (500 kHz)

Although it is not as noticeable in the developed torque results produced by the systems, torque limiting occurs marginally earlier in the fuzzy DTC system as observed in the speed results obtained. While both mechanisms produce suitable torque ripple throughout the drive cycle utilised, the fuzzy DTC system provides lower torque ripple in the field-weakening region. However, it was found that both systems exhibit largely constant torque ripple across variation in the desired speed and load torque. Both systems also respond well to step inputs in the load torque in the field-weakening region, enabling a fast dynamic torque response. The torque response obtained from both systems indicates that adequate vehicle rideability is achieved throughout the drive cycle utilised. Additional comparison of the torque ripple results for the two systems investigated is provided in Table 5-1(found in section 5.3).

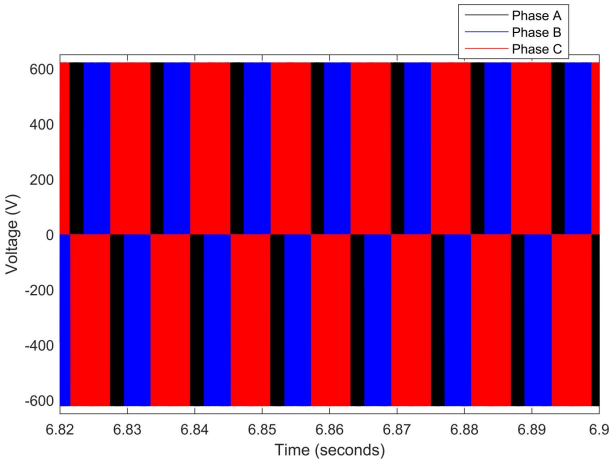

Figure 5-7: DTC-DVM-FTC with FW – Three-phase inverter voltage

The inverter voltages observed in the simulation of the DTC-SVM-FTC and fuzzy DTC systems are shown in Figure 5-7 and Figure 5-8, respectively. As expected, the frequency of the voltage waveform increases with increasing frequency; however, field-weakening control has no notable

impact on the voltage results obtained. Figure 5-9 and Figure 5-10 show the inverter current supplied to the induction motor during the entire drive cycle in the DTC-SVM-FTC and fuzzy DTC mechanisms, respectively. In addition, zoomed-in portions of both the Phase A and the three-phase steady-state inverter current supplied to the induction motor, when the motor was operating at 5000 rpm with a load torque of 36 N.m, are shown. The inverter current is sinusoidal in both mechanisms, and the current magnitude is proportional to the torque developed by the motor. Both systems produce current waveforms with low distortion or ripple, even in cases when the motor is operated well above the specified base speed.

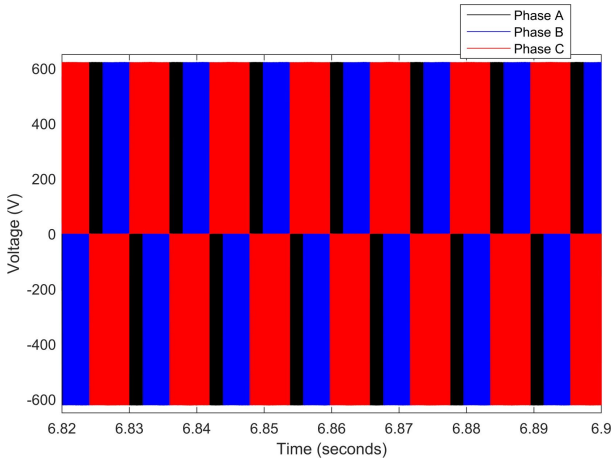

Figure 5-8: Fuzzy DTC with FW – Three-phase inverter voltage

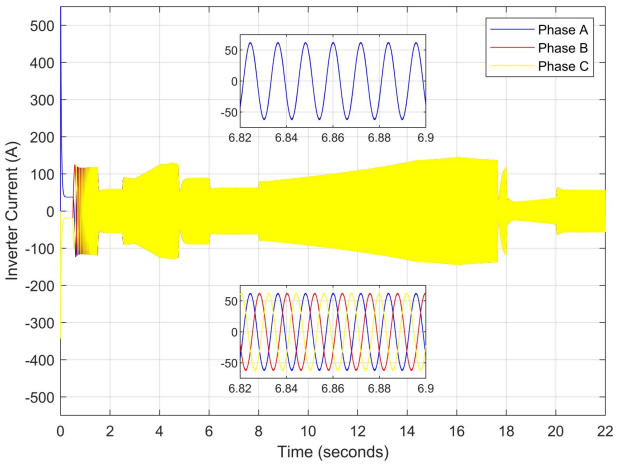

Figure 5-9: DTC-SVM-FTC with FW – Three-phase inverter current

The harmonic distortion of the current waveforms is assessed using FFT analysis, with the results of the analysis for DTC-SVM-FTC and fuzzy DTC shown in Figure 5-11 and Figure 5-12, respectively. The FFT analysis was performed during steady-state conditions while the motor was operating at 5000 rpm (fundamental frequency of ~83.33 Hz) with a load torque of 36 N.m. As in Chapter 4, the FFT analysis was performed over ten cycles, allowing for a resolution of ~8.33 Hz under the operating conditions utilised. The THD for the DTC-SVM-FTC system was found to be 12.55%, whereas it was found to be 12.05% for the fuzzy DTC system. This is significantly higher than the THD results obtained when the motor was operating at a lower speed and torque,

as discussed in Chapter 4. However, it should be noted that the number of cycles over which the FFT analysis is performed significantly impacts the THD measured. A much lower THD is obtained if the analysis is performed using only frequencies which correspond to whole numbered harmonics. It can be further observed that in both systems, low 5^{th}, 7^{th}, 9^{th} and 11^{th} harmonic components are observed, which is a favourable result. Additional comparisons of the current ripple and THD results obtained are provided in Table 5-2 (found in section 5.3).

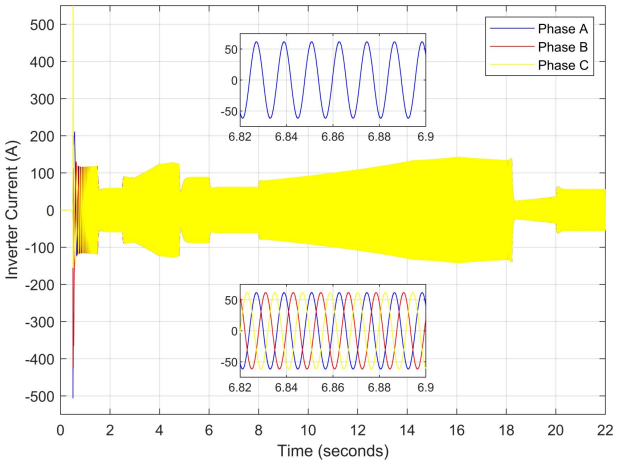

Figure 5-10: Fuzzy DTC with FW – Three-phase inverter current

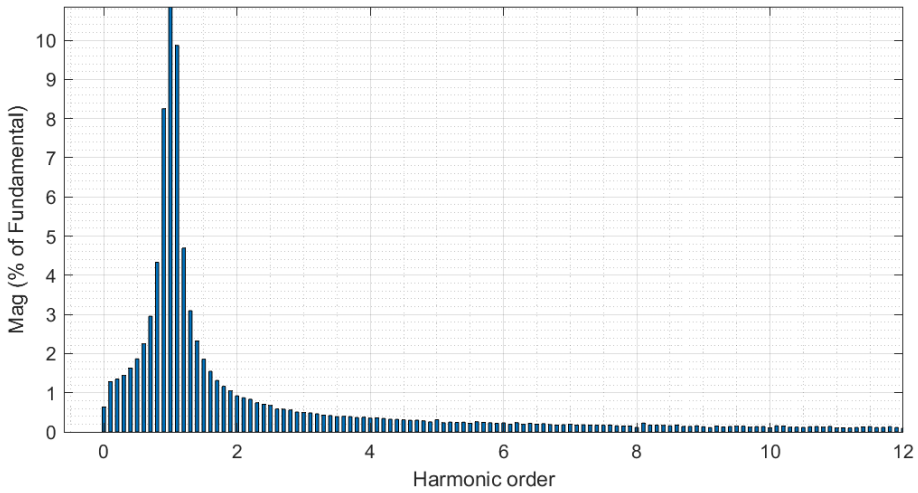

Figure 5-11: DTC-SVM-FTC with FW – FFT analysis of the current waveform (phase A)

The field-weakening method implemented adjusts the stator flux in a manner which is inversely proportional to the rotor speed. However, adjustment of the flux only takes place in operating conditions in which the rotor speed is above the specified base speed. As a result, when field-weakening control is in operation, the stator flux should be adjusted in a hyperbolic manner. Such adjustment of the stator flux can be seen in the stator flux magnitude graph, shown in Figure 5-13 for the DTC-SVM-FTC mechanism and Figure 5-14 for the fuzzy DTC mechanism. The stator flux magnitude graphs also show a zoomed-in portion of the stator flux magnitude, which was measured when the motor was operating at a speed of 5000 rpm with a load torque of 36 N.m. The zoomed-in portion of each waveform indicates that the fuzzy DTC system has significantly

improved ripple compared with DTC-SVM-FTC. A comparison of the flux ripple exhibited by the two mechanisms is also given in Table 5-2 (found in section 5.3).

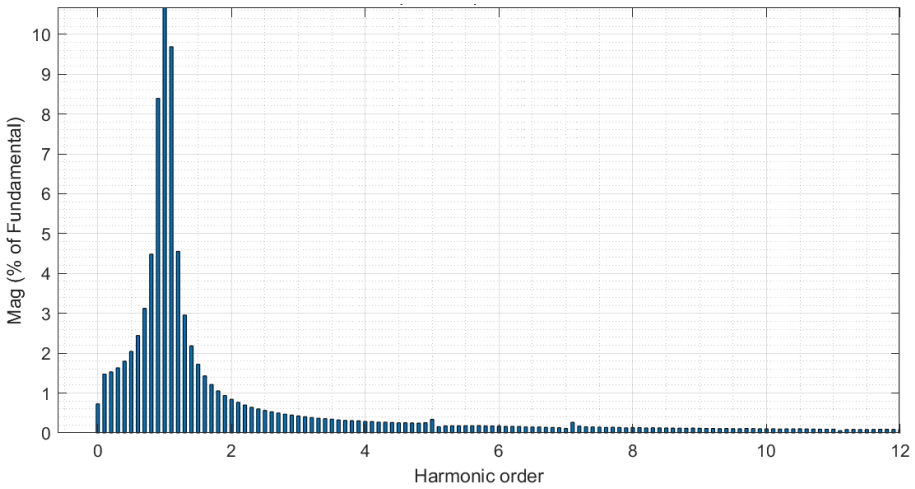

Figure 5-12: Fuzzy DTC with FW – FFT analysis of the current waveform (phase A)

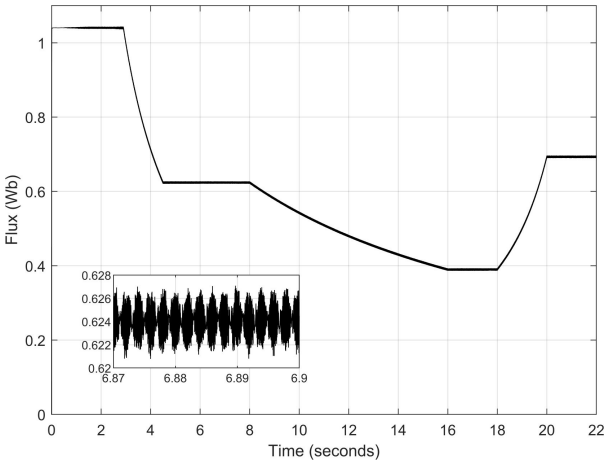

Figure 5-13: DTC-SWM-FTC with FW – Stator flux magnitude

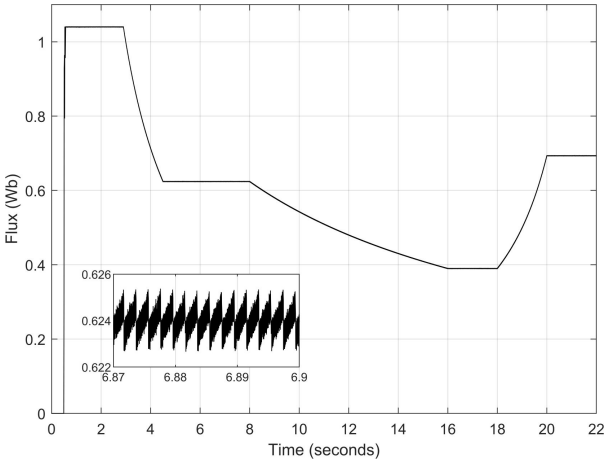

Figure 5-14: Fuzzy DTC with FW – Stator flux magnitude

As can be seen, the stator flux in both systems is decreased using field-weakening control between 2.5 to 4.5 seconds, as well as between 8 to 16 seconds. Furthermore, in periods in which the speed is below the base speed, or the speed of the motor is constant, the stator flux magnitude remains

constant. This can be further confirmed through the d- and q- axis components of the stator flux, shown in Figure 5-15 and Figure 5-16. Additionally, the zoomed-in portion of the stator flux shows smooth sinusoidal oscillations of both the d- and q- axis components in the DTC-SVM-FTC and fuzzy DTC mechanisms.

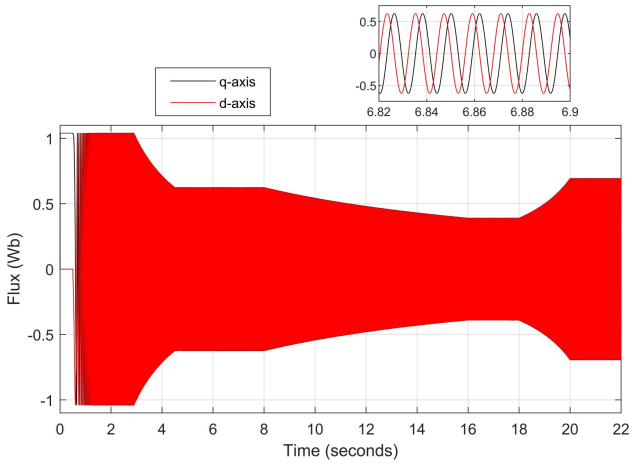

Figure 5-15: DTC-SVM-FTC with FW – Stator flux (d- and q-axis)

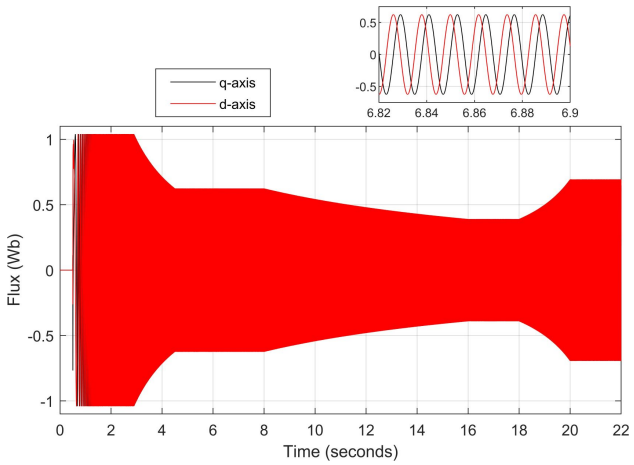

Figure 5-16: Fuzzy DTC with FW – Stator flux (d- and q-axis)

5.3. Discussion

The field-weakening technique implemented produced favourable results in both the DTC-SVM-FTC and fuzzy DTC systems, allowing the traction motor to correctly operate over the entire speed range required. Additionally, the torque is correctly limited to ensure the motor maintains stable operation throughout the entire drive cycle tested. Similarly to the investigation carried out in Chapter 4, a comparison of the DTC-SVM-FTC and fuzzy DTC mechanisms can be most effectively carried out through analysis of the speed, torque, current and flux responses of the two systems.

For the majority of the drive cycle, the two mechanisms offered comparable speed control results, providing a fast and stable dynamic speed response when subjected to ramp changes in the

reference speed, even in cases in which the motor was operating in the field-weakening region. The only difference between the speed responses of the systems can be observed when torque limiting is required to maintain stable operation of the system. Furthermore, the DTC-SVM-FTC and fuzzy DTC systems both respond well to step inputs in the load torque, exhibiting a fast and stable torque response. The steady-state torque ripple for the two mechanisms investigated, measured during various operating conditions, is shown in Table 5-1, with a graphical comparison of the methods provided in Figure 5-17. The torque ripple was measured under all steady-state operating conditions, except for when the motor was operating at 8000 rpm with a load torque of 36 N.m, due to the difference in the speed performance of the two systems as a result of torque limiting. The comparison indicates that fuzzy DTC provides superior torque ripple results across all operating conditions. However, on average, fuzzy DTC offers an improvement of only ~11.5% in the steady-state torque ripple when considering operating conditions which lie in the field-weakening region. Fuzzy DTC offers a more significant improvement when operating at speeds which are below the base speed of the motor.

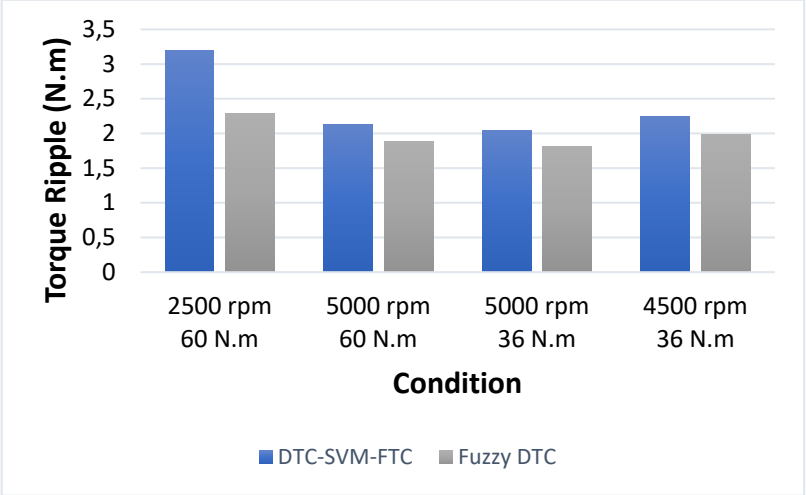

Figure 5-17: DTC-SVM-FTC vs fuzzy DTC (torque ripple)

Table 5-1: Comparison of motor control techniques with field-weakening (torque ripple)

Operating Condition	Torque Ripple (N.m)	
	DTC-SVM-FTC	Fuzzy DTC
2500 rpm, 60 N.m	3.20	2.29
5000 rpm, 60 N.m	2.13	1.88
5000 rpm, 36 N.m	2.04	1.81
4500 rpm, 36 N.m	2.25	1.99

The current and flux results obtained from the DTC-SVM-FTC and fuzzy DTC systems are shown in Table 5-2, with a graphical comparison of the results given in Figure 5-18. The current and flux results provided were measured when the motor was operating in steady-state conditions with a

speed of 5000 rpm and a load torque of 36 N.m. The results indicate that fuzzy DTC offers a significant improvement in the current and stator flux ripple at the operating condition utilised while also improving the current THD. However, as indicated in Table 3-7, fuzzy DTC has a higher computation time as it has a more complex algorithm structure. It should also be noted that both systems investigated provide favourable results for use in EV systems. Both DTC-SVM-FTC and fuzzy DTC provide a fast dynamic speed and torque response with low torque, current, and flux ripples across the entire speed range required. Furthermore, the field-weakening control method implemented correctly adjusts the stator flux, allowing for operation of the motor above the base speed specification while also providing necessary torque limiting to maintain stable operation of the motor.

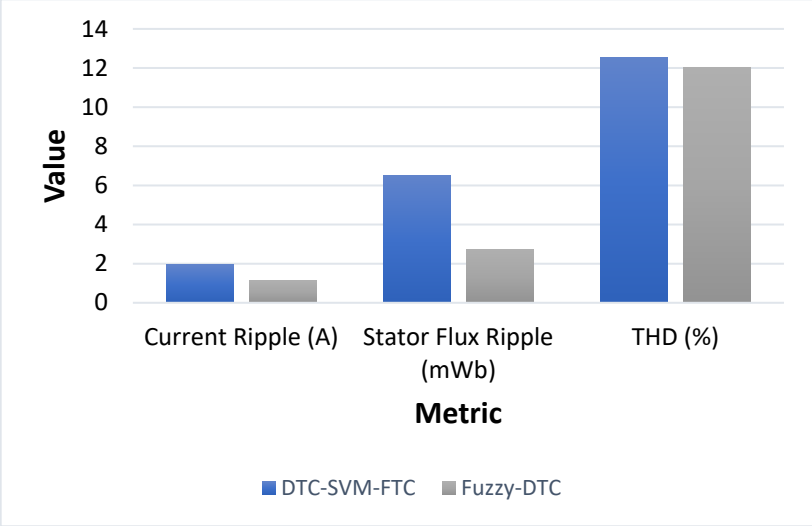

Figure 5-18: DTC-SVM-FTC vs fuzzy DTC (current and flux)

Table 5-2: Comparison of motor control techniques (current and flux)

Condition: 5000 rpm with a torque load of 36 N.m		
Metric	**DTC-SVM-FTC**	**Fuzzy-DTC**
Current Ripple (A)	1.95	1.13
Stator Flux Ripple (mWb)	6.52	2.73
THD (%)	12.55	12.05

5.4. Conclusion

Field-weakening control is essential in traction motor drives utilised in EV systems and is required to enable the operation of the vehicle at speeds necessary for highway driving. This chapter extends the standard structure of the DTC-SVM-FTC and fuzzy DTC mechanisms with the addition of field-weakening control and aims to assess the suitability of the field-weakening control method utilised, as well as provide a comparison between the two systems with field-weakening control implemented. The results indicate that both control mechanisms exhibit low

torque, current and flux ripples while achieving fast dynamic response and stable acceleration throughout the required speed range. Therefore, although the fuzzy DTC system provides improved torque, current and flux ripples, DTC-SVM-FTC provides suitable results for use in EV systems and is chosen for further investigation in this dissertation. DTC-SVM-FTC provides favourable performance while maintaining a simpler algorithm complexity and lower computation time, an important consideration as DTC is a largely online control method. DTC-SVM-FTC is further extended in the next chapter of this dissertation through the investigation of open-loop and closed-loop sensorless control methods for use in vehicular applications.

6. Chapter 6 – Comparison of Sensorless Control Techniques for DTC-SVM-FTC (Simulation Results)

6.1. Introduction

Sensorless speed estimation is majorly advantageous when used in the traction motor control system of an EV. The estimation algorithm often provides increased reliability and improved noise immunity while reducing the cost, maintenance, machine drive size and hardware complexity [115]. Investigation of DTC-SVM-FTC with the inclusion of field-weakening control indicated that the system provides favourable torque, current and flux results across the speed range required for the EV system being investigated in this dissertation. As a result of the theoretical benefits provided by the inclusion of sensorless speed control, this chapter aims the assess the performance of two different speed estimation techniques integrated into the DTC-SVM-FTC mechanism, which contains field-weakening control (as simulated in Chapter 5). As in previous chapters, the DTC-SVM-FTC mechanism is simulated with a sampling frequency of 500 kHz and an SVM frequency of 20 kHz. The two sensorless speed estimation techniques investigated are an open-loop rotor flux-based estimation technique and a closed-loop rotor flux-based MRAS technique. The techniques are compared, with the suitability of each for use in the traction motor control system of an electric vehicle discussed.

6.2. Comparison of Open-Loop Rotor Flux-Based and Closed-Loop Rotor Flux-Based MRAS Speed Estimation

The structure of the DTC-SVM-FTC mechanism remains the same when sensorless speed control is added; however, a dynamic speed estimator is also included in the model, mitigating the requirement for rotor speed measurement. In addition, both of the sensorless DTC-SVM-FTC models developed in this dissertation include field-weakening control and the necessary torque limits, which ensure stable motor operation across the entire speed range required. In addition, a moving average filter was included at the output of both speed estimation algorithms, minimising ripple in the estimated speed. Figure 6-1 and Figure 6-2 show the motor speed in comparison to the reference or desired speed for the DTC-SVM-FTC mechanisms with open-loop sensorless speed control and closed-loop sensorless speed control, respectively. The torque load was adjusted to prevent torque limiting in the field-weakening region. Operating conditions that do not require torque limiting allow the speed response obtained with the implementation of sensorless control to be easily observed and analysed.

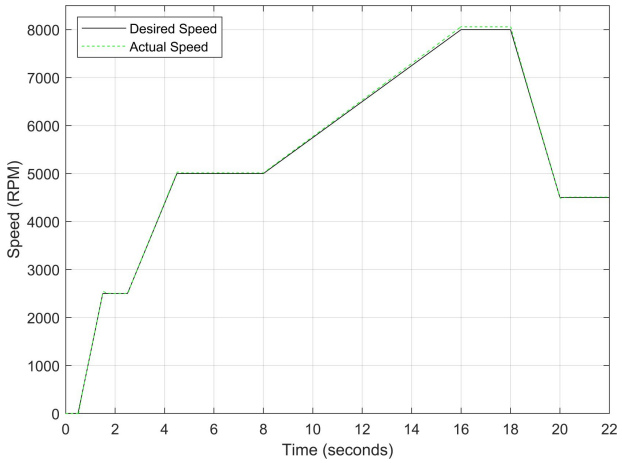

Figure 6-1: Open-loop sensorless DTC – Induction motor speed

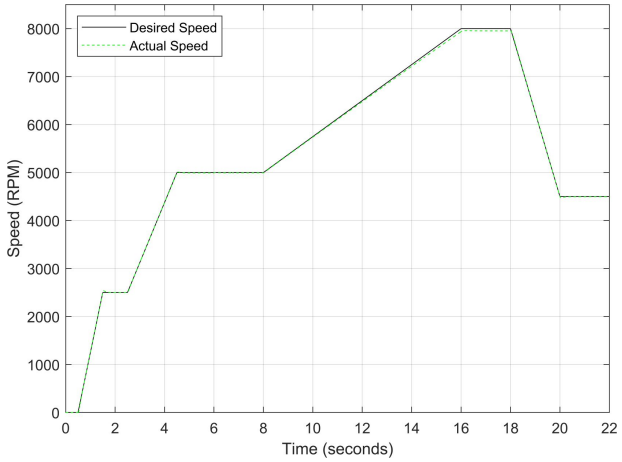

Figure 6-2: Closed-loop sensorless DTC – Induction motor speed

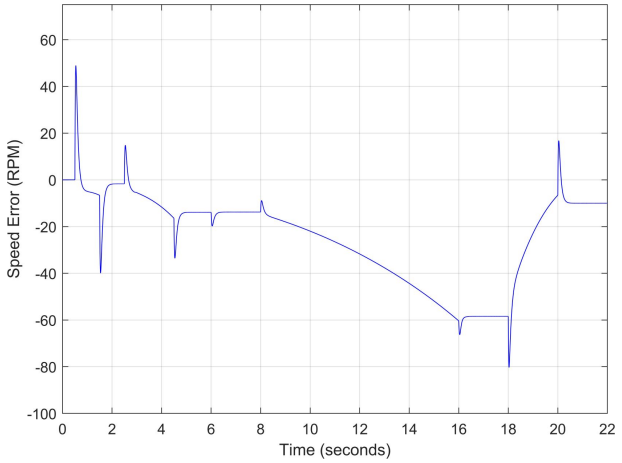

Figure 6-3: Open-loop sensorless DTC – Induction motor speed error

Figure 6-3 and Figure 6-4 show the absolute induction motor speed error when compared to the desired or reference speed for the DTC-SVM-FTC systems, which implement open-loop and closed-loop sensorless control, respectively. Both the speed response results (shown in Figure 6-1 and Figure 6-2), as well as the speed error results (shown in Figure 6-3 and Figure 6-4), indicate that the desired speed is correctly tracked throughout the drive cycle in both systems, with very little overshoot or undershoot. However, both mechanisms exhibit a small amount of steady-state

error, which increases with increasing speed. At a reference speed of 8000 rpm, both mechanisms show similar performance, with the open-loop speed estimation-based system exhibiting a steady-state error of approximately 0.735%, while a 0.595% steady-state error was observed from the closed-loop speed estimation-based system. These are the highest steady-state error percentages observed at any point during the drive cycle from either of the systems. As a result, it can be concluded that both sensorless speed control methods implemented have an accuracy of greater than 99.25% throughout the speed range simulated. This is a desired result, indicating that both implemented methods allow for accurate motor speed control. However, although both of the mechanisms have similar performance at a speed of 8000 rpm, the rotor flux-based MRAS system offers a significant reduction in the absolute speed error in most of the other operating conditions simulated. A comprehensive comparison of the absolute speed error observed from the systems is provided in Table 6-3 (found in section 6.3), which indicates the superior performance obtained from the rotor flux-based MRAS system.

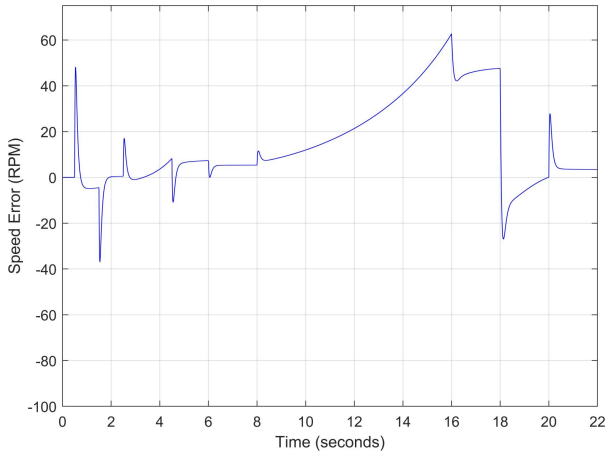

Figure 6-4: Closed-loop sensorless DTC – Induction motor speed error

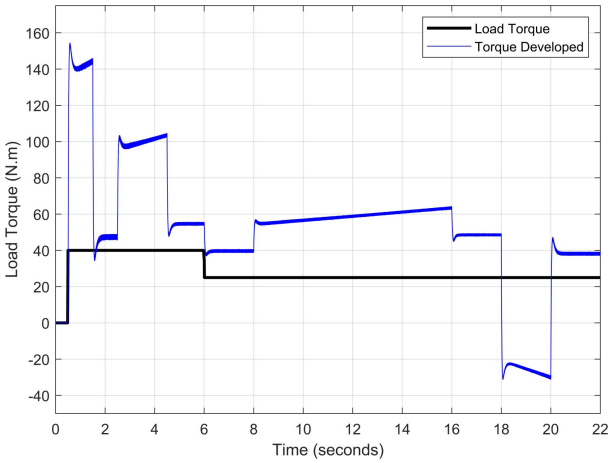

Figure 6-5: Open-loop sensorless DTC – Torque developed by induction motor (500 kHz)

The torque developed by the induction motor when open-loop and closed-loop sensorless DTC-SVM-FTC is utilised is shown in Figure 6-5 and Figure 6-6, respectively. The result indicates that the torque ripple is maintained within suitable levels in both mechanisms, providing comparable

results to that observed without the use of sensorless control. Torque limiting did not occur due to the reduced torque load utilised in the sensorless DTC-SVM-FTC simulations. It can be concluded that the implementation of the sensorless control schemes investigated does not have a significant impact on the torque ripple observed, with only a small increase in torque ripple seen in some operating conditions. A comprehensive comparison between the torque ripple observed in the DTC-SVM-FTC mechanisms with sensorless control implemented and the DTC-SVM-FTC mechanism without sensorless control is provided in Table 6-1 (found in section 6.3).

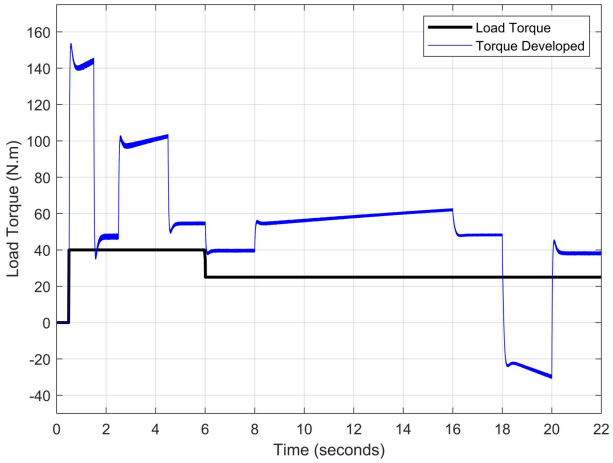

Figure 6-6: Closed-loop sensorless DTC – Torque developed by induction motor (500 kHz)

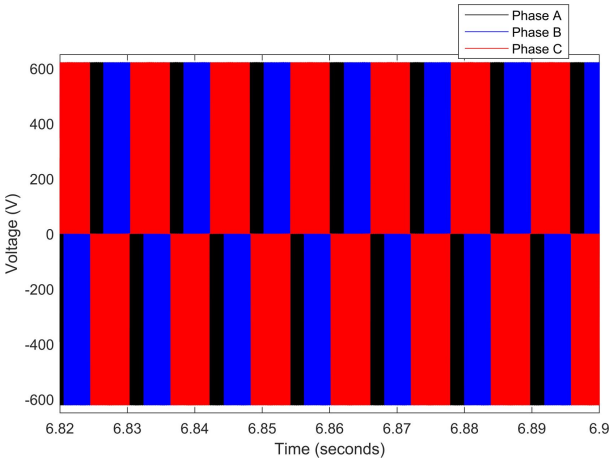

Figure 6-7: Open-loop sensorless DTC – Three-phase inverter voltage

The inverter voltages observed in the simulation are comparable to those observed in the DTC-SVM-FTC mechanism when sensorless control had not been implemented, with no notable variation in the results. The inverter voltages obtained from the DTC-SVM-FTC mechanisms with open-loop and closed-loop sensorless control are shown in Figure 6-7 and Figure 6-8, respectively. The voltages shown were measured when the motor was operating under steady-state conditions with a speed of 5000 rpm and a load torque of 25 N.m. Additionally, Figure 6-9 and Figure 6-10 show the inverter current supplied to the induction motor during the entire drive cycle for both mechanisms. Zoomed-in portions of both the Phase A and the three-phase steady-state inverter current supplied to the induction motor when the motor was operating at 5000 rpm

with a load torque of 25 N.m are also shown for both mechanisms. Both sensorless control-based systems produce sinusoidal current waveforms with low ripple, providing comparable results to those observed from the DTC-SVM-FTC system, which does not have sensorless control implemented.

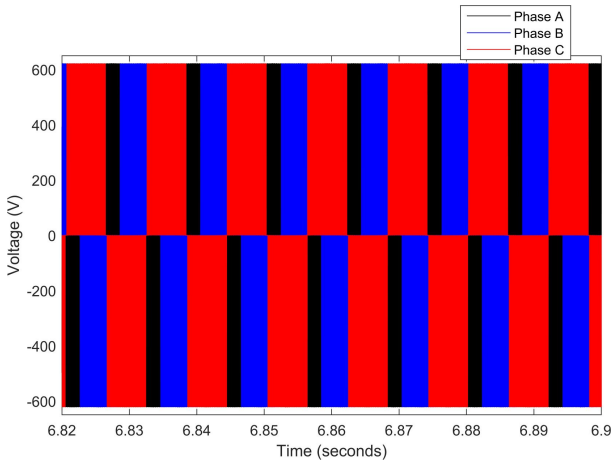

Figure 6-8: Closed-loop sensorless DTC – Three-phase inverter voltage

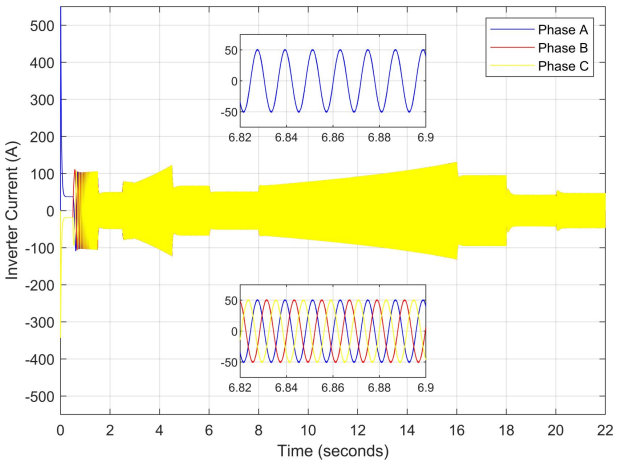

Figure 6-9: Open-loop sensorless DTC – Three-phase inverter current

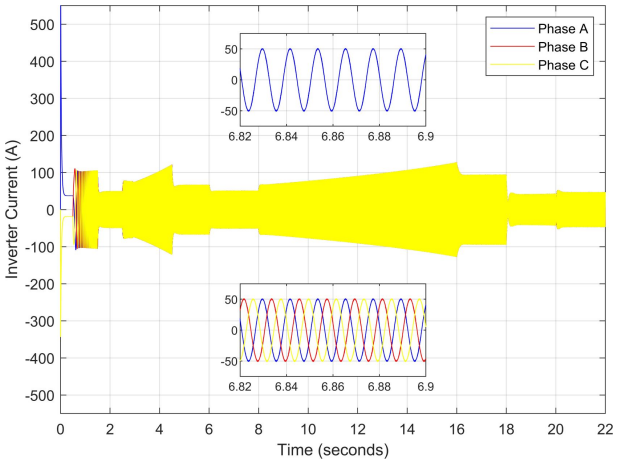

Figure 6-10: Closed-loop sensorless DTC – Three-phase inverter current

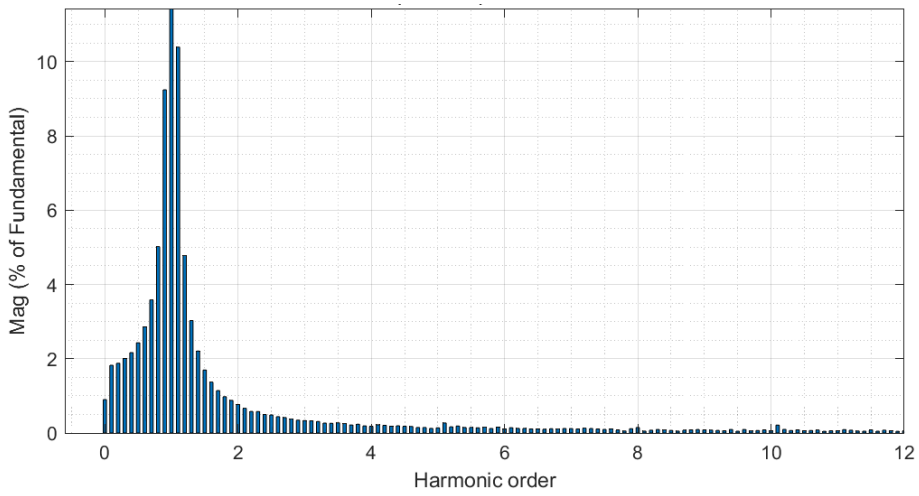

Figure 6-11: Open-loop sensorless DTC – FFT analysis of the current waveform (phase A)

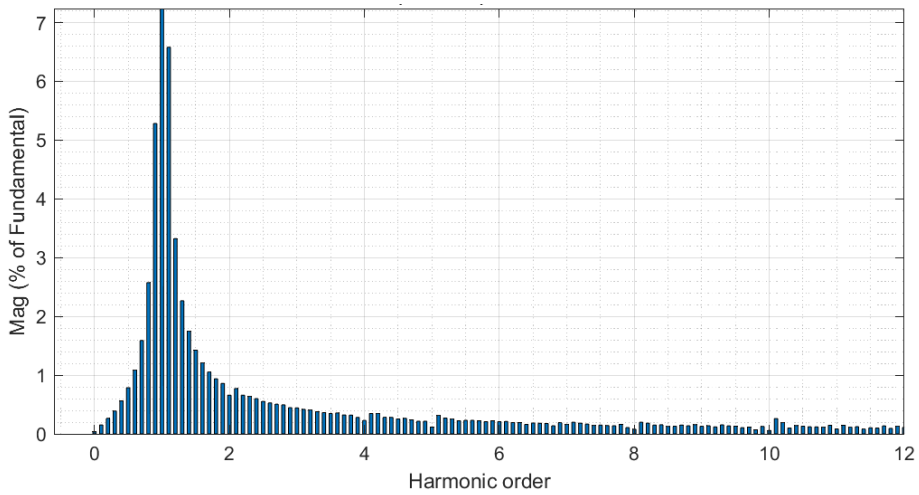

Figure 6-12: Closed-loop sensorless DTC – FFT analysis of the current waveform (phase A)

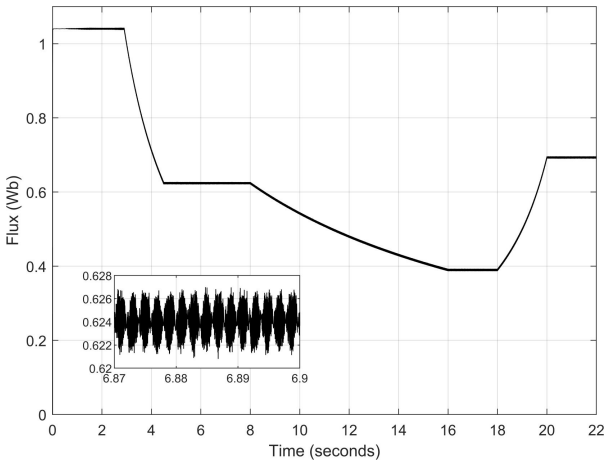

Figure 6-13: Open-loop sensorless DTC – Stator flux magnitude

The results of the FFT analysis performed on the current waveforms from the DTC-SVM-FTC mechanisms with open-loop and closed-loop sensorless control are shown in Figure 6-11 and Figure 6-12, respectively. As in the investigations carried out previously, the FFT analysis was carried out over a period of ten cycles. The analysis was performed while the motor was operating

under steady-state conditions, with a speed of 5000 rpm (fundamental frequency of ~83.33 Hz) and a load torque of 25 N.m, and indicated that the system which implemented a closed-loop rotor flux-based MRAS speed estimation system produced a THD of 8.95%, whereas the open-loop speed estimation based system produced a THD of 12.66%. As a result, the DTC-SVM-FTC system with closed-loop sensorless control provides an improved current waveform with a lower total harmonic distortion. However, it is also worth noting that both mechanisms produce suitable current waveforms with low 5^{th}, 7^{th}, $9^{th,}$ and 11^{th} harmonic components. Table 6-2 (found in section 6.3) provides additional analysis of the current ripple and THD results observed.

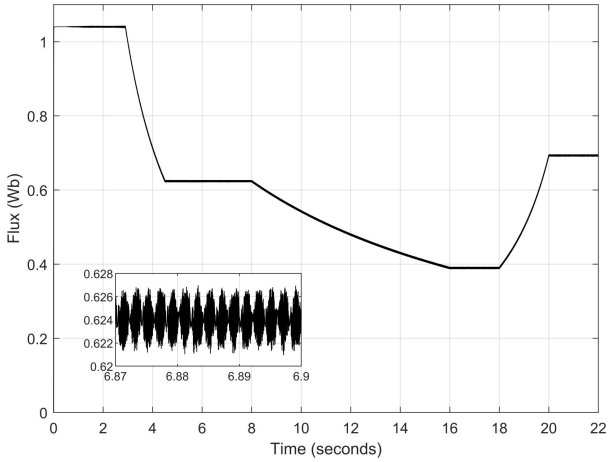

Figure 6-14: Closed-loop sensorless DTC – Stator flux magnitude

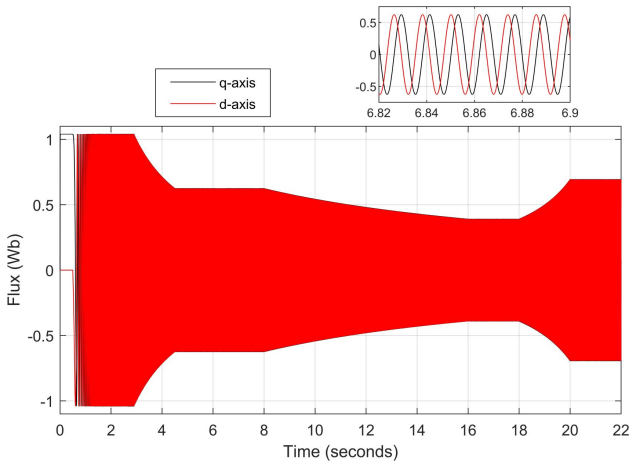

Figure 6-15: Open-loop sensorless DTC – Stator flux (d- and q-axis)

Figure 6-13 and Figure 6-14 show the stator flux magnitude during the entire drive cycle, observed from the DTC-SVM-FTC mechanisms, which implemented open-loop and closed-loop speed estimation mechanisms. Furthermore, Figure 6-15 and Figure 6-16 show the d- and q- axis components of the stator flux. Both sets of results also provide zoomed-in portions of the stator flux observed, measured when the motor was operating under steady-state conditions with a speed of 5000 rpm and a load torque of 25 N.m. From the graphs shown, it is clear that the stator flux is correctly varied, indicating the correct operation of the field-weakening control system when the motor is operating above the specified base speed. The sensorless speed control techniques

implemented result in comparable stator flux ripple when compared to the results obtained from the DTC-SVM-FTC mechanism, which did not implement sensorless speed control. Additional comparison of the stator flux ripple results obtained is given in Table 6-2 (found in section 6.3).

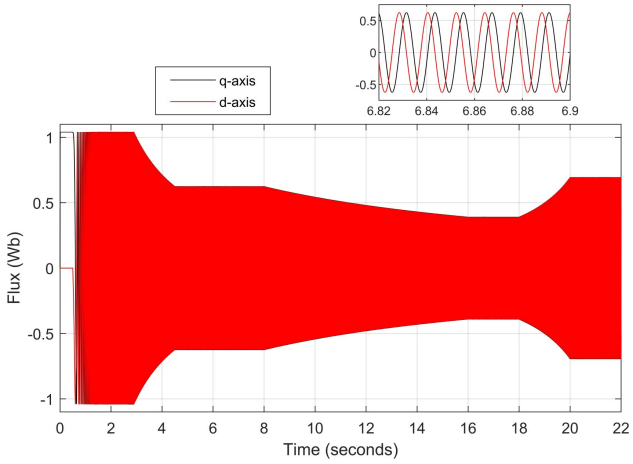

Figure 6-16: Closed-loop sensorless DTC – Stator flux (d- and q-axis)

6.3. Discussion

Investigation of both the open-loop rotor flux-based speed estimation mechanism and the closed-loop rotor flux-based MRAS speed estimation mechanism (integrated into the DTC-SVM-FTC system) provide favourable results, suitable for the traction motor control system of an electric vehicle.

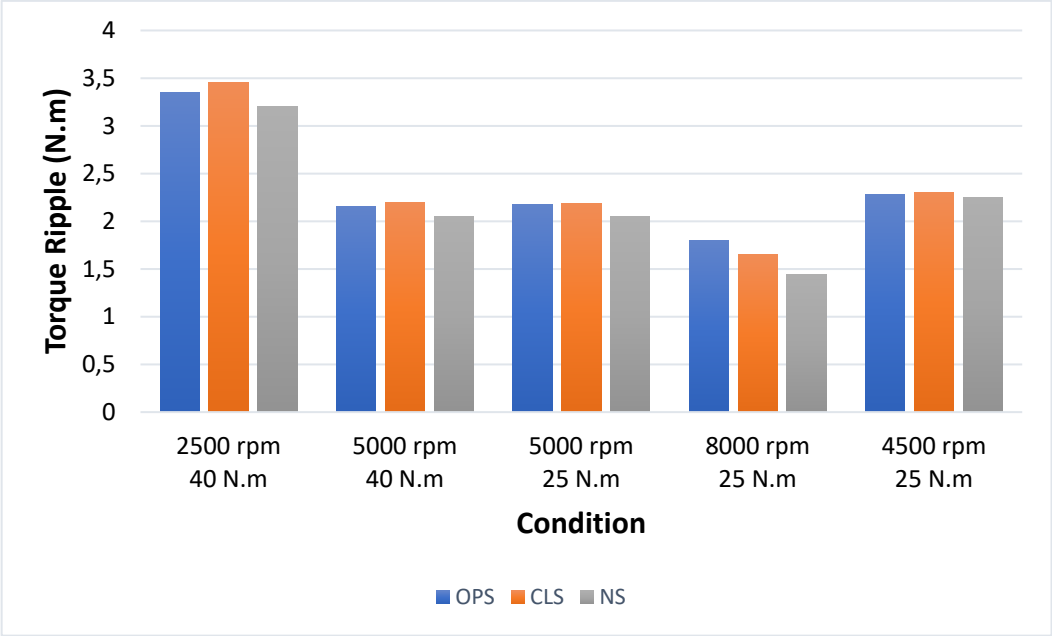

Figure 6-17: Comparison of sensorless control techniques in DTC-SVM-FTC (torque ripple)

Both speed estimation mechanisms investigated in this chapter were implemented with a moving average filter at the output of the estimation algorithm, minimising ripple in the estimated speed. It was observed that both DTC-SVM-FTC mechanisms with integrated speed estimation systems produced a similar torque response, responding well to step changes in the load torque and

exhibiting low steady-state torque ripple. A comparison of the steady-state torque ripple observed from both of the sensorless control-based systems, as well as the DTC-SVM-FTC mechanism without sensorless control, is provided in Table 6-1, with a graphical comparison provided in Figure 6-17. In Table 6-1 and Figure 6-17, the open-loop sensorless speed control-based mechanism is represented as OPS, the closed-loop sensorless speed control-based system as CLS and the DTC-SVM-FTC mechanism, which does not contain sensorless control as NS. This naming convention is maintained for the current, flux and absolute speed error results. The steady-state torque ripple results indicate that both of the sensorless control-based systems exhibit very similar steady-state torque ripple, with the ripple marginally increased from that seen in the DTC-SVM-FTC system, which does not include sensorless control. As a result, it is evident that the inclusion of the sensorless speed estimation mechanism did not have a major impact on the torque ripple observed from the system.

Table 6-1: Comparison of sensorless control techniques in DTC-SVM-FTC (torque ripple)

Operating Condition	Torque Ripple (N.m)		
	OPS	CLS	NS
2500 rpm, 40 N.m	3.35	3.45	3.20
5000 rpm, 40 N.m	2.16	2.20	2.05
5000 rpm, 25 N.m	2.18	2.19	2.05
8000 rpm, 25 N.m	1.80	1.65	1.44
4500 rpm, 25 N.m	2.28	2.30	2.25

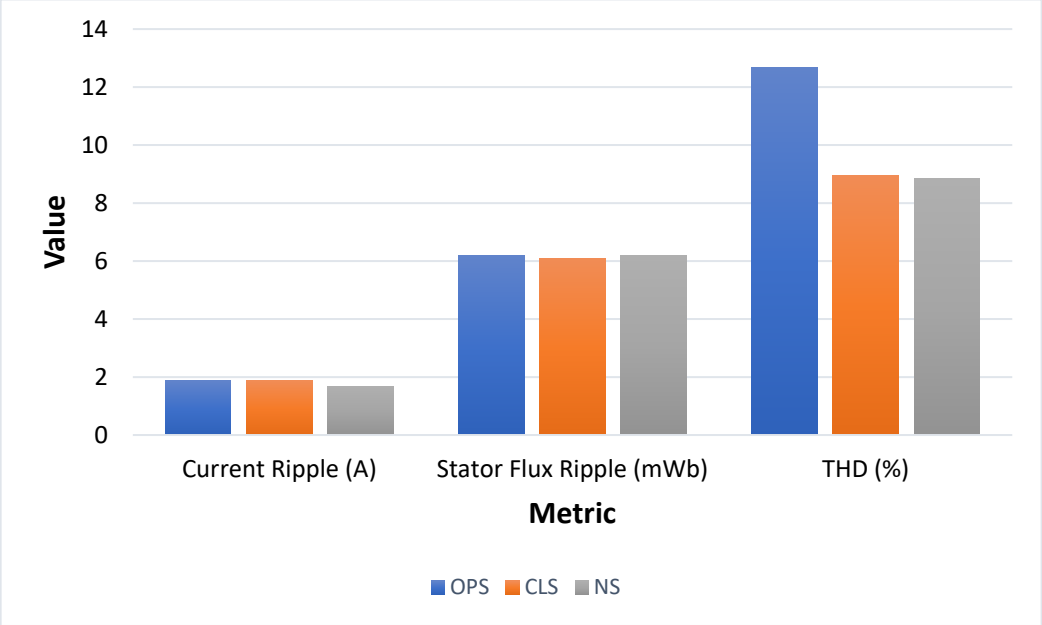

Figure 6-18: Comparison of sensorless control techniques in DTC-SVM-FTC (current and flux)

A comparison of important metrics obtained from the current and flux results observed from the DTC-SVM-FTC mechanism without sensorless speed control, the DTC-SVM-FTC mechanism

with open-loop speed estimation and the DTC-SVM-FTC mechanism with closed-loop speed estimation is shown in Table 6-2, with a graphical comparison given in Figure 6-18. All three of the models investigated provide very similar stator flux ripple results, with no notable differences between the systems. The DTC-SVM-FTC mechanism, which does not contain sensorless speed estimation, provides a slightly better current ripple, with both sensorless control-based mechanisms providing almost identical current ripple when compared with each other. However, the THD of the current ripple provides a notable result, as the open-loop sensorless control-based DTC-SVM-FTC mechanism has a notably higher THD than the other two mechanisms investigated.

Table 6-2: Comparison of sensorless control techniques in DTC-SVM-FTC (current and flux)

Condition: 5000 rpm with a torque load of 25 N.m			
Metric	**OPS**	**CLS**	**NS**
Current Ripple (A)	1.87	1.89	1.68
Stator Flux Ripple (mWb)	6.20	6.10	6.20
THD (%)	12.66	8.95	8.84

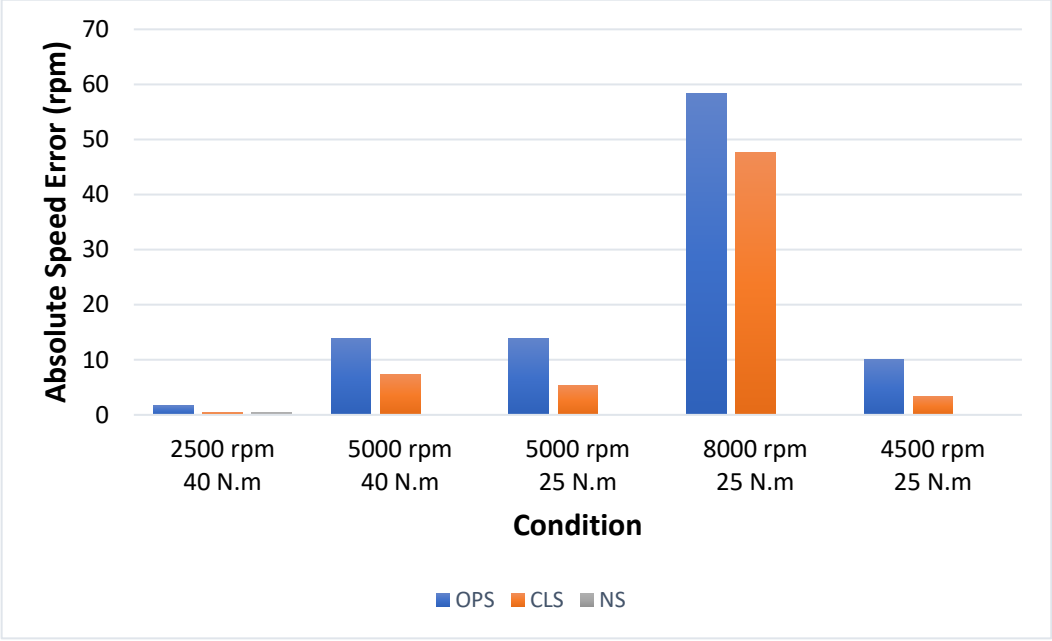

Figure 6-19: Comparison of sensorless control techniques in DTC-SVM-FTC (speed error)

Table 6-3 shows a comparison of the absolute speed error results that were obtained from the DTC-SVM-FTC mechanisms investigated in this chapter (DTC-SVM-FTC with open-loop and closed-loop speed estimation systems, as well as without sensorless speed control), with a graphical comparison shown in Figure 6-19. The speed error results provide the most notable comparison between the systems, as they indicate the significant improvement obtained when closed-loop speed estimation is used instead of an open-loop speed estimation system. Both speed

estimation mechanisms introduce speed error under all operating conditions assessed; however, the open-loop speed estimation system introduces significantly more speed error than the closed-loop system.

Table 6-3: Comparison of sensorless control techniques in DTC-SVM-FTC (speed error)

Operating Condition	Absolute Speed Error (rpm)		
	OPS	**CLS**	**NS**
2500 rpm, 40 N.m	1.70	0.50	0.37
5000 rpm, 40 N.m	13.90	7.30	0.00
5000 rpm, 25 N.m	13.78	5.35	0.00
8000 rpm, 25 N.m	58.44	47.62	0.00
4500 rpm, 25 N.m	10.00	3.40	0.00

6.4. Conclusion

Sensorless control is majorly advantageous in electric vehicle systems, enabling reduced hardware complexity, reduced cost, and less maintenance requirements. This chapter investigates the performance of DTC-SVM-FTC with two different sensorless speed control techniques, an open-loop rotor flux-based speed estimation system and a closed-loop rotor flux-based MRAS speed estimation system. The results obtained from both of the sensorless DTC-SVM-FTC mechanisms investigated indicate a significant advancement in the traction motor drive system implemented. Both of the implemented algorithms allowed for speed control with an accuracy of greater than 99.25% across the entire speed range required, with only a small increase in the torque ripple noted. However, although both methods perform adequately, it is evident that the closed-loop rotor flux-based MRAS estimation method provides significantly reduced steady-state speed error when compared with the open-loop estimation method investigated. The open-loop rotor flux-based estimation system requires an ideal integral and is sensitive to variation in the motor parameters, especially at low speeds. As a result, the closed-loop rotor flux-based MRAS system is included in the DTC-SVM-FTC mechanism investigated in chapter 7 of this dissertation.

7. Chapter 7 – DTC-SVM-FTC in Urban and Highway Driving Conditions (Simulation Results)

7.1. Introduction

Adequate investigation of a traction motor control system for an electric vehicle involves the assessment of the system with an adequate vehicle load in both urban and highway driving conditions. Until this stage, the investigation carried out has assessed various motor control techniques under numerous operating conditions, with a specific speed and load torque. However, this chapter aims to simulate the performance of the control mechanism while the traction motor is driving a realistic vehicle body in both urban and highway driving conditions. The simulated vehicle body is based on the specifications and parameters discussed in sections 3.3 and 3.4, with urban and highway drive cycles used to simulate realistic operating conditions encountered in everyday travelling. Drive cycles are utilised for the performance analysis of vehicles, as well as to assess vehicle characteristics. A drive cycle is able to simulate both road gradient and speed components; however, in most cases, one of the two variables remains constant while the other changes [17]. In the case of the simulations conducted in this chapter, the desired speed is the varied component.

A section of the New York City Cycle (NYCC) (adjusted for this case study) is utilised in order to simulate the performance of the vehicle in urban driving conditions, in which low-speed stop-and go- traffic conditions are present. The section simulated has a distance of 0.67 km, with a top speed of 42.5 km/h and an average speed of 16.08 km/h. Furthermore, a section of the Highway Fuel Economy Test (HWFET) drive cycle (adjusted for this case study) was utilised in order to simulate the performance of the vehicle in highway driving conditions. The HWFET cycle is the most commonly utilised test cycle for highway driving [17]. The section simulated has a distance of 3.56 km, with a top speed of 95 km/h and an average speed of 68.9 km/h. The DTC-SVM-FTC system used for control of the traction motor driving the vehicle body was simulated with a sampling frequency of 500 kHz, an SVM frequency of 20 kHz and included both field-weakening control and sensorless speed estimation (a closed-loop rotor flux-based MRAS speed estimator).

7.2. Urban Drive Cycle Simulation Results

Figure 7-1 shows the vehicle speed in comparison to the reference or desired speed, with Figure 7-2 showing the vehicle speed error. The results indicate that the speed is well tracked throughout the drive cycle simulated, with a very low speed error and negligible overshoot or undershoot. The section of the NYCC utilised tests operating conditions in which constant acceleration and deceleration are required, allowing the dynamic speed response of the system to be assessed. The

favourable results obtained indicate the correct operation and design of the PI controller-based speed control loop, as well as desired operation of the sensorless speed estimation system. An outlier, which indicates an unusually large speed error of ~2.2 km/h, can be observed in Figure 7-2, occurring just after 100 seconds in the drive cycle. This outlier occurs due to torque limiting, which enables stable operation of the induction motor throughout the drive cycle. Torque limiting is implemented as per Figure 3-4, with the torque limit at the operating condition (motor speed is lower than the rated speed of the motor) in question, based on the maximum overload factor chosen for the induction motor utilised (discussed in Table 3-4).

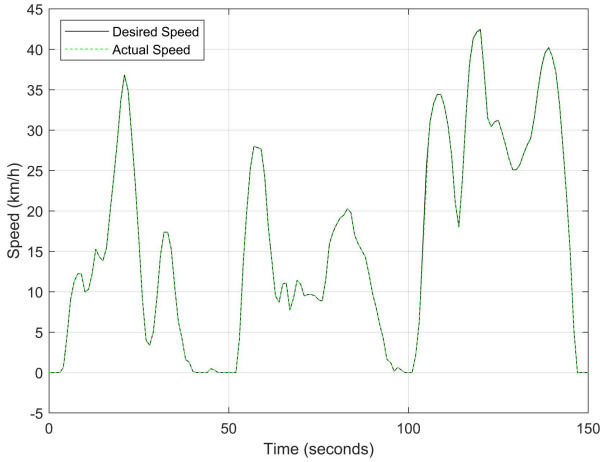

Figure 7-1: Urban drive cycle – Vehicle speed

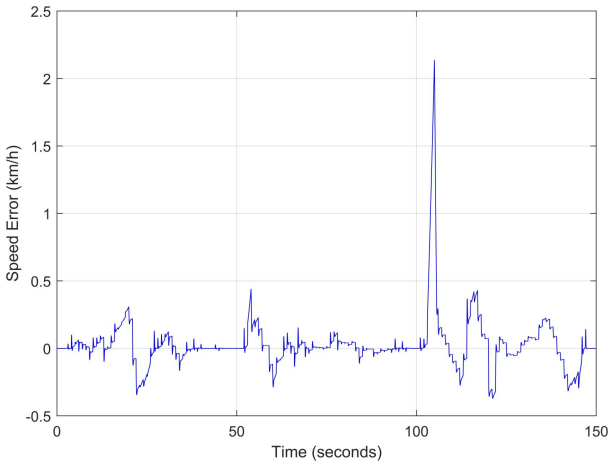

Figure 7-2: Urban drive cycle – Vehicle speed error

The torque limiting which occurs can be clearly observed in Figure 7-3, which shows the torque developed by the induction motor. This is a notable result, indicating that the developed torque does not exceed the torque limits of the motor, ensuring the electric vehicle drive system maintains stable operation throughout the drive cycle. The torque is supplied to the vehicle through a fixed gear system (discussed in more detail in section 3.4), and the developed torque result shows that the torque is continuously changing due to the continuous acceleration and deceleration required in the drive cycle. Furthermore, although the torque ripple varies across the dynamic operating conditions of the drive cycle, it can be observed that the torque ripple remains

within suitable levels under all operating conditions. The DTC-SVM-FTC system, which contains both field-weakening control and closed-loop speed estimation, responds well to all dynamic torque requirements, exhibiting a fast and stable response, translating to suitable vehicle rideability.

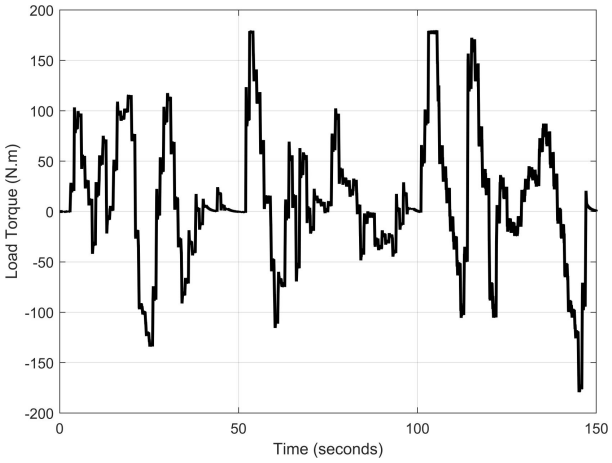

Figure 7-3: Urban drive cycle – Torque developed by induction motor

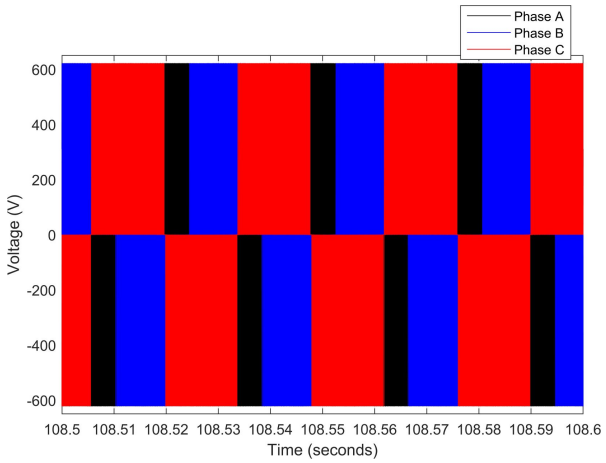

Figure 7-4: Urban drive cycle – Three-phase inverter voltage

Figure 7-4 shows the steady-state voltage generated from the two-level three-phase inverter supplying the traction motor during a short section of the drive cycle. The voltage observed was measured when the motor was operating under steady-state conditions with a speed of ~34.5 km/h. The sinusoidal voltage waveform produced is not of a high quality due to the nature of the inverter used; however, the voltage result observed is as expected. The inverter current supplied to the induction motor during the course of the urban drive cycle is shown in Figure 7-5. Furthermore, zoomed-in portions of the three-phase steady-state current are also shown in Figure 7-5, measured when the motor was operating at ~28 km/h (58.5 – 58.6 seconds) and ~34.5 km/h (108.5 – 108.6 seconds). As expected, the magnitude of the current waveform varies continuously and is proportional to the dynamic load introduced by the drive cycle. The zoomed-in sections of the waveform show that a desired sinusoidal current waveform is produced with a low current ripple. The quality of the current waveform is further assessed through the FFT analysis

undertaken, the result of which is shown in Figure 7-6. The analysis was performed when the motor was operating under steady-state conditions with a vehicle speed of ~34.5 km/h (fundamental frequency of ~35.519 Hz). The FFT analysis was carried out over a period of ten cycles (allowing for a resolution of ~3.55 Hz), with the THD found to be 5.52% under the operating condition assessed. High DC (0 Hz) and 2nd harmonic components were observed; however, the current waveform exhibited low 5th, 7th, 9th and 11th harmonic components. Overall, a high-quality current waveform with low ripple and an acceptable THD was produced.

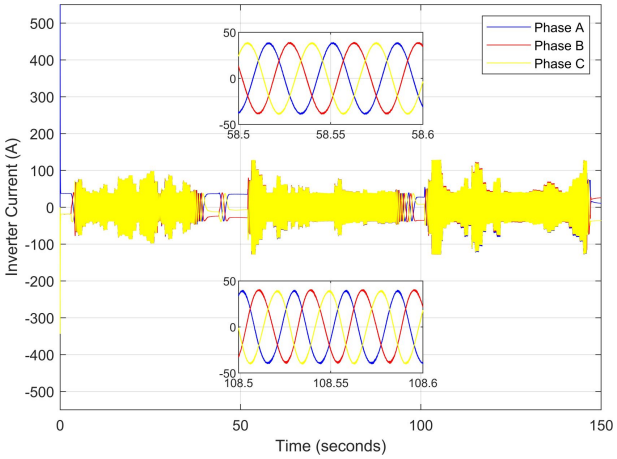

Figure 7-5: Urban drive cycle – Three-phase inverter current

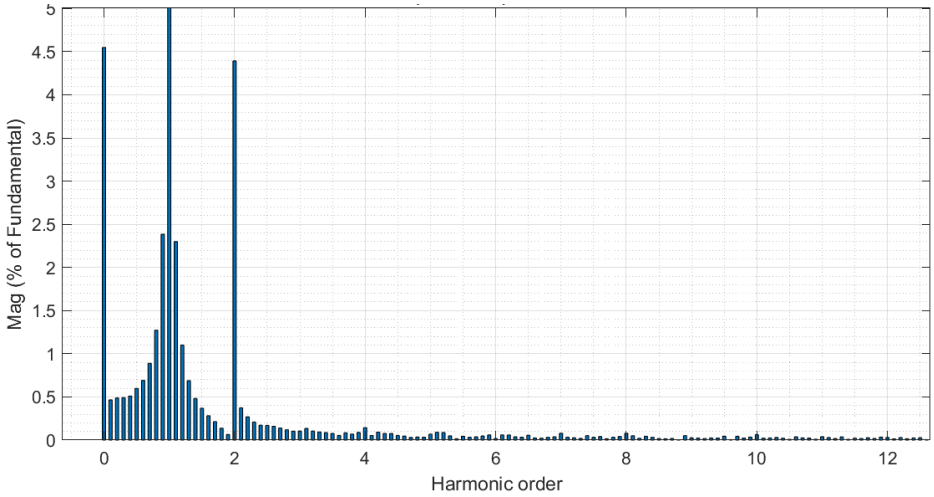

Figure 7-6: Urban drive cycle – FFT analysis of the current waveform (phase A)

The stator flux magnitude observed from the traction motor throughout the section of the NYCC used is shown in Figure 7-7, with Figure 7-8 showing the d- and q- axis components of the stator flux. Zoomed-in portions of the stator flux are also shown in both figures, measured when the motor was operating under steady-state conditions with a speed of ~34.5 km/h. The stator flux magnitude is maintained constant at the stator flux reference of 1.04 Wb, indicating that the stator flux is correctly controlled throughout the drive cycle. Due to the nature of the urban drive cycle used, the stator flux magnitude is not varied as the reference speed does not require the rated speed of the motor to be exceeded. Figure 7-7 indicates that the stator flux ripple does vary during

different sections of the drive cycle; however, the ripple is maintained within suitable limits under all operating conditions. This is evident from the zoomed-in portion of the stator flux magnitude shown, while the zoomed-in portion of the d- and q- axis components of the stator flux indicate that the stator flux components have an expected sinusoidal waveform with the correct amplitude of 1.04 Wb.

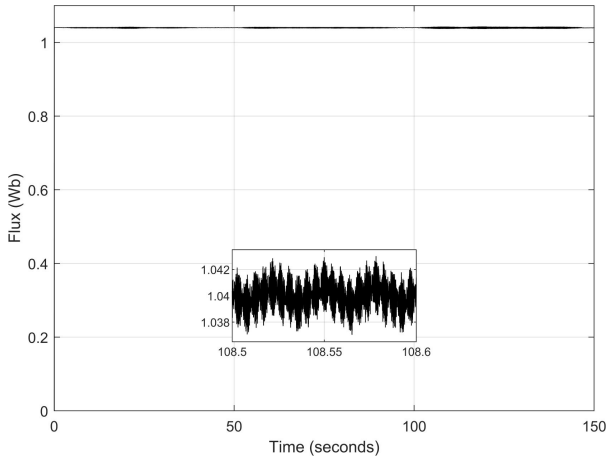

Figure 7-7: Urban drive cycle – Stator flux magnitude

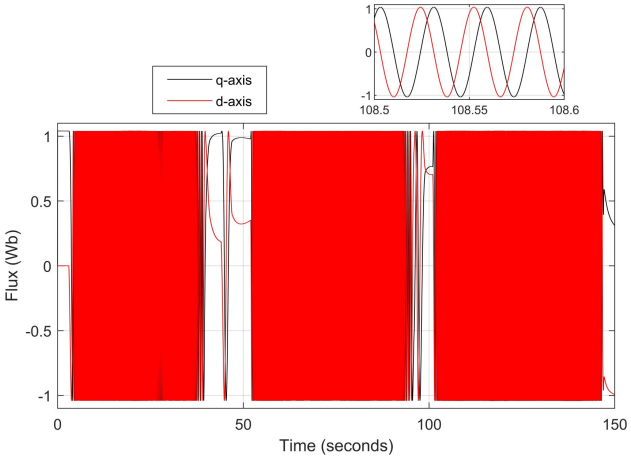

Figure 7-8: Urban drive cycle – Stator flux (d- and q-axis)

7.3. Highway Drive Cycle Simulation Results

The sections of the HWFET cycle utilised simulate the high-speed performance of the drive system, as opposed to the low-speed stop- and go- traffic conditions simulated in the NYCC. This can be observed in Figure 7-9, which shows the vehicle speed in comparison to the reference or desired speed, while Figure 7-10 shows the vehicle speed error. The results indicate that the desired speed is correctly tracked and that vehicle performance is satisfactory in the highway speed conditions tested. As with the urban drive cycle, the satisfactory performance indicates adequate design of the speed control loop and desired operation of the sensorless speed estimation system. A more consistent speed error can be noticed at the higher speeds simulated with the HWFET cycle when compared with the NYCC. This is due to the speed error generated from the

closed-loop rotor flux-based MRAS speed estimator utilised. However, the speed error shown in Figure 7-10 is maintained within acceptable limits throughout the HWFET cycle, with the absolute speed error not exceeding 0.6 km/h at any point during the cycle.

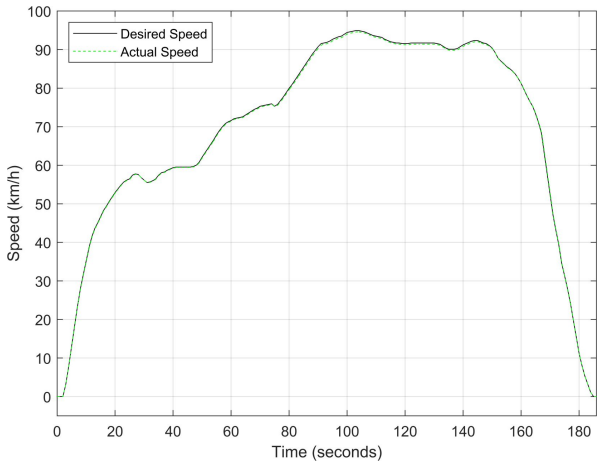

Figure 7-9: Highway drive cycle – Vehicle speed

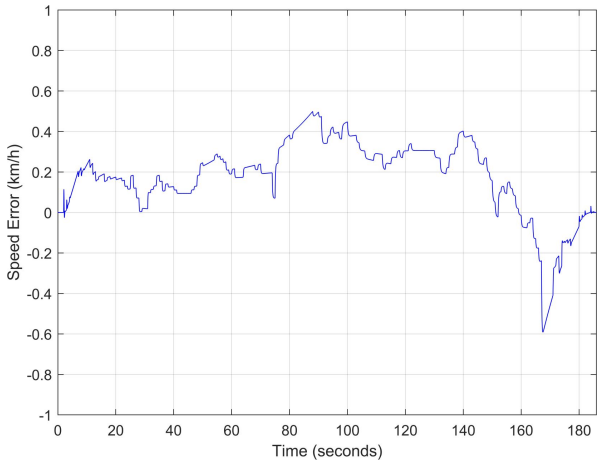

Figure 7-10: Highway drive cycle – Vehicle speed error

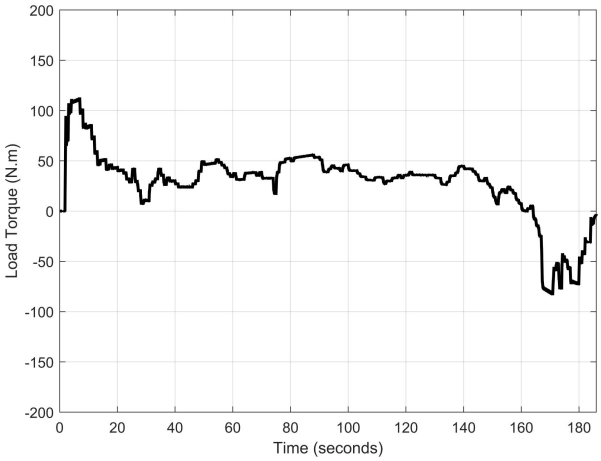

Figure 7-11: Highway drive cycle – Torque developed by induction motor

The torque developed by the traction motor, which is supplied to the vehicle through a fixed gear system, is shown in Figure 7-11. Due to the nature of the highway drive cycle, the torque developed is more consistent than the result observed from the NYCC simulation. Notably, the

developed torque does not exceed the torque limits of the motor, ensuring the traction drive system maintains stable operation throughout the drive cycle. Furthermore, the traction motor exhibits a largely steady torque ripple, which remains within suitable levels under all operating conditions. Overall, the torque result obtained from the DTC-SVM-FTC system, assessed with the HWFET cycle, indicates that the control system provides desired vehicle rideability, exhibiting a fast and stable torque response with acceptable torque ripple.

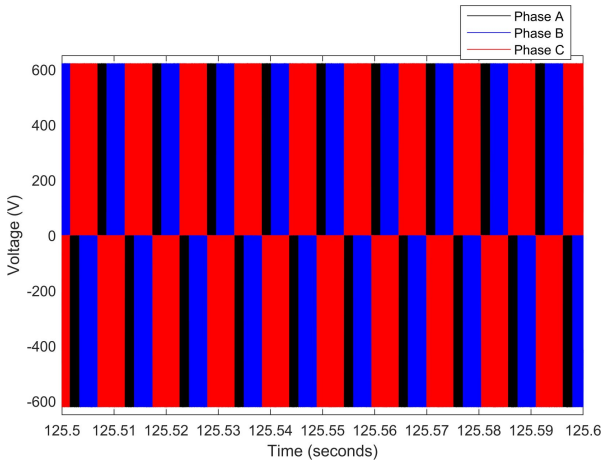

Figure 7-12: Highway drive cycle – Three-phase inverter voltage

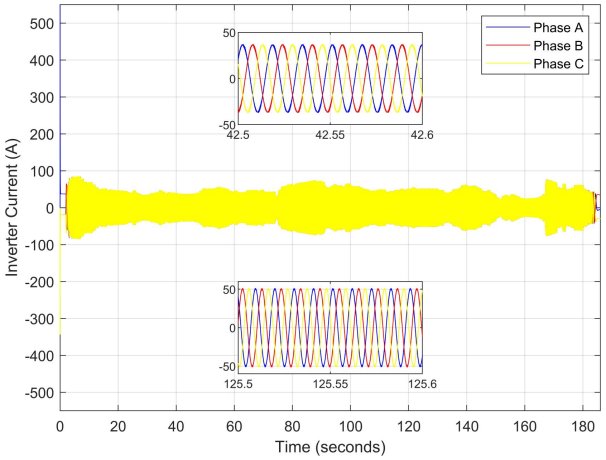

Figure 7-13: Highway drive cycle – Three-phase inverter current

The inverter voltage observed from the simulation of DTC-SVM-FTC with the HWFET cycle is given in Figure 7-12 and shows an expected result. The voltage was measured when the motor was operating under steady-state conditions with a vehicle speed of ~92 km/h. Furthermore, Figure 7-13 shows the inverter current supplied to the motor during the course of the drive cycle, with zoomed-in portions of the three-phase waveform also shown when the motor was operating under steady-state conditions with speeds of ~59.5 km/h (42.5 – 42.6 seconds) and ~92 km/h (125.5 – 125.6 seconds). Both zoomed-in sections of the waveform indicate that a desired sinusoidal current waveform with a low current ripple is achieved. The quality of the current waveform is further assessed through FFT analysis carried out on a portion of the waveform, the result of which is shown in Figure 7-14. The FFT analysis, measured over a period of ten cycles,

was also performed when the motor was operating under steady-state conditions with a speed of ~92 km/h (fundamental frequency of ~94.605 Hz). The THD under these operating conditions was 8.06%, with low 7^{th}, 9^{th} and 11^{th} harmonic components observed. A slightly higher 5^{th} harmonic component can be noticed; however, it is still within acceptable limits. In general, it can be concluded that a favourable result was achieved, as a high-quality current waveform with a low current ripple was observed.

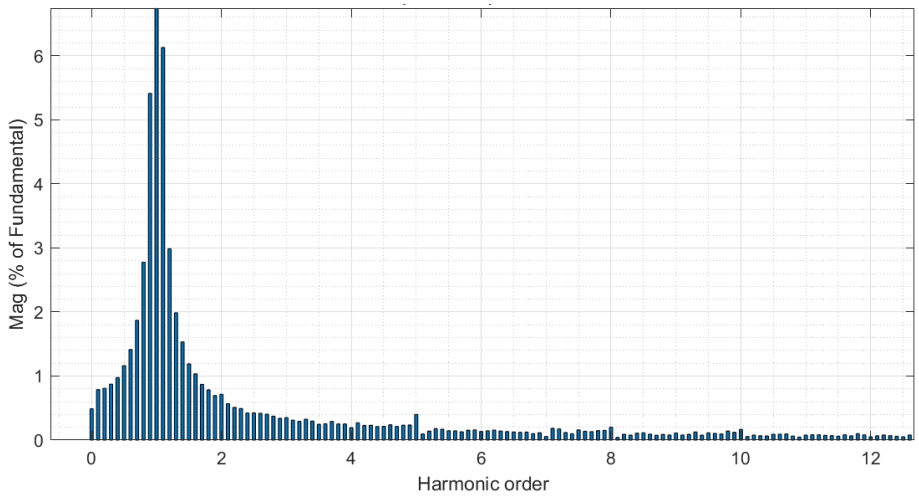

Figure 7-14: Highway drive cycle – FFT analysis of the current waveform (phase A)

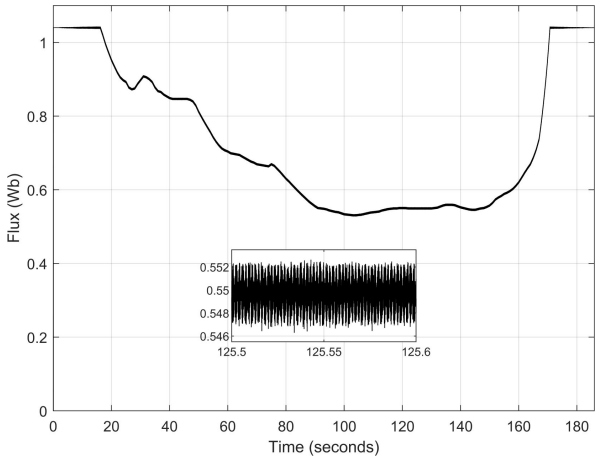

Figure 7-15: Highway drive cycle – Stator flux magnitude

Figure 7-15 and Figure 7-16 show the stator flux magnitude as well as the d- and q- axis components of the stator flux, respectively, observed from the DTC-SVM-FTC mechanism simulated with the HWFET cycle. Both results also show zoomed-in portions of the stator flux, observed when the motor was operating under steady-state conditions with a speed of ~92 km/h. The speed requirements of the highway drive cycle mean that field-weakening control is required, and Figure 7-15 indicates that the stator flux magnitude is correctly varied. The variation can also be observed in the changing amplitude shown in Figure 7-16. Furthermore, the control system exhibits a low and largely consistent stator flux ripple throughout the drive cycle, with the ripple maintained within suitable levels under all operating conditions. This is further confirmed by the

zoomed-in portion of the stator flux magnitude, while the zoomed-in section of the d- and q- axis components indicates a desired sinusoidal waveform.

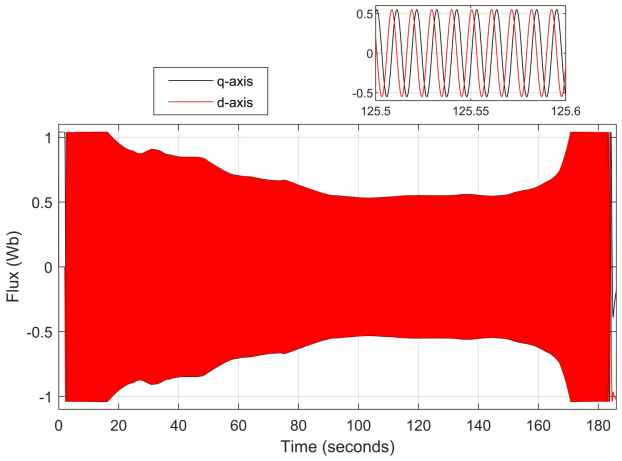

Figure 7-16: Highway drive cycle – Stator flux (d- and q-axis)

7.4. Discussion

The DTC-SVM-FTC model simulated in this chapter contains field-weakening control and a sensorless speed estimator (closed-loop rotor flux-based MRAS estimator), assessing three major components in the traction motor drive system. Furthermore, the use of a simulated vehicle body, which simulates realistic loading of the motor, ensured that the complete mechanism was adequately assessed to determine its suitability for use in EV systems. Notably, the complete mechanism performs favourably when assessed using both urban and highway driving conditions. The mechanism ensures that the vehicle correctly tracks the desired speed defined by the input drive cycle while exhibiting low-speed error in urban and highway conditions. While some speed error is noticed (and is more prevalent at higher speeds), the speed error is maintained within suitable limits. Furthermore, adequate vehicle rideability is obtained, as the control system provides a fast and stable torque response with low torque ripple, responding appropriately to the dynamic torque requirements in both drive cycles utilised. The control mechanism ensures stable operation of the motor drive system as the motor torque limits are not exceeded.

A desired sinusoidal inverter current waveform is observed, with a low current ripple and an acceptable THD (found using FFT analysis over a period of ten cycles). Furthermore, acceptable 5^{th}, 7^{th}, 9^{th} and 11^{th} harmonic components were observed when the mechanism was simulated in both urban and highway driving conditions. The stator flux is correctly controlled, maintaining a constant value when the motor is operating below the specified rated speed, and varying correctly when the motor is operating in the field-weakening region. Additionally, the stator flux ripple is maintained within acceptable limits throughout the speed range simulated in both drive cycles. The correct operation of the field-weakening control structure is also confirmed by the favourable dynamic speed response obtained in the HWFET cycle. Although it is not simulated in this

dissertation, it is also important to note that the DTC-SVM-FTC mechanism investigated enables the implementation of regenerative braking. The research scholars in [38] suggest that approximately 50% of all braking energy can be recovered through regenerative braking, adding significant benefit to the system. In addition, the research scholars in [22] indicate that simulations of the vehicles tested in their study showed that the implementation of regenerative braking enables the energy consumption of the drive train to be reduced in excess of 20%.

7.5. Conclusion

Assessment of a complete traction motor control mechanism (which includes field-weakening control and sensorless speed estimation) utilising realistic vehicle loads in urban and highway driving conditions is extremely useful when determining whether the control mechanism is suitable for electric vehicle applications. As a result, this chapter aims to investigate the performance of the complete DTC-SVM-FTC system with a simulated vehicle load. The model was simulated using the New York City Cycle for assessment of the urban driving performance and the Highway Fuel Economy Test drive cycle for assessment of the highway driving performance. The results observed under the various conditions assessed indicate that the DTC-SVM-FTC mechanism evaluated is suitable for use in the traction motor system of an electric vehicle. The system exhibits favourable speed tracking performance with adequate vehicle rideability and stable operation ensured. Furthermore, desired inverter current and stator flux waveforms are achieved, with the system also suitable for the implementation of regenerative braking. Ultimately, positive performance was obtained from the system while ensuring that the algorithm complexity and required computation time were reduced compared to some of the other control options available.

8. Chapter 8 – Conclusion and Recommendations

8.1. Conclusion

In its present state, the transport sector faces significant and growing issues due to its dependence on internal combustion engine vehicles. As the sector is necessary for the operation of many cities and business sectors around the world, the importance of reducing urban air pollution and greenhouse gases generated from vehicular transport cannot be overstated. Battery electric vehicles provide a promising solution, offering zero tailpipe emissions and high Tank to Wheel efficiencies. As a result of the benefits that battery electric vehicles provide, the field of battery electric vehicles warrants extensive investigation and continual development. Consequently, this dissertation aims to present an investigation of traction motor control systems applicable for use in an electric vehicle drivetrain.

As induction and permanent magnet synchronous motors are best suited for the urban and highway driving requirements experienced by electric vehicle systems, the traction motor drive system requires the implementation of direct torque control or field-oriented control for adequate control of the traction motor. A comprehensive review of literature found that recent research works have aimed to further develop these control techniques, focusing on efficiency improvements and ensuring parameter insensitivity in the control models. It was also found that various developments have been made to conventional direct torque control to improve the torque, current and stator flux performance of the control models. Furthermore, a tabulated comparison of electric motors which can be utilised in electric vehicle drivetrains led to the selection of an induction motor for use in this study due to its controllability, reliability, and cost.

A multi-stage simulation-based assessment of motor control techniques was necessary to answer the research questions proposed for this dissertation. An initial assessment of five motor control techniques (conventional direct torque and field-oriented control, space vector modulation-based direct torque control using closed-loop torque control, space vector modulation-based direct torque control using closed-loop torque and flux control, and fuzzy logic-based direct torque control) carried out indicated that both direct torque control and field-oriented control are suitable for application in the traction motor drive system of an electric vehicle. The initial assessment, which utilised the torque, current and stator flux results as main comparison metrics, indicated that fuzzy logic-based direct torque control and space vector modulation-based direct torque control using closed-loop torque and flux control were promising solutions for further investigation. However, it should be noted that field-oriented control also presented a suitable solution despite not being investigated further in this dissertation.

The second stage of the simulation-based assessment aimed to provide a comparison of the two selected solutions across the entire speed range required through the implementation of field-weakening control. The initial stage of the assessment utilised a simple drive cycle, for which the speed range simulated fell within the rated speed of the induction motor. The inclusion of field-weakening control in both control systems (fuzzy logic-based direct torque control and space vector modulation-based direct torque control using both closed-loop torque and flux control) was found to enable favourable dynamic speed responses across the entire speed range of the vehicle while ensuring stable traction motor operation through a correctly implemented torque limiting structure. Furthermore, it was observed that fuzzy logic-based direct torque control provides the most favourable results for application in electric vehicle systems. However, space vector modulation-based direct torque control using closed-loop torque and flux control also provides suitable results, while maintaining a simpler algorithm complexity and lower computation time in comparison to fuzzy logic-based direct torque control. The algorithm complexity and computation time are important metrics as direct torque control is a largely online control structure by nature. Resultantly, space vector modulation-based direct torque control using closed-loop torque and flux control was selected for further extension and investigation.

Sensorless speed estimation provides significant benefits when utilised in the traction motor control system of an electric vehicle. As a result, the third stage of the simulation-based assessment simulated two sensorless speed estimation techniques, integrated into space vector modulation-based direct torque control using closed-loop torque and flux control. Simulation of open-loop rotor flux-based speed estimation and a closed-loop model reference adaptive system speed estimator (also developed using the rotor flux) indicated that the closed-loop speed estimator provided more favourable results, reducing the steady-state speed error noted from the control mechanism.

With the formation of a complete traction motor control mechanism, which incorporates field-weakening control and closed-loop sensorless speed estimation, the final stage of the simulation-based study assesses the performance of the control structure in realistic urban and highway driving conditions with a simulated vehicle body. Simulations conducted utilising sections of the New York City Cycle and Highway Fuel Economy Test cycle indicate that the system exhibits favourable speed tracking performance with adequate vehicle rideability and stable operation ensured. Furthermore, desired inverter current and stator flux waveforms are achieved, with the system also suitable for the implementation of regenerative braking. Ultimately, positive performance was obtained from the system while ensuring that the algorithm complexity and required computation time were reduced compared to some of the other control options available.

8.2. Recommendations for Future Work

The following are suggestions to extend the research work conducted in this dissertation:

1. Induction motors provide a suitable option for the traction motor in electric vehicle systems, providing favourable controllability, reliability, and cost. However, permanent magnet synchronous motors are also a very attractive option, with increased efficiency and power density metrics. As a result, it is recommended that the study be extended to include a simulation-based comparison between the motors.
2. While an extensive investigation of various motor control techniques was carried out, other motor control techniques were not assessed, which may also provide suitable performance for electric vehicle applications. Such techniques include model predictive-based direct torque control, sliding mode-based direct torque control and artificial neural network-based direct torque control. It is suggested that investigation of these additional control techniques be included, ultimately extending the comprehensiveness of the study.
3. Current research works in the field of traction motor control systems for electric vehicle applications have placed a large emphasis on efficiency improvement. As a result, it is recommended that the research work be extended to include efficiency improvement through variation of the DC link voltage (which supplies the inverter) and the stator flux. The development of novel techniques in this area could allow for significant improvement in the traction motor drive system and the driving range of the electric vehicle.
4. The scope of the research work conducted in this dissertation is focused predominantly on the traction motor control system of an electric vehicle. Therefore, although certain essential parts of the electric vehicle drivetrain are simulated, the performance of the entire drivetrain is not investigated. It is suggested that the study undertaken be extended to include the battery and DC-DC bidirectional converter systems. Such an extension of the study enables performance analysis of the traction motor control mechanism in a more complete drivetrain system.

References

[1] A. Emadi, Y. Joo Lee and K. Rajashekara, "Power Electronics and Motor Drives in Electric, Hybrid Electric, and Plug-In Hybrid Electric Vehicles," *IEEE Transactions on Industrial Electronics*, vol. 55, no. 6, pp. 2237-2245, Jun. 2008.

[2] J. Larminie and J. Lowry, Electric Vehicle Technology Explained, West Sussex, United Kingdom: John Wiley & Sons, Ltd., 2012.

[3] X. Liu, H. Chen, Z. Zhao and A. Belahcen, "Research on the Performances and Parameters of Interior PMSM Used for Electric Vehicles," *IEEE Transactions on Industrial Electronics*, vol. 63, no. 6, pp. 3533-3544, Jun. 2016.

[4] M. Ehsani, Y. Gao, S. E. Gay and A. Emadi, Modern Electric, Hybrid Electric, and Fuel Cell Vehicles, 1st ed. Florida, United States of America: CRC Press, 2005.

[5] U. Chinthakunta, K. Prabhakar, A. Singh and P. Kumar, "Direct torque control induction motor drive performance evaluation based on torque error status selection methods," *IET Electrical Systems in Transportation*, vol. 9, no. 3, pp. 113-127, May 2019.

[6] D. Ranawat and P. R. Prasas, "Review on Electric Vehicles with perspective of Battery Management System," in *2018 Third International Conference on Electrical, Electronics, Communication, Computer Technologies and Optimization Techniques (ICEECCOT)*, Msyuru, India, 2018, pp. 1539-1544.

[7] H. Suvak and K. Ersan, "Simulation of A Photovoltaic Panel Supported Real Time Hybrid Electric Vehicle," in *2014 International Conference on Renewable Energy Research and Application (ICRERA)*, Milwaukee, United States of America, 2014, pp.529-534.

[8] J. J. Makrygiorgou and A. T. Alexandridis, "Power Electronic Control Design for Stable EV Motor and Battery Operation during a Route," *Energies*, vol. 12, no. 1990, pp. 1-21, May. 2019.

[9] E. A. Grunditz and T. Thiringer, "Performance Analysis of Current BEVs Based on a Comprehensive Review of Specifications," *IEEE Transactions on Transportation Electrification*, vol. 2, no. 3, pp. 270-289, Sep. 2016.

[10] K. T. Chau, Electric Vehicle Machines and Drives Design: Analysis and Application, Singapore: John Wiley & Sons and IEEE Press, 2015.

[11] K. Rajashekara, "Present Status and Future Trends in Electric Vehicle Propulsion Technologies," *IEEE Journal of Emerging and Selected Topics in Power Electronics*, vol. 1, no. 1, pp. 3-10, Mar. 2013.

[12] L. Shao, A. E. H. Karci, D. Tavernini, A. Sorniotti and M. Cheng, “Design Approaches and Control Strategies for Energy-Efficient Electric Machines for Electric Vehicles - A Review,” *IEEE Access,* vol. 8, no. 1, pp. 116900-116913, May 2020.

[13] J. Yong, V. Ramachandaramurthy, K. Tan and N. Mithilananthan, “A review on the state-of-the-art technologies of electric vehicle, its impacts and prospects,” *Renewable and Sustainable Energy Reviews,* vol. 49, no. 1, pp. 365-385, May. 2015.

[14] F. Un-Noor, S. Padmanaban, L. Mihet-Popa, M. N. Mollah and E. Hossain, “A Comprehensive Study of Key Electric Vehicle (EV) Components, Technologies, Challenges, Impacts, and Future Direction of Development,” *Energies,* vol. 10, no. 1217, pp. 1-84, Aug. 2017.

[15] K. Prabhakar, C. Reddy, P. Kumar and A. Singh, “A New Reference Flux Linkage Selection Technique for Efficiency Improvement of Direct Torque Controlled IM Drive,” *IEEE Journal of Emerging and Selected Topics in Power Electronics,* vol. 8, no. 4, pp. 3751-3762, Dec. 2020.

[16] J. de Santiago, H. Bernhoff, B. Ekergård, S. Eriksson, S. Ferhatovic, R. Waters and M. Leijon, “Electrical Motor Drivelines in Commercial All-Electric Vehicles: A Review,” *IEEE Transactions on Vehicular Technology,* vol. 61, no. 2, pp. 475-484, Feb. 2012.

[17] A. Karki, S. Phuyal, D. Tuladhar, S. Basnet and B. P. Shrestha, “Status of Pure Electric Vehicle Power Train Technology and Future Prospects,” *Applied System Innovation,* vol. 3, no. 35, pp. 1-28, Aug. 2020.

[18] L. Chapman, “Transport and climate change: a review,” *Journal of Transport Geography,* vol. 15, no. 5, pp. 354-367, Sep. 2007.

[19] I. Aharon and A. Kuperman, “Topological Overview of Powertrains for Battery-Powered Vehicles With Range Extenders,” *IEEE Transactions on Power Electronics,* vol. 26, no. 3, pp. 868-876, Mar. 2011.

[20] A. Albatayneh, M. Assaf, D. Alterman and M. Jaradat, “Comparison of the Overall Energy Efficiency for Internal Combustion Engine Vehicles and Electric Vehicles,” *Environmental and Climate Technologies,* vol. 24, no. 1, pp. 669-680, Oct. 2020.

[21] J. Hayes, R. de Oliveira, S. Vaughan and M. Egan, “Simplified electric vehicle power train models and range estimation,” in *2011 IEEE Vehicle Power and Propulsion Conference,* Chicago, United States of America, 2011, pp. 1-5.

[22] S. Van Sterkenburg, E. Rietveld, F. Rieck, B. Veenhuizen and H. Bosma, “Analysis of regenerative braking efficiency — A case study of two electric vehicles operating in the Rotterdam area,” in *2011 IEEE Vehicle Power and Propulsion Conference,* Chicago, United States of America, 2011, pp. 1-6.

[23] W. J. Smith, “Can EV (electric vehicles) address Ireland’s CO2 emissions from transport?,” *Energy*, vol. 35, no. 12, pp. 4514-4521, Dec. 2010.

[24] S. Campanari, G. Manzolini and F. Garcia de la Iglesia, “Energy analysis of electric vehicles using batteries or fuel cells through well-to-wheel driving cycle simulations,” *Journal of Power Sources*, vol. 186, no. 2, pp. 464-477, Jan. 2009.

[25] M. L. De Klerk and A. K. Saha, “A Comprehensive Review of Advanced Traction Motor Control Techniques Suitable for Electric Vehicle Applications,” *IEEE Access*, vol. 9, no. 1, pp. 125080-125108, Sep. 2021.

[26] M. L. De Klerk and A. K. Saha, “Performance analysis of DTC-SVM in a complete traction motor control mechanism for a battery electric vehicle,” *Heliyon*, vol. 8, no. 4, pp. 1-16, Apr. 2022.

[27] T. Sutikno, N. R. Idris and A. Jidin, “A review of direct torque control of induction motors for sustainable reliability and energy efficient drives,” *Renewable and Sustainable Energy Reviews*, vol. 32, no. 1, pp. 548-558, Feb. 2014.

[28] C. Reza, D. Islam and S. Mekhilef, “A review of reliable and energy efficient direct torque controlled induction motor drives,” *Renewable and Sustainable Energy Reviews*, vol. 37, no. 1, pp. 919-932, Jun. 2014.

[29] N. El Ouanjli, A. Derouich, A. El Ghzizal, S. Motahhir, A. Chebabhi, Y. El Mourabit and M. Taoussi, “Modern improvement techniques of direct torque control for induction motor drives - a review,” *Protection and Control of Modern Power Systems*, vol. 4, no. 11, pp. 1-12, May 2019.

[30] L. Zhang, Z. Zhang, Z. Wang, J. Deng and D. Dorrell, “Chassis Coordinated Control for Full X-by-Wire Vehicles-A Review,” *Chinese Journal of Mechanical Engineering*, vol. 34, no. 42, pp. 1-25, May. 2021.

[31] X. Ding, Z. Wang and L. Zhang, “Hybrid Control-Based Acceleration Slip Regulation for Four-Wheel-Independently-Actuated Electric Vehicles,” *IEEE Transactions on Transportation Electrification.*

[32] L. Zhai, T. Sun and J. Wang, “Electronic Stability Control Based on Motor Driving and Braking Torque Distribution for a Four In-Wheel Motor Drive Electric Vehicle,” *IEEE Transactions on Vehicular Technology*, vol. 65, no. 6, pp. 4726-4739, Jun. 2016.

[33] J. Liu, Z. Wang, L. Zhang and P. Walker, “Sideslip angle estimation of ground vehicles: a comparative study,” *IET Control Theory & Applications*, vol. 14, no. 20, pp. 3490-3505, Nov. 2020.

[34] A. Sarker, H. Shen, M. Rahman, M. Chowdhury, K. Dey, F. Li, Y. Wang and H. Narman, "A Review of Sensing and Communication, Human Factors, and Controller Aspects for Information-Aware Connected and Automated Vehicles," *IEEE Transactions on Intelligent Transportation Systems,* vol. 21, no. 1, pp. 7-29, Jan. 2020.

[35] S. De Pinto, C. Chatzikomis, A. Sorniotti and G. Mantriota, "Comparison of Traction Controllers for Electric Vehicles With On-Board Drivetrains," *IEEE Transactions on Vehicular Technology,* vol. 66, no. 8, pp. 6715-6727, Aug. 2017.

[36] C. Xu, J. Niu and F. Pei, "Design and simulation of the power-train system for an electric vehicle," in *2011 2nd International Conference on Artificial Intelligence, Management Science and Electronic Commerce (AIMSEC)*, Henan, China, 2011, pp. 3868-3871.

[37] S. J. Rind, M. Jamil and A. Amjad, "Electric Motors and Speed Sensorless Control for Electric and Hybrid Electric Vehicles: A Review," in *2018 53rd International Universities Power Engineering Conference (UPEC)*, Glasgow, Scotland, 2018, pp. 1-6.

[38] S. Tie and C. Tan, "A review of energy sources and energy management system in electric vehicles," *Renewable and Sustainable Energy Reviews,* vol. 20, no. 1, pp. 82-102, Dec. 2012.

[39] M. Lelie, T. Braun, M. Knips, H. Nordmann, F. Ringbeck, H. Zappen and D. Sauer, "Battery Management System Hardware Concepts: An Overview," *Applied Sciences,* vol. 8, no. 534, pp. 1-27, Mar. 2018.

[40] S. Habib, M. Khan, F. Abbas, L. Sang, M. Shahid and H. Tang, "A Comprehensive Study of Implemented International Standards, Technical Challenges, Impacts and Prospects for Electric Vehicles," *IEEE Access,* vol. 6, no. 1, pp. 13866-13890, Feb. 2018.

[41] L. Bokopane, K. Kanzumba and H. Vermaak, "Is the South African Electrical Infrastructure Ready for Electric Vehicles?," in *2019 Open Innovations (OI)*, Cape Town, South Africa, 2019, pp. 127-131.

[42] S. Manias, Power Electronics and Motor Drive Systems, Oxford, United Kingdom: Elsevier, 2017.

[43] A. Emadi, Handbook of Automotive Power Electronics and Motor Drives, Boca Raton, Florida, United States of America: Taylor & Francis Group, 2005.

[44] A. Tarkiainen and J. Pyrhönen, "Maximum modulation index of direct torque control with circular flux trajectory," *IET Power Electronics,* vol. 5, no. 4, pp. 477-484, Apr. 2012.

[45] M. Rashid, Power Electronics Handbook: Fourth Edition, Oxford, United Kingdom: Elsevier, 2018.

[46] G. Buja and M. Kazmierkowski, “Direct Torque Control of PWM Inverter-Fed AC Motors - A Survey,” *IEEE Transactions on Industrial Electronics*, vol. 51, no. 4, pp. 744-757, Aug. 2004.

[47] M. Vafaie, B. Dehkordi, P. Moallem and A. Kiyoumarsi, “Improving the Steady-State and Transient-State Performances of PMSM Through an Advanced Deadbeat Direct Torque and Flux Control System,” *IEEE Transactions on Power Electronics*, vol. 32, no. 4, pp. 2964-2975, Apr. 2017.

[48] X. Wang, Z. Wang, Z. Xu, M. Cheng and Y. Hu, “Optimization of Torque Tracking Performance for Direct-Torque-Controlled PMSM Drives With Composite Torque Regulator,” *IEEE Transactions on Industrial Electronics*, vol. 67, no. 12, pp. 10095-10108, Dec. 2020.

[49] A. Ammar, A. Benakcha and A. Bourek, “Closed loop torque SVM-DTC based on robust super twisting speed controller for induction motor drive with efficiency optimization,” *International Journal of Hydrogen Energy*, vol. 42, no. 28, pp. 17940-17952, Jul. 2017.

[50] M. Żelechowski, *Space Vector Modulated – Direct Torque Controlled (DTC – SVM) Inverter – Fed Induction Motor Drive*, Warsaw, 2005.

[51] X. Wu, W. Huang, X. Lin, W. Jiang, Y. Zhao and S. Zhu, “Direct Torque Control for Induction Motors Based on Minimum Voltage Vector Error,” *IEEE Transactions on Industrial Electronics*, vol. 68, no. 5, pp. 3794-3804, May 2021.

[52] J.-K. Kang and S.-K. Sul, “New Direct Torque Control of Induction Motor for Minimum Torque Ripple and Constant Switching Frequency,” *IEEE Transactions on Industry Applications*, vol. 35, no. 5, pp. 1076-1082, Sep./Oct. 1999.

[53] M. Nikzad, B. Asaei and S. Ahmadi, “Discrete Duty-Cycle-Control Method for Direct Torque Control of Induction Motor Drives With Model Predictive Solution,” *IEEE Transactions on Power Electronics*, vol. 33, no. 3, pp. 2317-2329, Mar. 2018.

[54] Z. Koutsogiannis, G. Adamidis and A. Fyntanakis, “Direct torque control using space vector modulation and dynamic performance of the drive, via a fuzzy logic controller for speed regulation,” in *2007 European Conference on Power Electronics and Applications*, Aalborg, Denmark, 2007, pp. 1-10.

[55] X. Wu, G. Tan, M. Liu and H. Li, “Electrically Excited Synchronous Motor Three-Level DTC_SVM Control Based on Novel Flux Observer,” in *2010 International Conference on Electrical and Control Engineering*, Wuhan, China, 2010, pp. 3689-3692.

[56] Y.-S. Lai and J.-H. Chen, “A New Approach to Direct Torque Control of Induction Motor Drives for Constant Inverter Switching Frequency and Torque Ripple Reduction,” *IEEE Transactions on Energy Conversion*, vol. 16, no. 3, pp. 220-227, Sep. 2001.

[57] M. Zelechowski, M. Kazmierkowski and F. Blaabjerg, “Controller design for direct torque controlled space vector modulated (DTC-SVM) induction motor drives,” in *Proceedings of the IEEE International Symposium on Industrial Electronics, 2005. ISIE 2005*, Dubrovnik, Croatia, 2005, pp. 951-956.

[58] E. Ozkop and H. Okumus, “Direct torque control of induction motor using space vector modulation (SVM-DTC),” in *2008 12th International Middle-East Power System Conference*, Aswan, Egypt, 2008, pp. 368-372.

[59] H. Sudheer, S. Fodad and B. Sarvesh, “Implementation of SVM-DTC of induction motor using FPGA,” in *2017 IEEE International Conference on Power, Control, Signals and Instrumentation Engineering (ICPCSI)*, Chennai, India, 2017, pp. 2319-2323.

[60] M. Lazim, M. Al-khishali and A. Al-Shawi, “Space Vector Modulation Direct Torque Speed Control Of Induction Motor,” *Procedia Computer Science*, vol. 5, no. 1, pp. 505-512, 2011.

[61] S. Gdaim, A. Mtibaa and M. F. Mimouni, “Design and Experimental Implementation of DTC of an Induction Machine Based on Fuzzy Logic Control on FPGA,” *IEEE Transactions on Fuzzy Systems*, vol. 23, no. 3, pp. 644-655, Jun. 2015.

[62] Y. Bchir, S. Gdaim and A. Mtibaa, “Application of fuzzy logic in DTC scheme using XSG,” in *14th International Conference on Sciences and Techniques of Automatic Control & Computer Engineering - STA'2013*, Sousse, Tunisia, 2013, pp. 191-196.

[63] N. El Ouanjli, S. Motahhir, A. Derouich, A. El Ghzizal, A. Chebabhi and M. Taoussi, “Improved DTC strategy of doubly fed induction motor using fuzzy logic controller,” *Energy Reports*, vol. 5, no. 1, pp. 271-279, Nov. 2019.

[64] C. Venugopal, “Fuzzy logic based DTC for speed control of Matrix Converter fed Induction Motor,” in *2010 IEEE International Conference on Power and Energy*, Kuala Lumpur, Malaysia, 2010, pp. 753-758.

[65] N. El Ouanjli, A. Derouich, A. El Ghzizal, A. Chebabhi, M. Taoussi and B. Bossoufi, “Direct Torque Control Strategy Based on Fuzzy Logic Controller for a Doubly Fed Induction Motor,” *IOP Conf. Series: Earth and Environmental Science*, vol. 161, no. 1, pp. 1-8, 2018.

[66] A. Tlemcani, O. Bouchhida, K. Benmansour, D. Boudana and M. Boucherit, “Direct Torque Control Strategy (DTC) Based on Fuzzy Logic Controller for a Permanent Magnet Synchronous Machine Drive,” *Journal of Electrical Engineering & Technology*, vol. 4, no. 1, pp. 66-78, Jan. 2009.

[67] S. Mir, M. Elbuluk and D. Zinger, “Fuzzy Implementation of Direct Self Control of Induction Machines,” *IEEE Trans. on Industry App.*, vol. 30, no. 3, pp. 729-735, May/Jun. 1994.

[68] J. Pujar and S. Kodad, “Direct Torque Fuzzy Control of an AC Drive,” in *2009 International Conference on Advances in Computing, Control, and Telecommunication Technologies*, Kerala, India, 2009, pp. 275-277.

[69] D. Jinlian and T. Li, “Improvement of Direct Torque Control Low-speed Performance by Using Fuzzy Logic Technique,” in *2006 International Conference on Mechatronics and Automation*, Luoyang, China, 2006, pp. 2481-2485.

[70] M. Hafeez, M. Uddin and R. Rebeiro, “FLC based hysteresis band adaptation to optimize torque and stator flux ripples of a DTC based IM drive,” in *2010 IEEE Electrical Power & Energy Conference*, Halifax, Canada, 2010, pp. 1-5.

[71] M. Uddin and M. Hafeez, “FLC-Based DTC Scheme to Improve the Dynamic Performance of an IM Drive,” *IEEE Trans. on Industry Applications,* vol. 48, no. 2, pp. 823-831, Mar./Apr. 2012.

[72] C. Lascu, I. Boldea and F. Blaabjerg, “Direct Torque Control of Sensorless Induction Motor Drives: A Sliding-Mode Approach,” *IEEE Transactions on Industry Applications,* vol. 40, no. 2, pp. 582-590, Mar./Apr. 2004.

[73] D. Sun, “Sliding Mode Direct Torque Control for Induction Motor with Robust Stator Flux Observer,” in *2010 International Conference on Intelligent Computation Technology and Automation*, Changsha, China, 2010, pp. 348-351.

[74] M. Dal, “Sensorless sliding mode direct torque control (DTC) of induction motor,” in *Proceedings of the IEEE International Symposium on Industrial Electronics, 2005. ISIE 2005*, Dubrovnik, Croatia, 2005, pp. 911-916.

[75] T. Vamsee Kiran and J. Amarnath, “A sliding mode controller based DTC of 3 level NPC inverter fed induction motor employing space vector modulation technique,” in *IEEE-International Conference On Advances In Engineering, Science And Management (ICAESM -2012)*, Nagapattinam, India, 2012, pp. 372-377.

[76] S.-K. Lin and C.-H. Fang, “Sliding-mode direct torque control of an induction motor,” in *IECON'01. 27th Annual Conference of the IEEE Industrial Electronics Society*, Denver, CO, USA, 2001, pp. 2171-2177.

[77] A. Benchaib, A. Rachid and E. Audrezet, “Sliding Mode Input-Output Linearization and Field Orientation for Real-Time Control of Induction Motors,” *IEEE Transactions on Power Electronics*, vol. 14, no. 1, pp. 3-13, Jan. 1999.

[78] T. Ahammad, A. Beig and K. Al-Hosani, “Sliding mode based DTC of three-level inverter fed induction motor using switching vector table,” in *2013 9th Asian Control Conference (ASCC)*, Istanbul, Turkey, 2013, pp. 1-6.

[79] A. Naassani, E. Monmasson and J.-P. Louis, “Synthesis of Direct Torque and Rotor Flux Control Algorithms by Means of Sliding-Mode Theory,” *IEEE Transactions on Industrial Electronics*, vol. 52, no. 3, pp. 785-798, Jun. 2005.

[80] L. Meng and X. Yang, “Comparative analysis of direct torque control and DTC based on sliding mode control for PMSM drive,” in *2017 29th Chinese Control And Decision Conference (CCDC)*, Chongqing, China, 2017, pp. 736-741.

[81] S. Mondal, J. Pinto and B. Bose, “A Neural-Network-Based Space-Vector PWM Controller for a Three-Level Voltage-Fed Inverter Induction Motor Drive,” *IEEE Transactions on Industry Applications*, vol. 38, no. 3, pp. 660-669, May/Jun. 2002.

[82] S. Jadhav, J. Kirankumar and B. Chaudhari, “ANN based intelligent control of Induction Motor drive with Space Vector Modulated DTC,” in *2012 IEEE International Conference on Power Electronics, Drives and Energy Systems (PEDES)*, Bengaluru, India, 2012, pp. 1-6.

[83] M. Zegai, M. Bendjebbar, K. Belhadri, M. Doumbia, B. Hamane and P. Koumba, “Direct torque control of Induction Motor based on artificial neural networks speed control using MRAS and neural PID controller,” in *2015 IEEE Electrical Power and Energy Conference (EPEC)*, London, England, 2015, pp. 320-325.

[84] Y. Sayouti, A. Abbou, M. Akherraz and H. Mahmoudi, “Real-time DSP implementation of DTC neural network-based for induction motor drive,” in *5th IET International Conference on Power Electronics, Machines and Drives (PEMD 2010)*, Brighton, United Kingdom, 2010, pp. 1-5.

[85] R. Kumar, R. Gupta, S. Bhangale and H. Gothwal, “Artificial neural network based direct Torque Control of Induction Motor drives,” in *2007 IET-UK International Conference on Information and Communication Technology in Electrical Sciences (ICTES 2007)*, Chennai, India, 2007, pp. 361-367.

[86] X. Wu and L. Huang, “Direct torque control of three-level inverter using neural networks as switching vector selector,” in *Conference Record of the 2001 IEEE Industry Applications Conference. 36th IAS Annual Meeting*, Chicago, Illinois, USA, 2001, pp. 939-944.

[87] E. Camacho, “Constrained Generalized Predictive Control,” *IEEE Transactions on Automatic Control*, vol. 38, no. 2, pp. 327-332, Feb. 1993.

[88] T. Geyer, G. Papafotiou and M. Morari, “Model Predictive Direct Torque Control—Part I: Concept, Algorithm, and Analysis,” *IEEE Transactions on Industrial Electronics,* vol. 56, no. 6, pp. 1894-1905, Jun. 2009.

[89] G. Papafotiou, J. Kley, K. Papadopoulos, P. Bohren and M. Morari, “Model Predictive Direct Torque Control—Part II: Implementation and Experimental Evaluation,” *IEEE Transactions on Industrial Electronics,* vol. 56, no. 6, pp. 1906-1915, Jun. 2009.

[90] Y. Zeinaly, T. Geyer and B. Egardt, “Trajectory extension methods for model predictive direct torque control,” in *2011 Twenty-Sixth Annual IEEE Applied Power Electronics Conference and Exposition (APEC)*, Fort Worth, Texas, United States of America, 2011, pp. 1667-1674.

[91] F. Wang, Z. Zhang, X. Mei, J. Rodriguez and R. Kennel, “Advanced Control Strategies of Induction Machine: Field Oriented Control, Direct Torque Control and Model Predictive Control,” *Energies,* vol. 11, no. 1, pp. 1-13, Jan. 2018.

[92] K. Prabhakar, U. Chinthakunta, A. Singh and P. Kumar, “Efficiency and performance analysis of DTC-based IM drivetrain using variable dc-link voltage for electric vehicle applications,” *IET Electrical Systems in Transportation,* vol. 8, no. 3, pp. 205-214, Apr. 2018.

[93] S. Odhano, R. Bojoi, A. Boglietti, S. Rosu and G. Griva, “Maximum Efficiency per Torque Direct Flux Vector Control of Induction Motor Drives,” *IEEE Transactions on Industry Applications,* vol. 51, no. 6, pp. 4415-4424, Nov./Dec. 2015.

[94] Y. Wang, T. Ito and R. Lorenz, “Loss Manipulation Capabilities of Deadbeat Direct Torque and Flux Control Induction Machine Drives,” *IEEE Transactions on Industry Applications,* vol. 51, no. 6, pp. 4554-4566, Nov./Dec. 2015.

[95] A. Haddoun, M. Benbouzid, D. Diallo, R. Abdessemed, J. Ghouili and K. Srairi, “A Loss-Minimization DTC Scheme for EV Induction Motors,” *IEEE Transactions on Vehicular Technology,* vol. 56, no. 1, pp. 81-88, Jan. 2007.

[96] G. Munoz-Hernandez, G. Mino-Aguilar, J. Guerrero-Castellanos and E. Peralta-Sanchez, “Fractional Order PI-Based Control Applied to the Traction System of an Electric Vehicle (EV),” *Applied Sciences,* vol. 10, no. 364, pp. 1-23, Jan. 2020.

[97] K. Prabhakar, C. Reddy, A. Singh and P. Kumar, “System Performance Comparison of Direct Torque Control Strategies Based on Flux Linkage and DC-Link Voltage for EV Drivetrains,” *SAE International Journal of Alternative Powertrains,* vol. 8, no. 2, pp. 103-118, Nov. 2019.

[98] B. Singh, P. Jain, A. Mittal and J. Gupta, “Neural Network Based DTC IM Drive for Electric Vehicle Propulsion System,” in *2006 IEEE Conference on Electric and Hybrid Vehicles*, Pune, India, 2006, pp. 1-6.

[99] A. Ghezouani, B. Gasbaoui and J. Ghouili, “Modeling and Sliding Mode DTC of an EV with Four In-Wheel Induction Motors Drive,” in *2018 International Conference on Electrical Sciences and Technologies in Maghreb (CISTEM)*, Algiers, Algeria, 2018, pp. 1-9.

[100] C. Lin, S. Liang, J. Chen and X. Gao, “A Multi-Objective Optimal Torque Distribution Strategy for Four In-Wheel-Motor Drive Electric Vehicles,” *IEEE Access*, vol. 7, no. 1, pp. pp. 64627-64640, May 2019.

[101] N. Mohan, Advanced Electric Drives, New Jersey, United States of America: John Wiley & Sons, Inc., 2014.

[102] S. Nawazish Ali, M. Hossain, D. Wang, K. Lu, P. Rasmussen, V. Sharma and M. Kashif, “Robust Sensorless Control Against Thermally Degraded Speed Performance in an IM Drive Based Electric Vehicle,” *IEEE Transactions on Energy Conversion*, vol. 35, no. 2, pp. 896-907, Jun. 2020.

[103] J. Gonzalez-Cordoba, R. Osornio-Rios, D. Granados-Lieberman, R. Romero-Troncoso and M. Valtierra-Rodriguez, “Thermal-Impact-Based Protection of Induction Motors Under Voltage Unbalance Conditions,” *IEEE Transactions on Energy Conversion*, vol. 33, no. 4, pp. 1748-1756, Dec. 2018.

[104] S. Nawazish Ali, A. Hanif, M. Hossain and V. Sharma, “An LPV H∞ Control Design for the Varying Rotor Resistance Effects on the Dynamic Performance of Induction Motors,” in *2018 IEEE 27th International Symposium on Industrial Electronics (ISIE)*, Cairns, QLD, Australia, 2018, pp. 114-119.

[105] J. Estima and A. Cardoso, “Efficiency Analysis of Drive Train Topologies Applied to Electric/Hybrid Vehicles,” *IEEE Transactions on Vehicular Technology*, vol. 61, no. 3, pp. 1021-1031, Mar. 2012.

[106] W. Qinglong, Y. Changzhou and Y. Shuying, “Indirect Field Oriented Control Technology for Asynchronous Motor of Electric Vehicle,” in *2020 IEEE International Conference on Power, Intelligent Computing and Systems (ICPICS)*, Shenyang, China, 2020, pp. 673-677.

[107] T. Öztürk and M. Aktaş, “Research on Control Strategy and Energy Consumption for Electric Vehicles,” *IFAC Proceedings Volumes*, vol. 46, no. 7, pp. 444-449, May 2013.

[108] E. Dehghan-Azad, S. Gadoue, D. Atkinson, H. Slater and P. Barrass, “Sensorless torque-controlled Induction Motor drive for EV applications,” in *2017 IEEE Transportation*

Electrification Conference and Expo (ITEC), Chicago, United States of America, 2017, pp. 263-268.

[109] J. Druant, F. De Belie, P. Sergeant and J. Melkebeek, "Field-Oriented Control for an Induction-Machine-Based Electrical Variable Transmission," *IEEE Transactions on Vehicular Technology*, vol. 65, no. 6, pp. 4230-4240, Jun. 2016.

[110] W. Qing-long, L. Chun, Y. Chang-zhou and Y. Shu-ying, "Field Weakening Control Technology for Asynchronous Motor of Electric Vehicle," in *2020 International Conference on Artificial Intelligence and Electromechanical Automation (AIEA)*, Tianjin, China, 2020, pp. 325-331.

[111] R. Bojoi, F. Farina, G. Griva, F. Profumo and A. Tenconi, "Direct torque control for dual three-phase induction motor drives," *IEEE Transactions on Industry Applications*, vol. 41, no. 6, pp. 1627-1636, Nov.-Dec. 2005.

[112] X. Xu, R. de Doncker and W. Novotny, "Stator flux orientation control of induction machines in the field weakening region," in *IEEE Industry Applications Society Annual Meeting*, Pittsburgh, PA, USA, 1988, pp. 437-443.

[113] M.-H. Shin, D.-S. Hyun and S.-B. Cho, "Maximum Torque Control of Stator-Flux-Oriented Induction Machine Drive in the Field-Weakening Region," *IEEE Transactions on Industry Applications*, vol. 38, no. 1, pp. 117-122, Jan./Feb. 2002.

[114] Z. Dong, Y. Yu, W. Li, B. Wang and D. Xu, "Flux-Weakening Control for Induction Motor in Voltage Extension Region: Torque Analysis and Dynamic Performance Improvement," *IEEE Transactions on Industrial Electronics*, vol. 66, no. 5, pp. 3740-3751, May 2018.

[115] J. Holtz, "Sensorless Control of Induction Motor Drives," *Proceedings of the IEEE*, vol. 90, no. 8, pp. 1359-1394, Aug. 2002.

[116] P. Vas, Sensorless Vector and Direct Torque Control, Oxford, United Kingdom: Oxford University Press, 1998.

[117] M. Elloumi, L. Ben-Brahim and M. Al-Hamadi, "Survey of speed sensorless controls for IM drives," in *Proceedings of the 24th Annual Conference of the IEEE Industrial Electronics Society*, Aachen, Germany, 1998, pp. 1018-1023.

[118] D. Xu, B. Wang, G. Zhang, G. Wang and Y. Yu, "A Review of Sensorless Control Methods for AC Motor Drives," *CES Transactions on Electrical Machines and Systems*, vol. 2, no. 1, pp. 104-115, Mar. 2018.

[119] x. Xin and C. Zhang, “Optimal Design of Electric Vehicle Power System with the Principle of Minimum Curb Mass,” in *The 8th International Conference on Applied Energy – ICAE2016*, Beijing, China, 2016, pp. 2629-2634.

[120] X. Zeng, Y. Peng and D. Song, “Powertrain Parameter Matching of A Plug-In Hybrid Electric Vehicle,” in *2014 IEEE Conference and Expo Transportation Electrification Asia-Pacific (ITEC Asia-Pacific)*, Beijing, China, 2014, pp.1-5.

[121] B. Sarlioglu, C. T. Morris, D. Han and S. Li, “Driving Toward Accessibility: A Review of Technological Improvements for Electric Machines, Power Electronics, and Batteries for Electric and Hybrid Vehicles,” *IEEE Industry Applications Magazine*, vol. 23, no. 1, pp. 14-25, Jan.-Feb. 2017.

[122] S. Anderson and L. Retief, “Research on Improved Driver Behaviour on South African Roads Phase A: Speed & Speed Limits in SA,” Road Traffic Management Corporation, Pretoria, South Africa, Mar. 2020.

[123] S. Rind, Y. Ren, Y. Hu, J. Wang and L. Liang, “Configurations and control of traction motors for electric vehicles: A review,” *Chinese Journal of Electrical Engineering*, vol. 3, no. 3, pp. 1-17, Dec. 2017.

[124] R. Pindoriya, B. Rajpurohit, R. Kumar and K. Srivastava, “Comparative analysis of permanent magnet motors and switched reluctance motors capabilities for electric and hybrid electric vehicles,” in *2018 IEEMA Engineer Infinite Conference (eTechNxT)*, New Delhi, India, 2018, pp. 1-5.

[125] M. Zeraoulia, M. Benbouzid and D. Diallo, “Electric Motor Drive Selection Issues for HEV Propulsion Systems: A Comparative Study,” *IEEE Transactions on Vehicular Technology*, vol. 55, no. 6, pp. 1756-1764, Nov. 2006.

[126] H. Kang and Z. Dandan, “Study on Driving Motor of Pure Electric Vehicles Based on Urban Road Conditions,” in *2013 International Conference on Communication Systems and Network Technologies*, Gwalior, India, 2013, pp. 839-842.

[127] I. Eroglu, L. Horlbeck, M. Lienkamp and C. Hackl, “Increasing the overall efficiency of induction motors for BEV by using the overload potential through downsizing,” in *2017 IEEE International Electric Machines and Drives Conference (IEMDC)*, Miami, USA, 2017, pp. 1-7.

[128] G. Pellegrino, A. Vagati, B. Boazzo and P. Guglielmi, “Comparison of Induction and PM Synchronous Motor Drives for EV Application Including Design Examples,” *IEEE Transactions on Industry Applications*, vol. 48, no. 6, pp. 2322-2332, Nov.-Dec. 2012.

[129] S. Park, J. Lee, Y. Lee and A. Ahmed, “Development of Electric Vehicle Powertrain: Experimental Implementation and Performance Assessment,” in *2016 Eighteenth*

International Middle East Power Systems Conference (MEPCON), Cairo, Egypt, 2016, pp. 932-937.

[130] V. Ambrožič, G. Buja and R. Menis, "Band-Constrained Technique for Direct Torque Control of Induction Motor," *IEEE Transactions on Industrial Electronics*, vol. 51, no. 4, pp. 776-784, Aug. 2004.

[131] R. Krishnan, Electric Motor Drives: Modeling, Analysis, and Control, New Jersey, United States of America: Prentice Hall, 2001.

[132] ABB, "Low Voltage Process Performance Motors," ABB, Zürich, Switzerland, Sep. 2020.

Appendix A – Motor Specifications

Table A-1: Induction motor specifications [132]

Parameter	Value
Output Power	37 kW
Input Voltage	400 V 50 Hz
Number of Poles	2
Synchronous Speed	3000 rpm
Rated Speed	2952 rpm
Full Load Efficiency	92.5%
Nominal Current	63.5 A
Rated Torque	119 N.m

Table A-2: Induction motor equivalent circuit parameters

Parameter	Value
Stator Resistance (R_s)	0.08233 Ω
Stator Leakage Inductance (L_{ls})	0.000724 H
Rotor Resistance (R_r)	0.0503 Ω
Rotor Leakage Inductance (L_{lr})	0.000724 H
Mutual Inductance (L_m)	0.02711 H
Stator Self-Inductance (L_s)	0.027834 H
Rotor Self-Inductance (L_r)	0.027834 H
Inertia	0.37 kg.m^2
Friction Factor	0.02791 N.m.s